Integration of Cervical Nervous Tissues into a Head-Neck Finite Element Model for the Investigation of Radiculopathy

By

Rachel Elaine Bruns

July, 2024

Director of Thesis: Alex Vadati, PhD

Major Department: East Carolina University Department of Engineering

Abstract

Radiculopathy of the spine is a prevalent chronic disorder caused by a wide number of pathologies, affecting up to 10% of individuals over the age of 50, caused by compression of the nerve roots. Recent concern has been raised at the increasing incidence of reported neck pain in fighter pilots, helicopter pilots, and crewmen. Repetitive loading activities such as wearing heavy helmets could be contributing to chronic neck pain, decreasing quality of life and safety while operating aircraft. To understand how to prevent and treat neck pain within the pilot population, a more in-depth understanding of the soft tissue interactions under chronic loading of the cervical spine must be investigated. Due to the ethical concerns of researching loading the neck in human experiments, mechanisms of nerve root pain and potential radiculopathy can be investigated using finite element (FE) modeling. The Nerve CSM (Cervical Spine Model) was developed in this thesis by adding nervous tissue to an existing head-neck model, the VIVA Open Human Body Model (OpenHBM). The newly developed nervous tissue encompassed gray and white matter of the spinal cord, cerebrospinal fluid, dura mater, root sheaths, spinal nerves, nerve roots, dorsal root ganglions, nerve rootlets, denticulate ligaments, foraminal ligaments and epidural ligaments.

Validation of the Nerve CSM's global head and spinal cord kinematics was performed by replicating a 2.3 m/s whiplash simulation and a flexion/extension simulation. The global head kinematics of the Nerve CSM in the 2.3 m/s whiplash simulation did not change substantially compared to the VIVA

OpenHBM. Additionally, the correlation score for the time response of the Nerve CSM compared to the experimental data was similar to the VIVA OpenHBM, thus, it is reasonable to conclude that the addition of the nerve geometry did not considerably alter the global kinematics of the VIVA OpenHBM. The results of the spinal cord kinematic validation of the Nerve CSM demonstrated that the spinal cord during flexion and extension of the head moved within the bounds of variation presented in the experimental data, pointing to a conclusion that the Nerve CSM demonstrates suitable spinal cord kinematics for a healthy participant. Future work will encompass the integration of the Nerve CSM into subject-specific pilot neck models to investigate the effect of cervical spine compression and flight related loading conditions on the interaction between the nerve roots and surrounding tissues.

Integration of Cervical Nervous Tissues into a Head-Neck Finite Element Model for the Investigation of Radiculopathy

A Thesis

Presented to the Faculty of the Department of Engineering

East Carolina University

In Partial Fulfillment of the Requirements for the Degree

Master of Science in Biomedical Engineering

By

Rachel Elaine Bruns

July, 2024

Director of Thesis: Alex Vadati, PhD
Thesis Committee Members:
Zachary Domire, PhD
Stephanie George, PhD

Acknowledgements

I would like to express my sincere gratitude and thanks to my supervisor, Dr. Alex Vadati, for his guidance and mentorship throughout the duration of my Master's.

Thank you to Dr. Stephanie George and Dr. Zachary Domire for their support and guidance as my committee members, and their investment in me and this project.

I would like to thank Mackenzie Hoey for her phenomenal support and friendship throughout our time in the lab at ECU, I would not have made it this far without her.

Special thanks to the Department of Defense, Office of Naval Research for sponsoring this research.

Lastly, I would like to thank all my family and friends for their love and support throughout my life and encouragement during my program at ECU.

Table of Contents

List of Tables

List of Figures

List of Abbreviations

A/P = Anterior/posterior

CNS = Central nervous system

CSF = Cerebrospinal fluid

DL = Denticulate ligament

DRG = Dorsal root ganglion

ELF = Extraforaminal ligament

FEM = Finite element model

IFL = Intraforaminal ligament

IVD = Intervertebral disk

IVF = Intervertebral foramen

JHMCS = Joint helmet mounted cuing system

LF = Ligamentum flavum

L/R = left/right

Nerve CSM = Nerve Cervical Spine Model

NVG = Night vision goggles

PLL = Posterior longitudinal ligament

PNS = Peripheral nervous system

PMHS = Post mortem human subject

SD = Standard deviation

S/I = Superior/inferior

SPH = Smoothed particle hydrodynamics

TFL = Transforaminal ligament

VIVA OpenHBM = VIVA Open Human Body Model

Nomenclature

E = Young's Modulus

ν = Poisson's Ratio

η = Viscosity

co = Sound velocity

s = Constant defining relationship between shock velocity and the particle velocity

Γ0= Mie-Gruneisen ratio (a material constant)

μ = Material constant in the Ogden hyperelastic formulation (Melly et al., 2021).

α = Material constant in the Ogden hyperelastic formulation (Melly et al., 2021).

CHAPTER 1: INTRODUCTION

Cervical spine radiculopathy (CSR) is a highly prevalent chronic pain disorder caused by a wide variety of pathologies, affecting up to 10% of individuals over the age of 50 (Mansfield et al., 2020). CSR is defined as compression of the cervical nerve root within the spine that causes a sensorimotor deficit and/or painful symptoms (Caridi et al., 2011). Root compression can be caused by a wide variety of pathologies, including disk herniation and bulging, spondylosis, instability, trauma, ligament ossification, and narrowing of the foraminal space (Caridi et al., 2011). Each of these pathologies can cause mechanical deformation, inflammation, or ischemic damage to the dorsal root ganglion or nerve root that results in ectopic firing and pain (Carette & Fehlings, 2005).

While cervical radiculopathy is prevalent within the common aging population, recent concern has been raised at the increasing incidence of reported neck pain in fighter pilots, helicopter pilots, and crewmen (Ang & Harms-Ringdahl, 2006; Harrison et al., 2015; Posch et al., 2019; Walters PL et al., 2012). In the past two decades, recent advances in technology have introduced headgear for pilots, such as night vision goggles (NVG) and the joint helmet mounted cuing system (JHMCS) to increase the ability to see while flying in low light and provide flight information to the pilot, which adds additional mass and alters the natural center of gravity of the head (Harrison et al., 2015; Lange et al., 2011). A survey of 58 F-16 pilots that use these systems regularly from the Danish Air Force found that 97% of the fighter pilots experience neck pain in flight or shortly after flying (Lange et al., 2011). It has often been assumed that the exposure to high G-forces is the leading cause of neck pain in fighter pilots; however, it has recently been demonstrated that helicopter pilots and crewmen that do not undergo the same high G-forces also have a high incidence of neck pain (Posch et al., 2019; Walters PL et al., 2012), meaning that wearing helmets with these systems for prolonged periods of time could be a major contributor to neck pain. A survey of 104 Austrian rescue helicopter pilots and 117 crewmembers found that 67.3% of pilots and 45.3% of crewmembers reported neck pain in the past 12 months (Posch et al., 2019). A survey conducted in 2012 reported that 58% of helicopter pilots and crew serving in the US army report flight-related neck pain (Walters PL et al., 2012). Human centrifuge experiments have shown that increasing loading of the cervical spine contributes to more strain in cervical stabilizing muscles which increases flight related risk of pain (Pousette et al., 2016). Poor posture, extended exposure to +Gz forces and vibrations, and the use of NVG and JHMCS systems for long periods of time are all hypothesized causes for flight-related neck pain (Van den Oord et al., 2012). Neck pain has been shown to significantly influence concentration, motor control, postural stability, and operation safety in fighter and helicopter pilots and crew (Ang & Harms-Ringdahl, 2006; Äng, 2008; Jørgensen et al., 2011; Sjölander et al., 2008; Stijn & van den Oord, 2015). Additionally, pilots reporting neck pain often need to take sick leave (Ang & Harms-Ringdahl, 2006), increasing the demand for new pilots, which is costly, as the training of a new pilot can range from $5.6-10.9 million (Mattock et al., 2019). Due to these adverse outcomes, strength training programs have been developed to improve neck strength and reduce workload on the cervical musculature and reduce neck pain (Ä et al., 2009; Salmon et al., 2011, 2013), which have been shown to yield preservative effects (De Loose et al., 2008; O'Conor et al., 2020; Thoolen & van den Oord, 2015; Wallace et al., 2021).

However, reported rates of neck pain have remained high in recent years (Chumbley et al., 2017; Omholt et al., 2017; Posch et al., 2019), suggesting that these interventions thus far have not been effective enough to reduce pain significantly in the pilot population. Additionally, studies reporting the frequency of neck pain in helicopter pilots do not always report types or descriptions of symptoms of pain. Neck pain is an extremely broad term to describe the diverse variety of potential mechanisms and locations of chronic pain generation. Most instances of literature including more descriptive information report muscle strain and stiffness and facet joint syndromes (Jones et al., 2000), but more serious injuries such as disk herniation and bulging and degeneration of the spine have also been reported (Hämäläinen et al., 1994; Newman, 1996; Schall, 1989) which are potential causes of nerve root compression seen in cervical radiculopathy. These findings suggest that there may be other pain mechanisms, such as nerve root compression, at play besides muscular strain. Thus, an in-depth investigation into the pain mechanisms within the cervical spine under helmet loading conditions must be performed to understand how to decrease neck pain in the pilot population.

Finite element analysis is a computational modeling method that utilizes constitutive mathematical equations to simulate mechanical behavior of one or multiple components under loading conditions. In the past two decades, significant progress has been made in the ability to model components and tissues of the human body to overcome ethical and physical obstacles associated with human subjects and cadaver experiments. There is a considerable amount of research in development of cervical spine models investigating loading of the vertebrae, facet joints, ligaments, and intervertebral disks (Cai et al., 2020; H. J. Kim et al., 2009; Rahman et al., 2022; Subramani et al., 2020); however, there are a limited number of studies utilizing finite element models (FEM's) with nerves and nerve roots due to the complexities of their anatomical makeup. Existing models including nerves and nerve roots (Ah Shin et al., 2016; Khuyagbaatar et al., 2017, 2018; H. J. Kim et al., 2009; Mihara, 2018; Xue et al., 2021, 2023) are simplified and do not investigate mechanisms of nerve root compression and interaction with other soft tissues under chronic compression of the cervical spine.

Thus, this research proposal's objective is to build an advanced model of the soft tissues within the spinal canal and vertebral spaces that are relevant to pain generation during chronic compression of the spine. This project is part of a larger work that is seeking to build subject-specific head-neck models of fighter pilots and investigate the mechanism of pain under helmet induced loading conditions. To do this, it is critical to have a working model of the soft tissues and nerves within the spine. Thus, this thesis was focused on integrating the soft nervous tissues into the VIVA OpenHBM model, a well-validated model of the head-neck complex developed by (Östh et al., 2017). The appropriate nervous tissue geometries were created and established into the existing 50th percentile female VIVA OpenHBM model through the definition of accurate material properties and boundary conditions. Additionally, validation of the new model's global kinematic response in the 2.3 m/s whiplash simulation (Östh et al., 2017) and spinal cord kinematics in flexion/extension according to the experiment performed by (Stoner et al., 2019) was performed. This thesis is organized into five chapters, where Chapter 2 will outline the background information necessary to understand the appropriate anatomy, biomechanical properties, and pain mechanisms relevant to cervical radiculopathy, and a review of existing FEM's that include nerves and nerve roots. Chapter 3 will provide a description of the methods used in this study, Chapter 4 will discuss the results, and Chapter 5 will provide a discussion of the current study compared to the literature, limitations, and future research direction.

CHAPTER 2: BACKGROUND

2.1 Anatomy

2.1.1 Anatomic Planes and Directions

In this thesis, the anatomic position of the body refers to a neutral, standing position with the head, feet, and palms of the hand facing forwards (Figure 1)(Standring, 2020). This position is the baseline upon which all other anatomical directional conventions are based on. There are several critical directional conventions and anatomical planes utilized in human anatomy that are used to describe positions of body parts globally or locally relative to one another.

The superior direction points upwards, towards the head, while the inferior direction points downwards, towards the feet (Standring, 2020). In human anatomy specifically, the cranial (closer to the head) and caudal (away from the head) direction can be used interchangeably with the superior and inferior direction. The anterior direction is towards the front of the body, while the posterior direction is to the back (Standring, 2020). Two other terms, ventral and dorsal, will also be used interchangeably throughout this thesis, with ventral corresponding to the anterior direction and dorsal corresponding to the posterior direction. Lastly, the medial direction points towards the centerline of the body, while the lateral direction points away from the centerline of the body (Standring, 2020). Proximal refers to a point on the body that is closer to the trunk or the site of attachment, while distal means it is farther away from trunk or point of attachment (Standring, 2020). There are additional definitions that are commonly used for more complex descriptions; however, these are the basis of all other terms and are the ones that will be used frequently throughout this thesis.

Further, the body can be split up into three imaginary, intersecting planes. The frontal plane splits the body into front and back sections, also known as the coronal plane. The sagittal plane lies in the center and is oriented anterior-posteriorly, separating the torso into right and left symmetrical halves, also referred to as the median plane. The transverse plane lies along the axis of the body and separates it into top and bottom divisions and is also known as the axial plane (Standring, 2020).

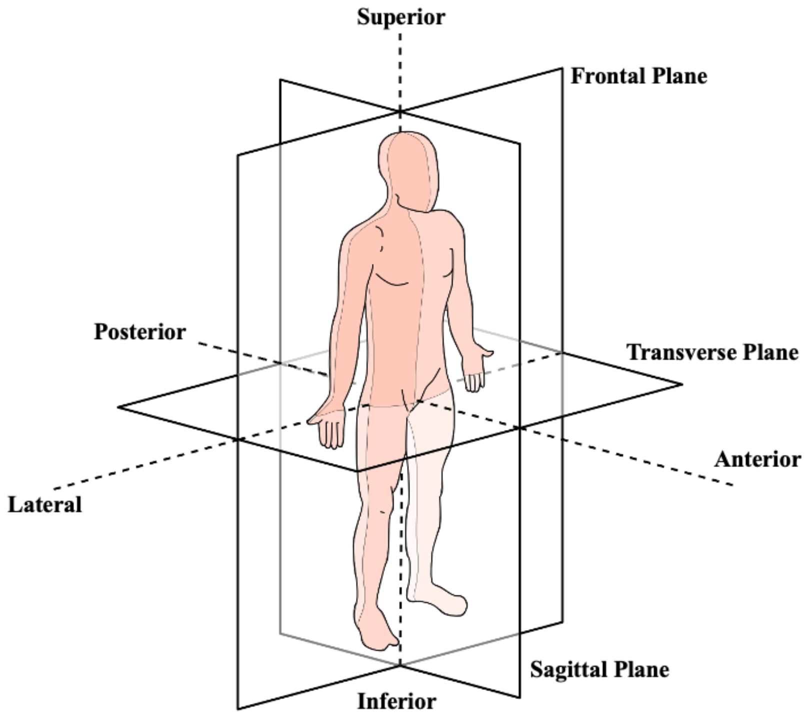

Figure 1: Anatomical Planes and Directions.
Source: [Adapted from (CFCF, 2014)].

2.1.2 Spine Terminology

The spine is categorized into five main sections, defined by the individual bones, called vertebrae, that form a continuous column from the skull down to the pelvis (Figure 2)(Betts et al., 2013). The cervical spine (C) consists of the first seven vertebrae and then transitions to the thoracic spine (T), which is composed of twelve vertebrae. The lumbar spine (L) is directly inferior to the thoracic spine and contains five vertebrae. Below the lumbar spine is the sacrum and coccyx, which connect to the hip bones and form the structure of the pelvis. When referring to a specific vertebra, the convention is to use the initial of the spinal section first, followed by the number in that sequence (DiPaola & Eck, 2014). For example, the third cervical vertebra would be referred to as C3. Location along the length of the spinal column is denoted as the spinal level or segment, which is a functional unit that consists of the superior and inferior vertebrae in that position and encompasses the surrounding connective tissues. For example, a soft tissue between the 4^{th} and 5^{th} cervical vertebrae would be at the C4/5 spinal level.

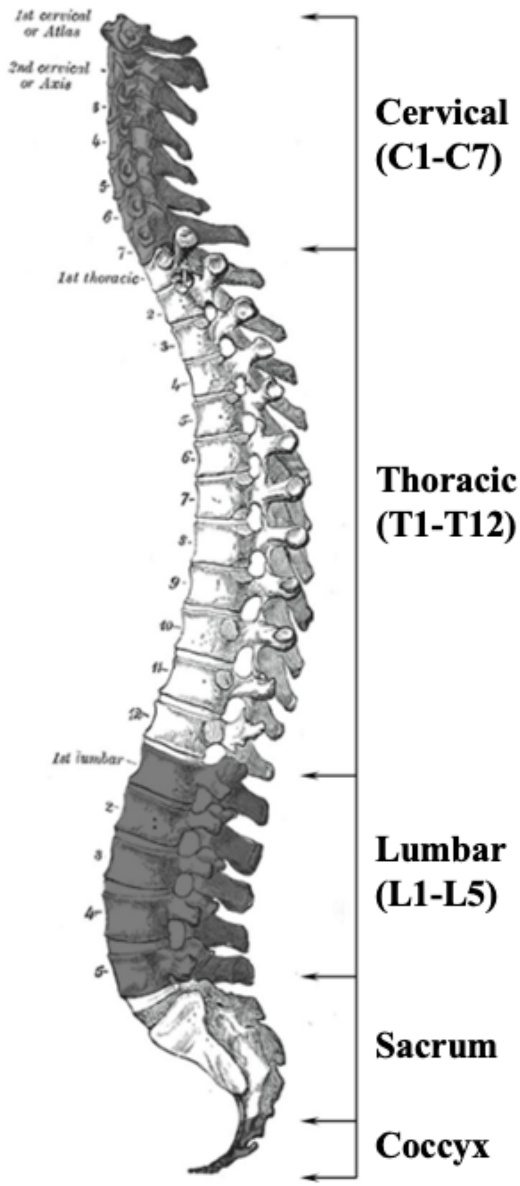

Figure 2: Classification of the Human Vertebral Column.
Source: [Adapted from (Gray & Lewis, 1918)].

The cervical spine is capable of four primary movements, which when combined, provide remarkable range of motion (ROM) of the head-neck complex. Flexion is bending of the neck towards the front of the body and is utilized when looking down or touching one's chin to their chest. Extension is the bending of the neck towards the back of the body, also known as looking upward. Lateral bending is the action of tilting the neck to either side of the body or touching one's ear to their shoulder. Lastly, axial rotation is turning the head and neck side to side. The cervical spine is a unique structure with exceptional mobility and facilitates both stability and flexibility of the head (Standring, 2020).

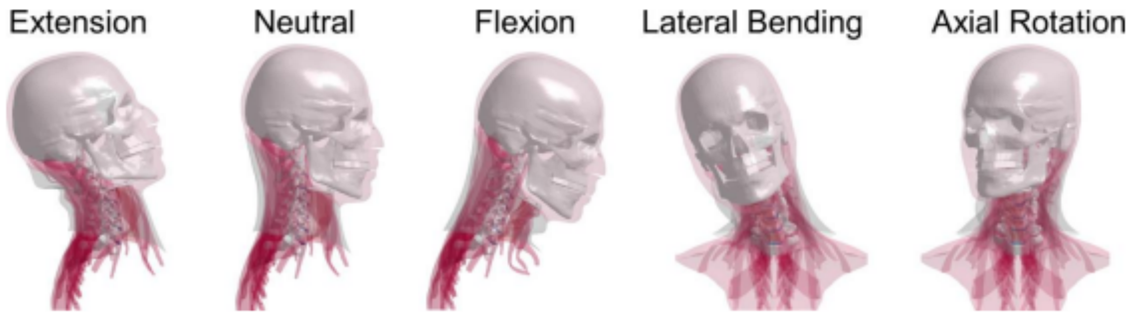

Figure 3: Primary Motions of the Cervical Spine.
Source: (Shen, 2020).

2.1.3 Anatomy of the Cervical Spine

2.1.3.A. Cervical Vertebrae and Intervertebral Discs

The cervical spine is a complex structure that aids in sensory and motor function as well as protection and movement. It is composed of seven bony vertebrae (C1-C7) whose primary job is to provide structure and flexibility to the spinal column while protecting the nervous tissue housed inside (DiPaola & Eck, 2014). The cervical vertebrae are unique, as the first two cervical vertebrae are different from the rest and have their own distinguished names, functions, and articulations. The third through seventh cervical vertebrae have the same anatomical characteristics as one another, but vary slightly in dimension and proportion, growing bigger and wider the farther down the spinal column they are located.

The first two cervical vertebrae are distinguished from the rest of the vertebrae in their anatomical makeup and distinct function (Figure 4)(Standring, 2020). The first cervical vertebra (C1) is named the atlas and directly interfaces with the skull through the occipital condyles located on both superior articular surfaces and allows movement. The atlas does not have a defined vertebral body or a connecting intervertebral disc; instead, it interfaces directly through the articular facets with the C2 vertebra, called the axis. The axis has a unique functionality in allowing the head-neck complex to rotate axially, facilitated through a structure called the dens, which is a rounded bony surface that protrudes superiorly and couples to the atlas on the dorsal side of the anterior arch in a groove called the dens articular facet. Holding the dens in place is the transverse ligament, which originates from the medial surfaces of the atlas and crosses the vertebral foramen to attach on the posterior surface of the dens. The underside of the axis has two inferior articular facets and a vertebral body, which interface seamlessly with the C3 vertebra below it.

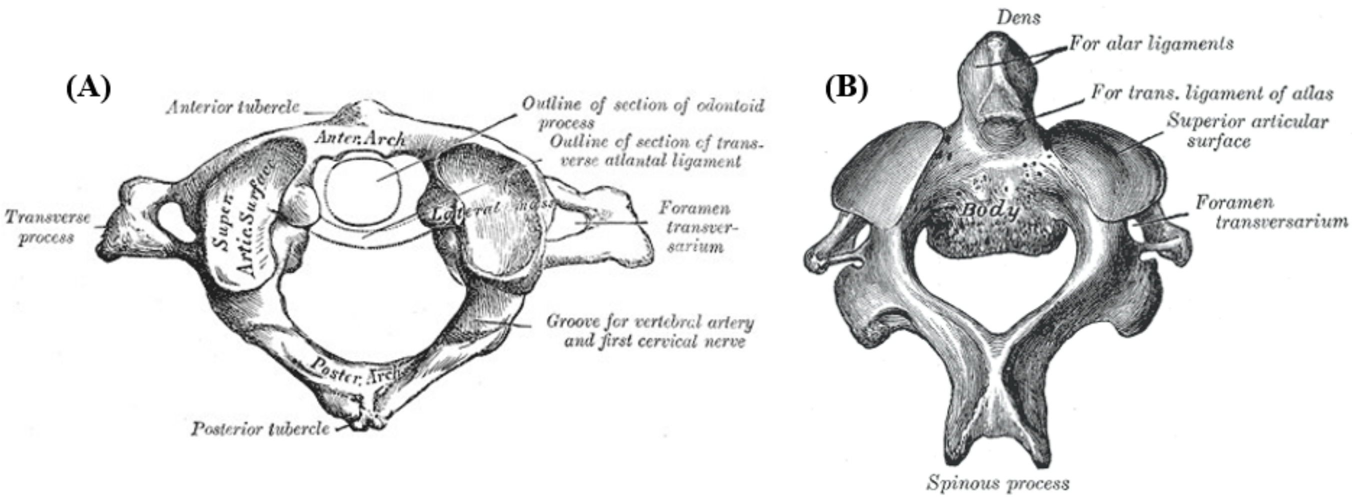

Figure 4: Anatomical Landmarks of the Atlas (A) and Axis (B).
Source: [Adapted from (Gray & Lewis, 1918)].

Concerning C3-C7, the anterior portion of the vertebrae is the vertebral body (Figure 5)(Betts et al., 2013). Posterior to the body of the vertebrae is the spinal canal, also called the vertebral foramen, which is a cavity that houses the spinal cord. The transverse processes lie laterally on both sides of the vertebrae and are an important attachment site for ligaments and other soft tissue structures. The cavity within the transverse process houses the vertebral artery, which travels down the length of the spine. Connection between the transverse processes and the vertebral body is made by the pedicle, which is a flat, bridging structure. Just posterior to the transverse processes are the superior and inferior articular facets, the site of the facet joints which constrain motion and transfer loads between vertebrae. The facet joint consists of the convex inferior articular process of the superior vertebra connecting to the concave superior articular process of the inferior vertebra. Posterior to the facet joints are the laminae, which eventually gives way to the spinous process, a bony structure that sharply juts out in the dorsal direction.

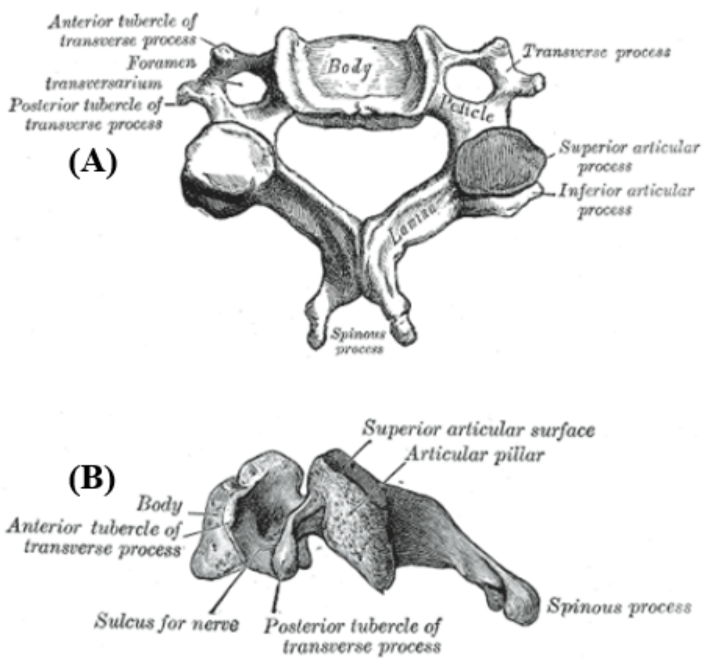

Figure 5: Anatomical Landmarks of the Cervical Vertebrae.
(A) is the superior view, (B) is the left lateral view. *Source: [Adapted from (Gray & Lewis, 1918)].*

One area that is of great significance to this thesis is the intervertebral foramen (Figure 6), which is a lateral opening on both sides formed by the junction of two connecting vertebrae. It is bounded superiorly and inferiorly by the pedicles of the adjacent vertebrae, anteriorly by the intervertebral disc and posteriorly by the facet joints. This opening provides a window for neural structures and blood vessels to travel out of the spinal canal and to the rest of the body. It is a highly complex area filled with a vast network of connecting tissues that provide stability, functional transport, and protection to the nervous tissue housed within.

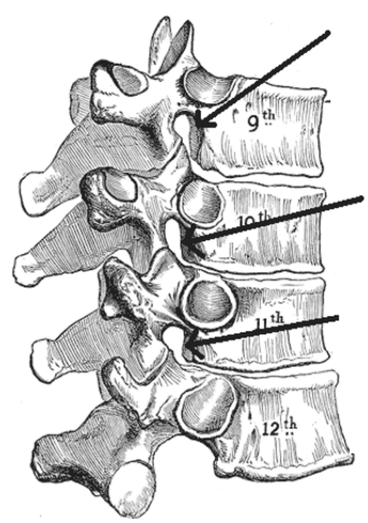

Figure 6: Left Lateral View of Thoracic Intervertebral Foramen (arrows).
Source: [Adapted from (Wikipedia, 2007)].

Each vertebral body is separated from one another by intervertebral disks (IVDs), except for the atlantoaxial joint between C1 and C2 (Standring, 2020). IVDs have many functions, such as connecting the vertebrae, counteracting compressive and tensile forces on the spine, and allowing enough space for nerve roots to exit the spine. Each disk is made up of two main components, an outer ring of tough fibers called the annulus fibrosus, and an inner volume of fluid-like material called the nucleus pulposus (Figure 7). The annulus fibrosis is composed of layers of lamellae that contain collagen fibers with various orientations surrounded by a ground substance made up of water and proteoglycans. These lamellae layers are arranged concentrically around each disk and the angles of the collagen fibers alternate between each layer to provide stability during the motion of the spine. The nucleus pulposus gelatinous material serves to resist and distribute compressive loads to the vertebrae, expanding during compression and causing the collagen fibers in the annulus fibrosis to bulge under tension. Together, this exceptional combination of these two components provides flexibility, stability, and shock absorption to the spine during movement of the neck (DiPaola & Eck, 2014).

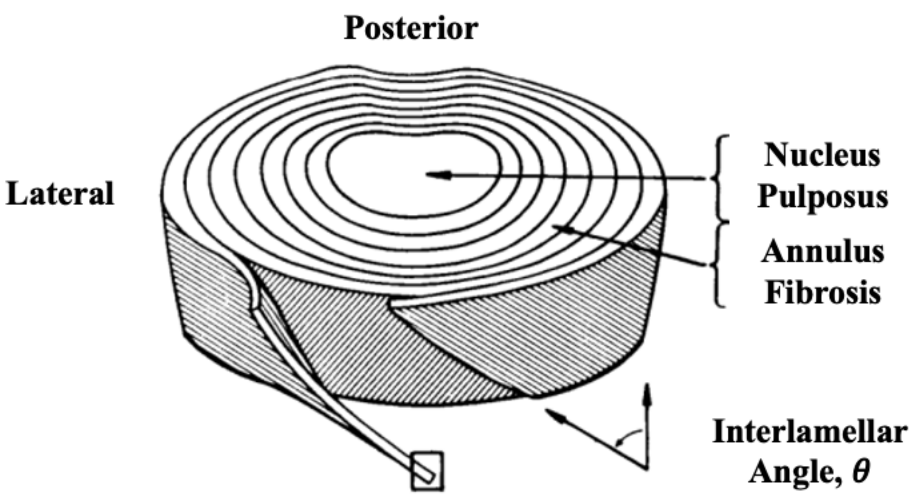

Figure 7: Components of the Intervertebral Disk.
The concentric rings of the annulus fibrosis have fibers oriented at an alternating interlamellar angle, θ, and surround the fluid-like nucleus pulposus in the center. *Source: [Adapted from (Cassidy et al., 1989; Shen, 2020)].*

2.1.3.B. Nervous Structures and Soft Tissue within the Spinal Column

There are two divisions within the nervous system, namely the central nervous system (CNS), which consists of the spinal cord and the brain, and the peripheral nervous system (PNS), which consists of nerves that extend from the spinal cord and brain (Betts et al., 2013). The spinal cord is housed within the column formed by the vertebral foramen, originating as part of the brainstem, and traveling down the length of the spine and ending at the conus medullaris, the tip of the inferior spinal cord, around the L1/L2 vertebrae. The spinal cord is made up of two types of tissue, called white matter and gray matter, with the white matter surrounding the inner gray matter, appearing like a butterfly in shape (Figure 8). The white matter is made up of axons that connect the brain to the rest of the body, while the gray matter houses the neuronal cell bodies.

The PNS starts as pairs of spinal nerves that originate on the spinal cord itself to then extend outward to the rest of the body, exiting the vertebral canal through the opening provided by the intervertebral foramen (Standring, 2020). The origination of each spinal nerve is facilitated through a unique nervous tissue, called the nerve root. Two pairs of nerve root structures, the ventral and dorsal roots, connect and extend from the spinal cord at each level of the spine with multiple rootlets at the insertion site (Figure 8). The ventral nerve roots, anteriorly located, are efferent nerves that send motor signals to distal tissues and their cell bodies are located within the anterior horns of the gray matter in the spinal cord (Olmarker, 1991; B. Rydevik et al., 2012). The dorsal nerve roots, posteriorly located, are afferent nerves that receive sensory input from the body and transmit the information to the CNS. Their cell bodies are in the dorsal root ganglion (DRG), which is a swelling of the root that forms a bulb-like structure, located distally from the spinal cord on the dorsal root (Olmarker, 1991; B. Rydevik et al., 2012). After the DRG, the ventral and dorsal root finally reach the intervertebral foramen (Hasue et al., 1983). Within the foraminal space, nerve roots typically take up approximately 30 to 50% of the cross-sectional area as they exit the vertebrae (Kitab et al., 2009). After exiting the intervertebral foramen, they come together to form the spinal nerve and then split again into the dorsal and ventral rami, which extend and innervate specific targets distal from the spinal cord.

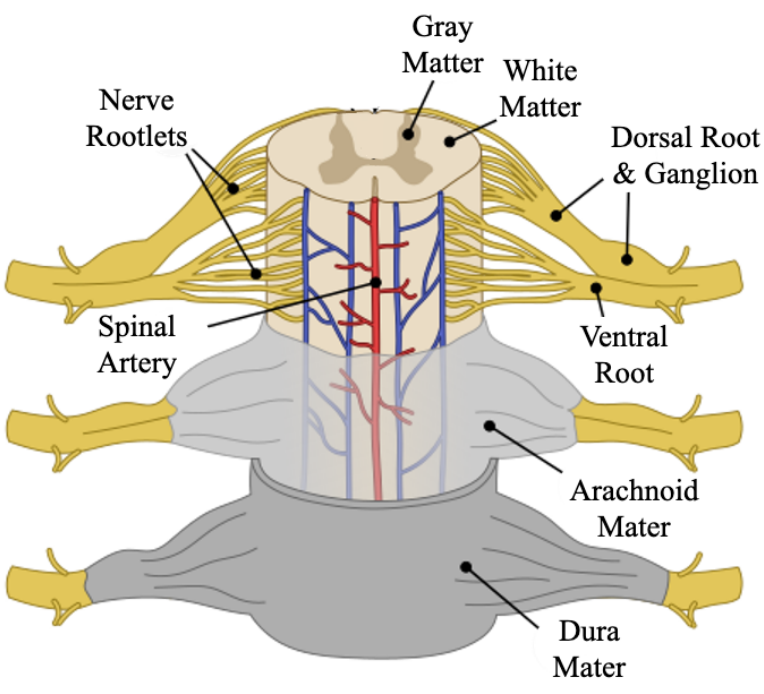

Figure 8: Innervation of the Nerve Roots on the Gray and White Matter of the Spinal Cord.
Source: [Adapted from (umimeto.org, 2020)].

The dorsal root ganglion (DRG) plays a crucial role in the function of nerves as it houses the cell bodies of sensory neurons (B. L. Rydevik, 1992). DRGs are located distally to nerve roots high within the foramen and directly below the pedicle, leaving it highly vulnerable to compression (De Peretti et al., 1989). This position makes DRG unique because they connect to both the CNS through a long axon that goes up the spinal column and the PNS via peripheral nerves (Brisby, 2003). The synthesis of many important proteins that provide structure to axons takes place in DRGs, causing an increased metabolic demand. With this increased metabolic demand comes a more permeable membrane and a richer microvascular network than other areas of spinal nerves (B. L. Rydevik, 1992).

Like the vertebrae, the spinal cord can be divided into cervical, thoracic, lumbar, and sacral segments. Within the cervical spine, there are eight pairs of cervical nerve roots and spinal nerves that innervate various tissues and organs in the upper body region (Standring, 2020). The cervical spinal cord can be further separated into eight distinct divisions, with each section comprised of the corresponding nerve rootlets, nerve roots and spinal nerves. The length of each spinal cord segment shortens as it travels down to the end of the cervical spine, with the nerve roots oriented in the spinal canal cranial-caudally, exiting through the intervertebral foramen formed by the corresponding vertebrae. For example, the C4 spinal nerve roots travel through the C3/C4 intervertebral foramen.

Within peripheral nerves are fibers, also called axons, that innervate distal body parts and conduct impulses to and from the CNS. In addition, these fibers physically connect nerve cell bodies and organs that allow critical substances secreted from the cell bodies to travel back and forth, a process called axonal transport (B. Rydevik et al., 2012). The axons are frequently covered with a sheath of layered, sectioned tissue called myelin, which is formed by Schwann cells that lay along the length of the axon, which is fundamental in increasing the conduction velocity of the impulses (B. Rydevik et al., 2012). The peripheral nerve consists of three layers, the endoneurium, perineurium, and epineurium, shown below in Figure 9. The endoneurium is connective tissue composed of fibroblasts and collagen which surrounds each individual axon to form a bundle of fibers, called fascicles (B. Rydevik et al., 2012). Surrounding each fascicle is the perineurium, consisting of a thin layer of tough, dense tissue to protect the nerve fibers from mechanical and chemical damage that additionally serves as a blood-nerve barrier preventing substances from outside environments penetrating the endoneurium (Paggi et al., 2021). The outermost layer, the epineurium, surrounds the entire group of fascicles and blood vessels interspersed throughout the fascicles, and provides a cushion during movement of the nerve, often showing thicker layers where nerves are precariously positioned near bone (B. Rydevik et al., 2012).

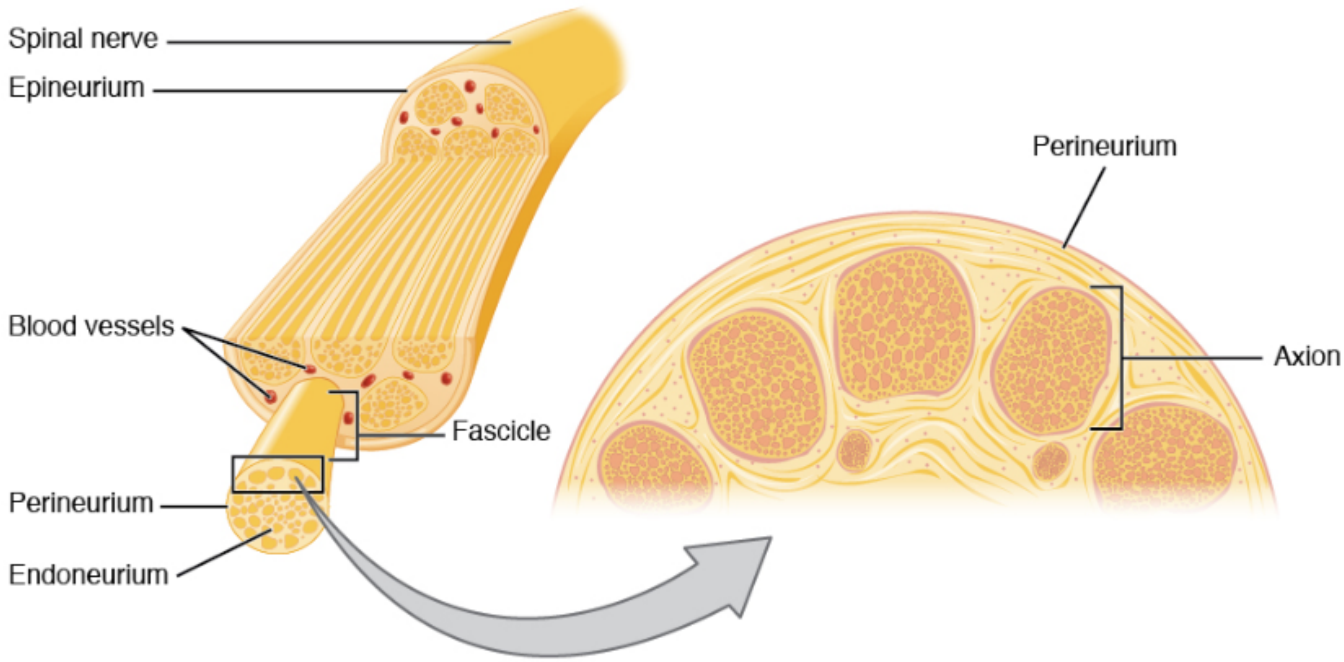

Figure 9: Peripheral Nervous Structure and Histological Breakdown.
Source: [Adapted from (Betts et al., 2013)].

Three layers of tissue called meninges, classified as the pia mater, the arachnoid, and the dura mater surround the spinal cord and nerve roots (Standring, 2020), shown below in Figure 10. The pia mater directly covers the spinal cord and separates it from the subarachnoid space. Within the subarachnoid space is clear plasma-like cerebrospinal fluid (CSF) that acts to protect the CNS from mechanical and immunological harm (source). Surrounding the subarachnoid space is the arachnoid and the dura mater, which enclose the CSF. As the nerve roots travel through the CSF and approach the wall of the dura mater, an envelope-like fold is formed by the dura for the nerve roots to travel through. This opening facilitated by the dura pinches in towards the nerve root as it becomes more distal from the spinal cord, and fuses to the outer surface of the nerve root itself (B. Rydevik et al., 2012). This forms a sheath around the ventral and dorsal root and DRG, referred to as the root sheath (B. Rydevik et al., 2012). The nerve root itself consists only of the endoneurium, lacking the perineurium and epineurium that provide structure and protection to the rest of the peripheral nerves (B. Rydevik et al., 2012). However, the dura mater encloses the nerve root and fuses with the root sheath to become the perineurium and epineurium once the spinal nerve is formed (B. Rydevik et al., 2012).

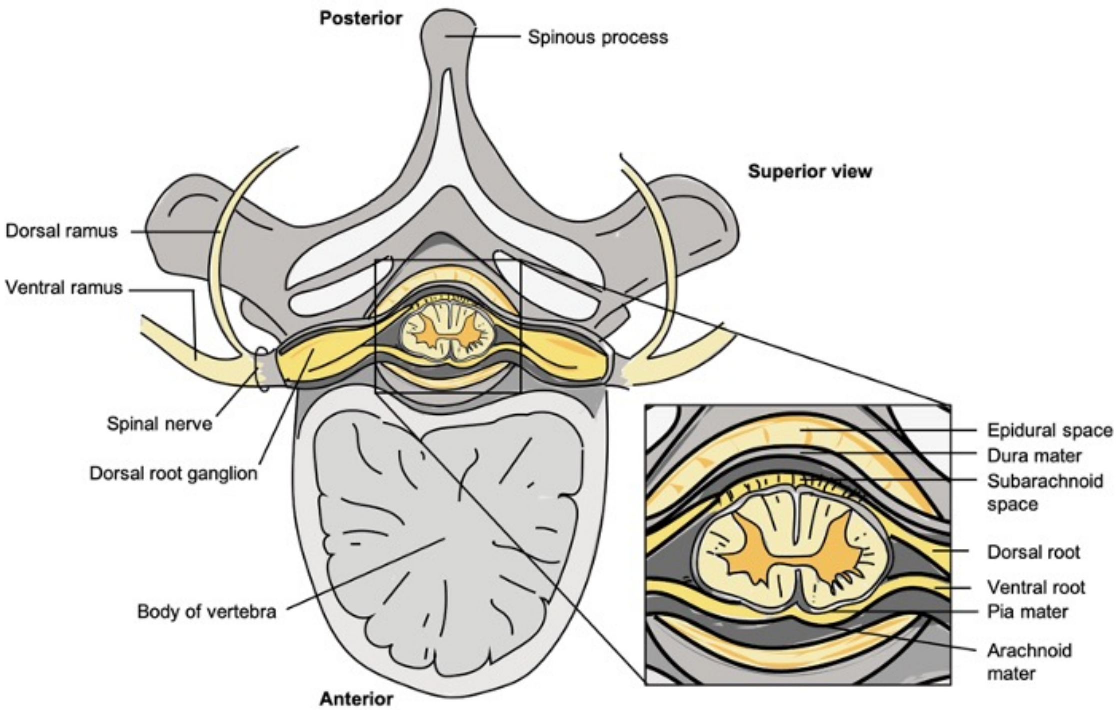

Figure 10: Cross-sectional Anatomy of the Spinal Cord, Meninges and Nerve Roots within the Spinal Column.

Source:(Mazzasette, 2021).

2.1.3.C. Ligaments Within the Spinal Column and IVF

There are many ligaments throughout the spinal column and extraforaminal space that work to stabilize and minimize stress on the nervous tissue (Lohman, 2014). The main vertebral ligaments within the spinal column that are relevant to later discussion is the posterior longitudinal ligament (PLL) and the ligamentum flavum (LF) (Figure 11). The PLL is located on the posterior side of the vertebral bodies, stabilizing their connection to each other by running throughout the entire length of the spinal canal. The LF connects the laminae of adjacent vertebrae on the posterior side of the spinal column.

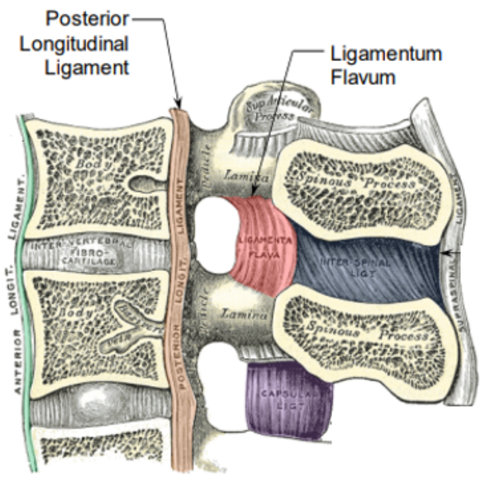

Figure 11: Anatomy of the Posterior Longitudinal Ligament and the Ligamentum Flavum.
Source: [Adapted from (Gray & Lewis, 1918)].

Within the subarachnoid space are the denticulate ligaments (DLs), which originate on the lateral surface of the white matter and insert on the interior surface of the dura mater, working to stabilize the spinal cord within the CSF. The DLs have been described as “a long ribbon-like ligament on each side of the spine that suspends the spinal cord in the dural sac through a series of bilateral saw-toothed ligamentous attachments” (Ceylan et al., 2012). Essentially, the DLs are akin to a thin triangle, with the base attached to the white matter and the apex attached to the wall of the dura mater with a thin, fibrous strip (Figure 12). Each DL is located in between the ventral and dorsal nerve rootlets and is superomedial to the intervertebral foramen of the vertebrae at the spinal level below it. Histologically, the DLs are composed of collagen fiber bundles, where the fibrous strip portions consisted of longitudinally oriented fibers and the triangular extension consisted of transversely and obliquely oriented collagen fibers (Ceylan et al., 2012).

Figure 12: Denticulate Ligament Attachments in the Cervical Spine.
*Shows the fibrous strip attachment at the distal end of the DLs. *Source: (Ceylan 2012).*

Anteriorly and posteriorly, the dural sac is held in place by additional connective tissues, referred to here as the epidural ligaments. Fibrous attachments connecting the PLL to the ventral wall of the dura in the anterior space have been defined as Hoffmann's ligaments, and travel ventrolaterally from the dura to the vertebral canal (Tardieu et al., 2016) (Figure 13). They have been described as narrow, threadlike connections and the quantity varies between vertebral levels and species with three distinct types: midline, lateral and proximal root sleeve (Wadhwani et al., 2004). At lumbar levels, they are often thick and well developed, but as they travel superiorly up the spine, they become thin and scanty (Tardieu et al., 2016). A study done by (Wadhwani et al., 2004) found Hoffmann's ligaments in all their specimens at levels C7-L5. However, they did not find them in levels superior to C7, thus, the existence of these ligaments in the cervical spine is questionable. Along the entire vertebral column, the PLL is loosely adhered to the midline of the dural wall, but at higher cervical levels, the ventral dural sac has been found to closely adhere to the PLL (Tardieu et al., 2016). These ligaments have been hypothesized to limit posterior movement of the spinal nerves, preventing stretching that could lead to pain. However, they could also be a contributing factor in chronic pain from prevention of movement (Yong-Hing et al., 1976).

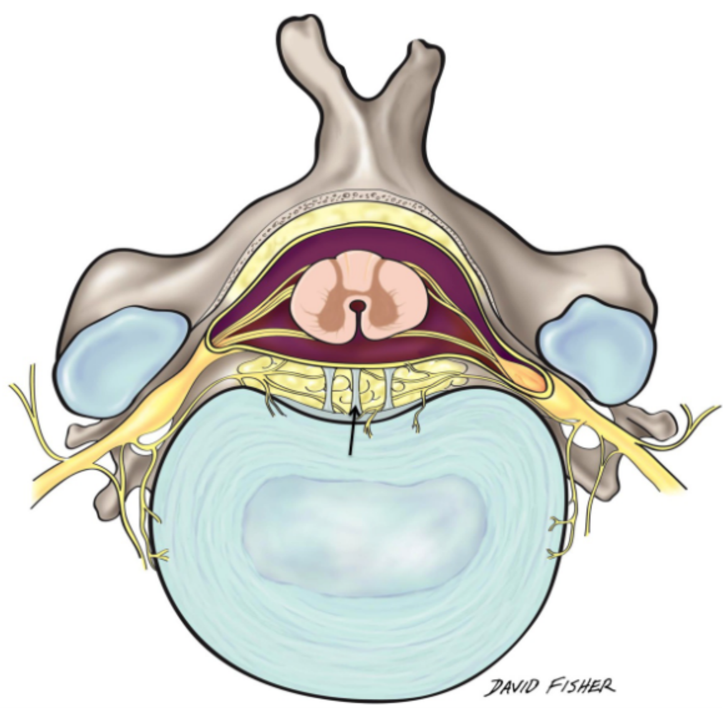

Figure 13: Hoffman's Ligaments (arrow) in the Epidural Space.
Source: (Tardieu et al., 2016).

Posteriorly, there are also connections in the epidural space that connect the posterior wall of the dura mater to the ligamentum flavum and the posterior vertebral walls. These ligaments are often referred to as the posterior epidural ligaments in the literature but are less well-defined than other structures discussed here. They have been described as dense, tight fibrous connections within the median areas of the posterior epidural space (Shi et al., 2014). One study reported their presence in all 22 specimens and found them in the C1-C5/6 levels (Shi et al., 2014). Their orientation was primarily craniocaudal from the dorsal surface of the dural sac to the laminae or ligamentum flavum, however, there were some that had the opposite orientation (Figure 14). Typically, there was only one ligament at each vertebral level, however, it was also not uncommon to see two, one on the right and the left. The space between the dura mater and the vertebral walls was filled with areolar connective tissue, pockets of loose fat, lymphatics and blood vessels (Shi et al., 2014).

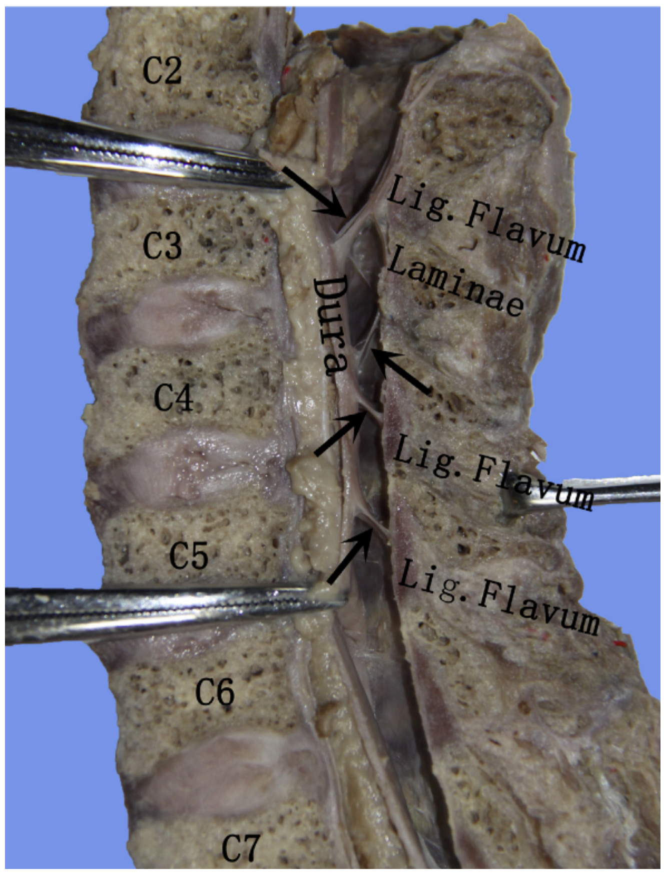

Figure 14: The Posterior Epidural Ligament Attachments (arrows) in the Epidural Space.
Source: (Shi et al., 2014).

The ligaments that directly interact with the nerve roots and DRG are the foraminal ligaments. These ligaments attach the nerve root, DRG and spinal nerve to the intervertebral foramen (Hasue et al., 1983) and their function is to dissipate traction forces by keeping the root centrally located (De Peretti et al., 1989). By limiting strains on the nerve roots and DRG, they prevent permanent deformation and promote adequate blow flow, as well as allowing action potentials to continue to fire normally (Lohman, 2014). Foraminal ligaments are split into two categories based on their location within the intervertebral foramen, which is bounded by the superior and inferior pedicles of the vertebrae. The pedicle is split into three different zones (Figure 15), the medial zone, middle zone, and lateral zone (Ebraheim et al., 1996). The medial zone is the part of the pedicle medial to the opening of the transverse foramen. The middle zone is the part of the pedicle that spans the length of the adjacent transverse foramen. Lastly, the lateral zone encompasses the part of the pedicle lateral to the transverse foramen. Ligaments that occur within the medial and middle zones are referred to as intraforaminal ligaments (IFLs), while ligaments that occur within the lateral zone are referred to as extraforaminal ligaments (EFLs) (Shi et al., 2015; Yang et al., 2019).

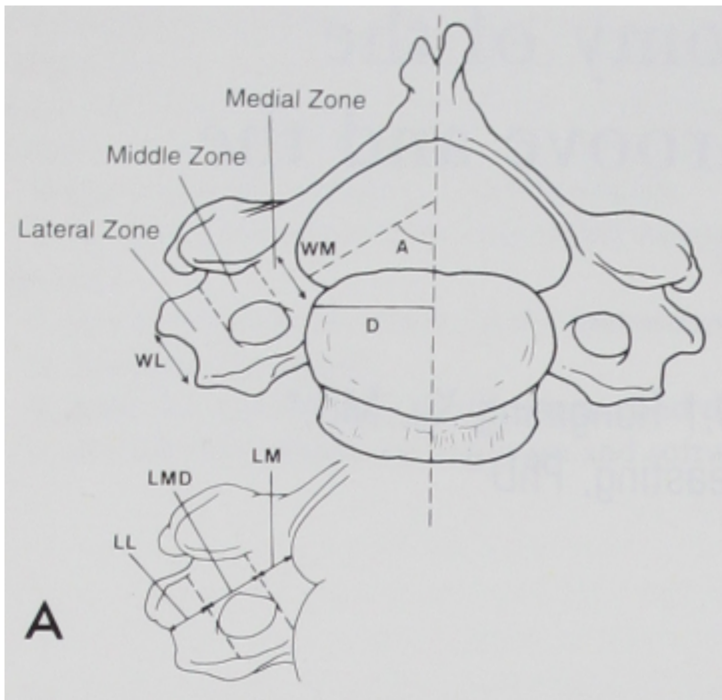

Figure 15: Pedicle Zone Classifications of the Cervical Vertebrae.
Source: (Ebraheim et al., 1996).

IFLs connect the nerve roots to the periosteum surrounding each foramen radially, and most often meet the nerve roots at a right angle, ranging in appearance from strands of connective tissues to a complete membrane (Yang et al., 2019). When looking at a cross section of the intervertebral foramen, it closely resembles a bicycle wheel, with the nerve root in the center and the IFLs as the spokes. Relatively fewer, looser, and thinner IFLs have been observed in upper levels of the cervical spine (C1/2-C3/4), whereas thicker and stiffer IFLs have been observed in the lower levels (C4/5-C6/7) (Yang et al., 2019). Within the medial zone, IFLs radially attach to the nerve root most commonly from the posterior facet joint capsule the posterior part of the intervertebral disc, and the upper and lower edges of the inferior and superior pedicle, respectively (Figure 16). Only one to two medial zone IFLs have been observed in the C1/2 IVF, whereas numbers at IVFs C4-T1 ranged from four to seven. These medial zone IFLs are typically covered in a membranous structure, that when removed reveals their cord-like appearance. They attach directly to the root sleeve that surrounds both the dorsal and ventral nerve root (Figure 16).

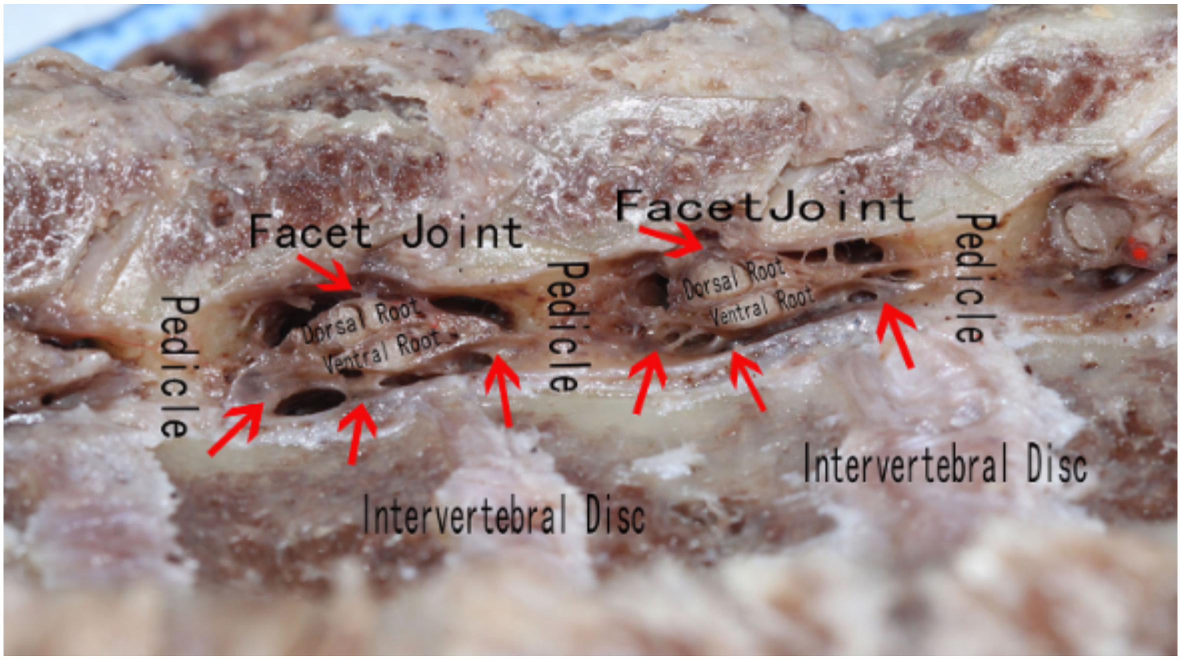

Figure 16: Common Attachment Sites of the Medial Zone IFLs (red arrows).
Source: (Yang et al., 2019).

As the nerve root travels laterally from the medial zone into the middle zone of the intervertebral foramen, the IFLs increase in both number and complexity, appearing as thin, cord-like strands that weave around each other and create a web-like structure, attaching loosely to the root sleeve and vascular walls in the fat space (Figure 17). Due to their interwoven nature, it is difficult to quantify the number of middle zone IFLs at each level, however, (Yang et al., 2019) reports that they are noticeably more developed at the C4-T1 levels. In addition, blood vessels and fat are interspersed throughout these ligaments (Figure 17).

Figure 17: Attachments of the Interwoven Medial Zone IFLS (red arrows).
Source: (Yang et al., 2019).

EFLs connect the newly formed spinal nerve to the intervertebral foramen and are located in the lateral zone of the pedicle. They can be separated into two different types, radiating ligaments and transforaminal ligaments (TFLs)(Shi et al., 2015). Radiating ligaments attach the spinal nerve to the walls of the surrounding IVF and to the transverse processes, and encompass superior, inferior, posterior and anterior attachments (Shi et al., 2015). A study by Shi et al. (Shi et al., 2015) characterized the location and incidence of the cervical EFLs and found that superior attachments originated from the lateral margin of the cranial transverse process and were thick and well developed. Inferior attachments originated on both the anterior and posterior tubercles of the caudal transverse process. Several superior and inferior attachments originated from the vertebral pedicle and transverse foramen. Anterior attachments most often originated from the lateral part of the uncovertebral joint, while posterior attachments originated from the capsule of the facet joint. Inferior radiating ligaments had the highest occurrence rate (61.5%), followed by superior radiating ligaments (24.7%), and lastly trailed by anterior (7.5%) and posterior (6.3%) radiating ligaments. The most common spatial orientation of the radiating ligaments was mediocranial to laterocaudal and generally parallel to the spinal nerves, pulling the spinal nerve towards the spinal cord to help resist lateral traction. At the C1/C2 IVF, only one to two radiating ligaments were present, whereas at lower levels (C4-T1), there were four to six. Figure 18 shows an overview of the possible locations of the EFLs.

The second type of EFL, the transforaminal ligament (TFL), typically originated from the anteroinferior margin of the cranial transverse process and spanned the IVF to insert on the superior margin of anterior tubercle of the caudal transverse process, passing the spinal nerve ventrally with a perpendicular orientation (Shi et al., 2015). While the transforaminal ligaments originated and inserted on the adjacent vertebrae, the dorsal side was also firmly attached to the sheath of the spinal nerve, significantly decreasing the available space for the emerging nerve root. These ligaments have been described as strong, thick, and unyielding, and while no formal biomechanical studies have been performed, when tugging on them forcefully with a hook they resisted rupture (Shi et al., 2015). The number of TFLs varied widely between specimens, with some containing up to seven and others containing none (Shi et al., 2015). However, each individual IVF never contained more than one TFL. Figure 18 shows where the TFL is located within the IVF.

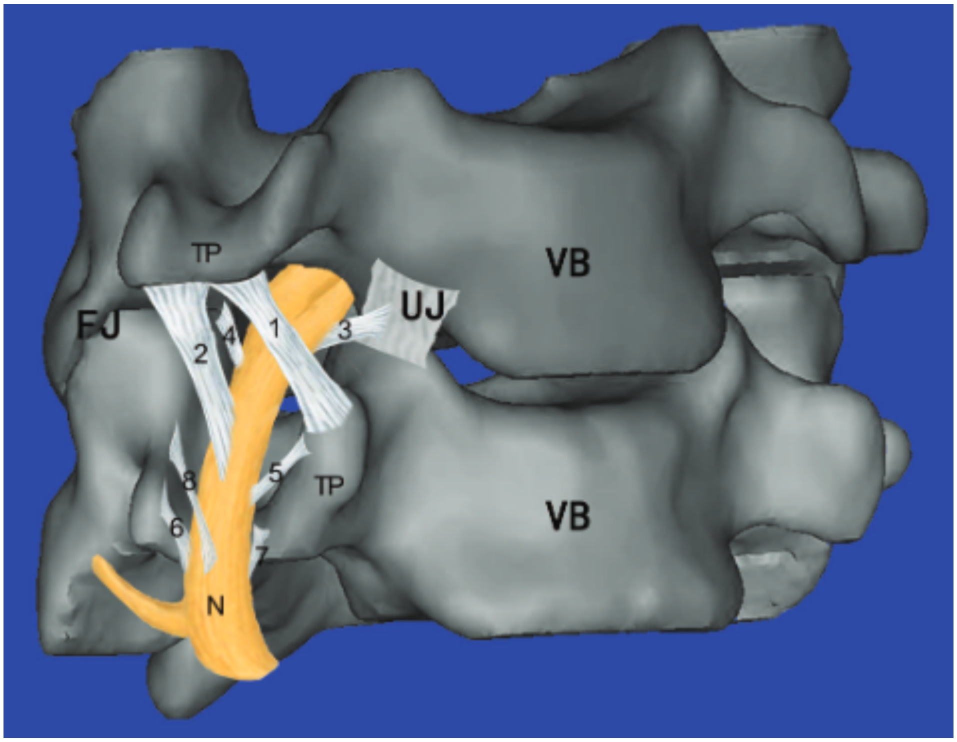

Figure 18: Summary of Possible EFL Attachments within the IVF.
Abbreviations: FJ (facet joint), UJ (uncovertebral joint), VB (vertebral body), TP (transverse process), N (nerve root), TFL (transforaminal ligament), 1 (TFL), 2 (superior radiating ligament), 3 (anterior radiating ligament), 4 (posterior radiating ligament), 5,6,7, and 8 (inferior radiating ligaments). *Source: (Yang et al., 2019)*.

2.2 Mechanical Properties of Nervous and Ligamentous Soft Tissue

Soft tissues in the body typically demonstrate a nonlinear relationship between stress and strain which is dependent on the rate of strain. Because soft tissues are hydrated, their mechanics differ vastly from solid materials, as there is fluid flow within pores and spaces between the tissue layers (Korhonen & Saarakkala, 2011). At slower strain rates, fluid will be allowed to gradually flow within the tissue and act like a compressible sponge. However, at a high strain rate, the fluid will not have time to dissipate slowly throughout the tissue and will act as an incompressible material, which will increase the stiffness significantly. This is one of the main reason why the stiffness of tissues such as articular cartilage is highly dependent on the strain rate (Korhonen & Saarakkala, 2011). Thus, characterizing the Poisson's ratio for the intended strain rate is critical, as it describes the expansion or contraction of a material perpendicular to the loading direction. Dynamic loading scenarios often utilize a Poisson's ratio of 0.5 to represent an incompressible material, while quasistatic scenarios are typically modeled using a lower Poisson's ratio. The white matter and gray matter of the spinal cord, the connecting ligaments (denticulate, foraminal, epidural), and nerves within the spinal column all fall into this category of tissue and care must be taken to correctly represent their biomechanical characteristics in a FEA model.

2.2.1 Peripheral Nerves and Nerve Roots

Nerve mechanical properties and their reported values are influenced by various factors, including their anatomical makeup, the procedures in which they were tested, their spatial scale, type, age, and relative health, making it difficult and expensive to pinpoint quantitative traits experimentally and complicating comparison of results (Paggi et al., 2021). While exact metrics are difficult to compare, nerves behave as a composite anisotropic material, with each component possessing its own unique mechanical properties. The layers of the peripheral spinal nerve (epineurium, perineurium, endoneurium) all possess different mechanical properties that play different roles in the biomechanics of the whole nerve. A study conducted by (Koppaka et al., 2022) where sciatic rabbit nerve perineurium and epineurium tissue was stretched at 0.033 s^{-1} demonstrated that the perineurium in peripheral nerve provided the most stiffness and strength, with an elastic modulus of approximately 3.0 ±0.3 MPa in comparison to 0.4±0.1 MPa for the epineurium within the elastic limit of the tissue. Under an initial tensile load, both the perineurium and epineurium had a linear elastic stress-strain relationship, but as strain increased, the behavior transitioned into a nonlinear region past the elastic limit, shown below in Figure 19. The nonlinear behavior represented the fibers rupturing within the tissue without a complete break, rendering the nerve tissue unable to fully recover its initial deformation (B. Rydevik et al., 2012). Both the perineurium and epineurium exhibited the ability to deform elastically under high strain, with the former's elastic limit at 40% strain and the latter twice as high at 80% strain with numerous linear regions past the initial one that occurred from rupture of individual strands. These results align with the anatomical makeup of the tissue, as the perineurium's structure is layered with tightly packed collagen fibers which contribute to stiffness and protection from penetration and loading, while the epineurium does not have an organized cellular structure but rather contributes to stretching and contracting to facilitate the movement of the nerve (Rosso & Guck, 2019; Sunderland & Bradley, 1961; Walbeehm et al., 2004).

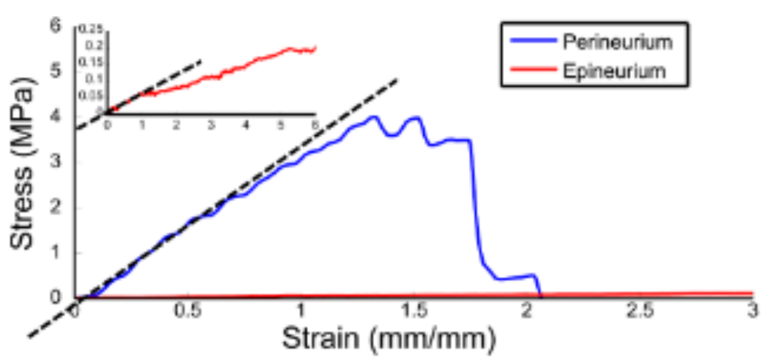

Figure 19: Stress-Strain Behavior of the Perineurium (blue) and Epineurium (red) in Longitudinal Tension.

Source: (Koppaka et al., 2022).

The stress-strain curve of a peripheral spinal nerve is characterized by an initial toe-region of large strain under very little stress (Figure 20). This suggests that when fully relaxed, the nerve fibers possess a crimp or undulation; this has been confirmed in histological studies (B. L. Rydevik et al., 1990). When a longitudinal force is applied, the unfolding of the crimped fibers allows the nerve to undergo strain without sustaining any force (Walbeehm et al., 2004). Once these fibers are fully unfolded, they begin to undergo tension (Walbeehm et al., 2004). Because of this, nerves can undergo extreme strain, reports have shown up to 30%, in normal everyday movements (Phillips et al., 2004). Most biomechanical studies seeking to define the stress-strain behavior of nerves under longitudinal tension report the stretch data from samples that have been excised from the body and allowed to fully relax over a period of time (Kerns et al., 2019; Ma et al., 2013; Wong et al., 2019). Thus, the samples return to their most relaxed state where the crimping of the fibers is present before they are stretched, meaning that a large toe-region is often seen in the data, representing the unfolding of the fibers before they start to withstand any stress. However, within the body, the nerves are often not in this fully relaxed state. A study performed by (Walbeehm et al., 2004) investigated the difference in the tensile stress-strain behavior of nerves that were excised and allowed to relax fully versus nerve segments that were clamped to preserve the in situ organization, tension, length, and diameter of the nerve. They found that the samples with the preserved in situ characteristics displayed no toe-region and instead showed a nearly linear force-displacement relationship, compared to the nonlinear behavior and existence of the toe region in the sample with the relaxed length (Figure 20). This demonstrated that the toe region is an artifact introduced by the excision and resting period of the nerve. Thus, it can be reasonable to utilize linear elastic material models for the definition of nerve material within FE models, as the in situ behavior resembles a linear relationship between stress and strain.

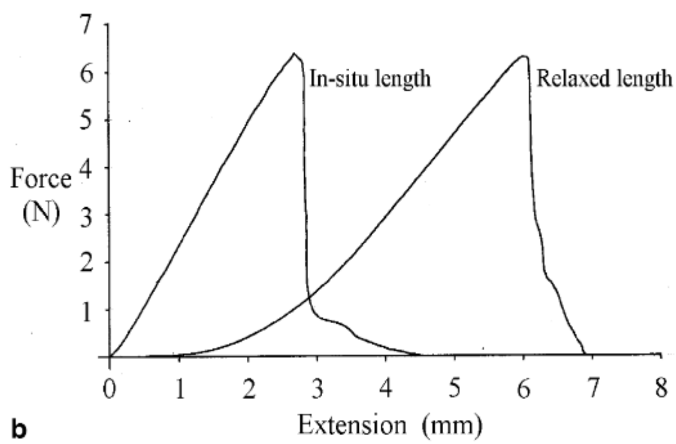

Figure 20: Stress-Strain Behavior of Sciatic Nerve Segments Comparing In-Situ Specimens to Relaxed Specimens.

Source: (Walbeehm et al., 2004).

There have been a multitude of biomechanical studies seeking to accurately characterize the stress-strain properties of peripheral nerves. Table 1 below summarizes the findings from various publications that have carried out uniaxial tension testing of different types of whole nerves at the macroscopic scale. The range of Young's moduli between species, different strain rates and experimental methods are varied and do not follow a discernable pattern but range from approximately 6-58 MPa. Additionally, the amount of strain that the nerves can withstand before breaking is shown to be quite high, ranging from approximately 30-43% according to the studies listed below.

Table 1: Comparison of Peripheral Nerves' Mean Mechanical Properties Under Axial Tension Testing.

Source	Species	Nerve Type	Strain Rate (s^{-1})	Ultimate Strain (%)	Ultimate Stress (MPa)	Young's Modulus (MPa)
(Ma et al., 2013)	Human	Ulnar	0.0011	~	~	5.93*
		Median	0.0023	~	~	5.93*
(Kerns et al., 2019)	Human	Peroneal	0.0033	~	3.88 (1.47)	10.41 (2.85)
		Tibial	0.0033	~	3.91 (0.92)	9.50 (2.84)
(Wong et al., 2019)	Human	Digital	0.0138	32.9	10.34 (n/a)	~
(B. L. Rydevik et al., 1990)	Rabbit	Tibial	0.0033	38.5 (2.0)	11.7 (0.7)	58
(Walbeehm et al., 2004)	Rat	Sciatic (Ex-vivo)	0.2000	41.4 (3.0)	6.15 (0.6)	24.4 (2.4)
		Sciatic (In-situ)	0.2000	29.8 (2.0)	7.2 (0.5)	29.3 (3.2)
(Beel et al., 1984)	Mouse	Sciatic	0.1743	0.43	3.2	7

*Note: Average ultimate stress and strain are reported at the elastic limit. Average Young's Modulus is reported as the slope of the elastic region. Values in parentheses report the standard deviation. *Refers to a value that was calculated by the authors of this thesis from the figures within the listed study.*

Biomechanical characteristics of nerve roots are different than those of peripheral nerves, largely hypothesized to be due to the lack of epineurium and perineurium in the nerve root, which provides much of the mechanical strength and stiffness in peripheral nerves (Koppaka et al., 2022). Without the perineurium and epineurium, the nerve roots within the spinal column can be much more susceptible to deformation (B. Rydevik et al., 1984; Yoshizawa et al., 1995). Nerve roots have been shown to display the same characteristic initial nonlinear toe region under small strain and then linear elastic behavior as strain increases (Beel et al., 1986; Kwan & Rydevik, 1988; Singh et al., 2006; Tamura et al., 2015). The studies that showed a toe-region in their data used the traditional method of excising the sample and allowing the nerve to relax before stretching. Beel et al. (Beel et al., 1986) subjected mouse sciatic nerve roots to a stretch rate ranging from 0.2 s^{-1} to 0.125 s^{-1} and compared their mechanical properties to previously tested mouse sciatic nerves at a similar strain rate (Beel et al., 1984). They found that for the nerve roots, the force at the elastic limit (0.0273N) was approximately thirty times lower than the force at the elastic limit for peripheral sciatic nerves (0.8N). The maximum stress in the nerve roots was 0.302 MPa, only 10% of the stress tolerated by the peripheral sciatic nerves. L5-L4 nerve root stiffness was only 17% of peripheral sciatic nerves, with an average value of 1.19 MPa, showing a small amount of variation between L4 and L5 levels, as well as between the dorsal and ventral root. However, the nerve roots were comparable to the peripheral nerves in elasticity, with 46% and 43% strain at the elastic limit, respectively. To summarize, nerve roots were experimentally determined to withstand much lower maximum load and possessed lower ultimate strength, stiffness, and density than peripheral nerves due to the large structural discontinuities between the two. Thus, small forces transferred directly to the nerve roots would lead to considerable damage. However, a nerve root within an intact IVF and spine is able to withstand larger tensile forces than if it was isolated, as the ligaments and tissues surrounding the nerve root work to dissipate tensile loads. Thus, characterizing the interactions of peripheral nerves and nerve roots with the surrounding tissues is imperative to understanding accurate injury mechanics under loading.

Table 2 below gives a summary of the existing biomechanical data that has been reported for nerve roots. Unfortunately, there are limited studies available that report values for human nerve roots (Kwan & Rydevik, 1988; Sunderland & Bradley, 1961). They do not report stiffness values or clear stress-strain datasets. Additionally, maximum stress values reported by (Sunderland & Bradley, 1961) have a large undefined range that is much higher than any of the other studies listed (Table 2). More comprehensive datasets for mouse, rat, and rabbit nerve roots and pig nerve root fibers have been reported (Beel et al., 1986; Palmerska et al., 2022; Singh et al., 2006; Tamura et al., 2015) which together give insight into the mechanical behavior of the nerve roots. However, because the magnitudes reported for maximum stress vary between species, it is unclear how maximum stress and stiffness values between murine and human values are related, as there is only one dataset reporting maximum stress values with an acceptable range (Kwan & Rydevik, 1988) and stiffness values are not reported for any existing human nerve root study.

Table 2: Comparison of Nerve Root's Mean Mechanical Properties Under Axial Tension Testing.

Study	Species	Strain Rate (s^{-1})	Max Stress (MPa)	Max strain (%)	Young's Modulus (MPa)
(Sunderland & Bradley, 1961)	Human anterior (ventral)	0.0254-0.0635	3.92-27.46	9-15	-
	Human posterior (dorsal)	0.0254-0.0635	5.88-29.42	9-16	-

(Kwan & Rydevik, 1988)	Human (Intradural)	0.0050	1.71 (0.59)	15.22 (3.8)	-
	Human (Foraminal)	0.0050	1.49 (0.44)	18.07 (4.08)	-
(Beel et al., 1986)	Murine	0.1250	0.302 (0.016)	46 (3)	1.19 (0.31)
(Singh et al., 2006)	Murine	0.0008	0.258 (0.111)	29.0 (8.9)	1.3 (0.8)
	Murine	1.2500	0.625 (0.307)	30.8 (8.4)	2.9 (1.5)
(Tamura et al., 2015)	Porcine (Fiber Bundles)	0.0060	0.543 (0.132)	15 (3)	3.80 (1.07)
		0.0600	0.430 (0.242)	13 (2)	3.26 (2.03)
		0.6000	0.713 (0.178)	17 (2)	4.49 (1.07)
(Palmerska et al., 2022)	Lagomorpha	0.0100	0.9 (0.53)	12.73 (4.03)	2.53 (1.00)

Note: Average ultimate stress and strain are reported at the elastic limit. Average Young's Modulus is reported as the slope of the elastic region. Values in parentheses report the standard deviation.

The biomechanical characteristics and interactions of peripheral nerves and nerve roots have been shown experimentally to be complex. Modeling of these nervous structures must take into consideration the anisotropic properties of the tissue, the distinction in strength, stiffness and density between peripheral nerves and nerve roots, and the potential for considerable qualitative changes in the mechanical properties based on the species and characterization method between datasets found in the literature. Many of these considerations have been left unexplored within the existing finite element modeling studies of nerves and nerve roots due to their complexity.

2.2.2 Ligaments Within the Spinal Canal and Intervertebral Foramen

Ligaments are vastly varied throughout the body in their anatomical makeup and function. Ligaments exhibit a generally similar non-linear response to stress compared to nerves, with an initial toe region and then a period of linearity as stress increases. However, there is a vast amount of experimental data that characterizes different biomechanical responses for many different ligaments throughout the body; thus, this thesis will seek to address the biomechanical behavior of only the ligaments which are relevant to the experimental model developed in the methods section, being the denticulate ligaments, foraminal ligaments, and epidural ligaments.

The denticulate ligaments are more well-studied than the foraminal and epidural ligaments, thus there is more data available that describes their mechanical characteristics. A study done by (Polak et al., 2014) subjected porcine denticulate ligament samples to stretching at a strain rate of approximately 0.0167 s^{-1} and reported the force-displacement values. Figure 21 shows an example of the force-displacement data, with a point defined for the end of the toe region and one for the force at breaking. The average values for each point were reported for denticulate ligaments C1-C7. The mean Young's modulus value was 2.06 MPa, indicating a low stiffness and high flexibility of the tissue. The data demonstrated a trend of decreasing toe and failure force at lower levels of the spinal cord, suggesting that the denticulate ligaments are more resistant to breaking at upper and mid-levels of the cervical spine, indicating that the DLs adapt their mechanical properties to meet the diverse loads at different vertebral levels (Polak et al., 2014).

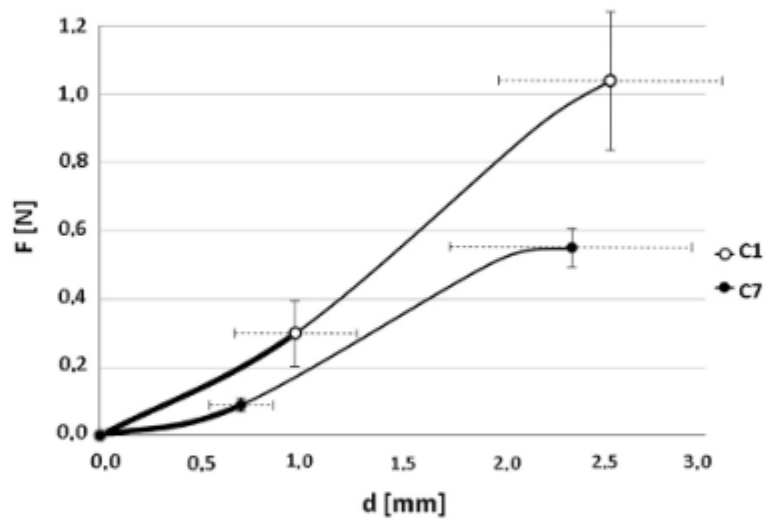

Figure 21: Force-Displacement Behavior of the C1 and C7 Denticulate Ligaments.
The standard deviation bars represent points at the end of the toe region and at the failure force.
Source: (Polak et al., 2014).

While biomechanical data exists for the denticulate ligaments, to this author's knowledge, there are no similar studies that have done tensile stretching tests of the foraminal or the epidural ligaments. Thus, there are no guidelines for what mechanical properties to use when modelling these ligaments. Because they are similar in scale to the DLs, utilizing the mechanical properties presented by (Polak et al., 2014) for the DLs could be an acceptable starting point. However, while no biomechanical data exists for the foraminal and epidural ligaments, their biomechanical functions have been discussed in the literature.

The intraforaminal and extraforaminal ligaments (IFLs) play a role in stabilizing and assisting the nerve root and spinal nerve during movement of the spine and limbs, as the spinal nerves are not static but instead tighten or relax to assist the position of the spine (Akdemir & Neurosurg, 2010). Under normal physiological circumstances, motion of the spine does not cause nerve root injury because the IFLs and the surrounding fat tissue greatly reduce friction and protect the nerve from contact with the surrounding bony structures or other tissues that could cause compression (Yang et al., 2019). Additionally, they prevent abnormal movement or folding of the nerve root sleeves through the duration of spinal movement and help the nerve root to maintain its shape, ensuring that adequate blood flow and electrophysiological transmission occurs within the nerve root (Yang et al., 2019). Shi et al. (Shi et al., 2015) hypothesized that at the cervical level, the extraforaminal radiating ligaments serve to secure the spinal nerve in the center of the IVF which protects it from compression and longitudinal strain. The spinal nerve was observed to be able to move freely within the IVF so that it can accommodate movement of the spinal column, however, because the nerve sheath is fused to the dural sac and anchored to the IVF by the radiating ligaments, the extent of lateral movement is limited during an abnormal traction applied to the spinal nerve (Shi et al., 2015). Thus, the IFLs and EFLs are critical components to include when investigating pain mechanisms within the cervical spine during chronic compression and loading.

The epidural ligaments that anchor the posterior dural sac to the LF and the laminae have been speculated to function as stabilizing structures that constrain the dura mater to the movement of the spine (Shi et al., 2014). Additionally, they assist in preventing the dura mater from folding in on itself and in dissipating dural tension (Shi et al., 2014). Thus, they are important to consider when developing a model of the spinal column that will undergo movement. More in-depth studies into the biomechanical properties of the epidural and foraminal ligaments should be performed to further the accuracy of modeling these tissues.

2.3 Cervical Spine Radiculopathy

Radicular pain can be caused by compression of the nerve roots that leads to dysfunction (Caridi et al., 2011). Suggested mechanisms of radicular pain include narrowing of the foraminal space, ligament ossification, and bulging and herniation of the intervertebral disks (Humphreys et al., 1998). Nerves, nerve roots and DRGs are highly sensitive tissues and because they are tethered to a dynamic spine, there are many conditions that can lead to tension or compression injuries (Kitab et al., 2009). The following is an overview of the anatomical components that most commonly cause compression of the nerve root, which are the bony vertebral structures, vertebral ligaments, and IVDs. Additionally, the thresholds of critical pressure that cause pain via deformation, blood flow restriction, and impaired action potential propagation are reviewed, in addition to the long-term effects on nerve structure after chronic compression.

2.3.1 Nerve Root Compression Mechanisms

Within the anatomy of the spinal column are many tissue structures that can cause compression of the nerve roots, with the most commonly reported being the bony structures of vertebrae, the ligaments, and IVDs. The primary purpose of the vertebrae surrounding nervous tissue is protection; however, there are many ways for bony structures to compress nerves. Nerve roots are particularly susceptible to foraminal compression from head movements (B. L. Rydevik et al., 1989), more often compressed on the outer edge of the intervertebral foramina compared to the inside (Hasue et al., 1983; B. L. Rydevik, 1992). Additionally, the pedicle of the vertebral arch often is responsible for compressing the nerve roots superiorly, while the articular facets are most often responsible for inferior compression. More severe disorders such as isthmic spondylolisthesis, which occurs when one vertebra slips onto the vertebra below it, can cause a flattening of the foraminal space, trapping the nerve root and forcing the nerve root to travel more posteriorly than its normal path (K. W. Kim et al., 2004). A study by (K. W. Kim et al., 2004) examined 38 nerve roots in adults with isthmic spondylolisthesis and radicular pain and found that 26 of the 38 nerve roots were entrapped or impinged in the foramen. This shows a strong correlation between radicular pain and foraminal compression.

Like the vertebrae, ligaments are intended to protect nervous tissue and neutralize the stress put on the nerve roots by tethering to the inside and outside of the foramina to minimize movement (Kitab et al., 2009). When ligaments connecting to the nerve roots function properly, the strain limitation allows action potentials to continue firing which facilitates adequate blood flow and prevents permanent deformation in roots (Lohman, 2014). The IFLs, EFLs, and the PLL are the primary ligaments that have been studied in relation to nerve root compression.

IFLs and EFLs are the primary limiters of nerve root displacement, but there is a discrepancy in the magnitude of restraint between the two, as the intraforaminal ligaments contribute a higher amount of stabilizing force (Lohman, 2014). When the strain in the nerve roots is large or dynamic enough, a sizable strain gradient can occur within the foramina that can generate damage and pain (Lohman, 2014). Furthermore, direct contact of these ligaments with the nerve root can cause compression and pain, most often arising from ligament ossification in which changes to the histological composition of the ligament cause hardening and loss of flexibility in the ligament (Lohman, 2014).

With aging, it is not uncommon to see structural changes occur that cause ossification in the vertebral ligaments, increasing their stiffness and the risk for nerve root compression (Loeser, 2010). Ossification of the PLL has recently been shown to occur primarily in the cervical spine and rarely in the thoracic and lumbar spine (Hasue et al., 1983; Y. H. Kim et al., 2013). Segmental ossification of the PLL can form a complete barrier through the CSF between the PLL and spinal cord, indirectly cutting off nutrient flow to highly metabolic structures like the DRG, resulting in deterioration (Khuyagbaatar et al., 2015).

Another structure that can cause nerve root compression in daily movements of the cervical spine is the IVD. With aging and continuous loading, it is common for IVDs to deteriorate, making it easier for the nucleus to slip out of alignment from its typical location within the center of the vertebral body. As a result, the annulus can bulge over the edge of the vertebral body, resulting in a shortening of the IVD and/or compression of the surrounding tissues (Li et al., 2014). Nowicki et al. (Nowicki et al., 1996) studied the effects of IVD degeneration on occult stenosis, which is a narrowing of the foraminal space that results in nerve root compression via head movement. They found that 100% of advanced degenerated disks produce occult stenosis in the cervical spine. Furthermore, occurrence was 73% in disks with radial tears and 49% in aging disks. However, in young, healthy IVDs, there was a 0% occurrence of occult stenosis. These results show that deteriorated IVDs, which are very common with aging and chronic loading, only amplify the chances of bony structures compressing and impeding nerve root function. A summary of these structures and how they compress nerve roots is shown below in Figure 22.

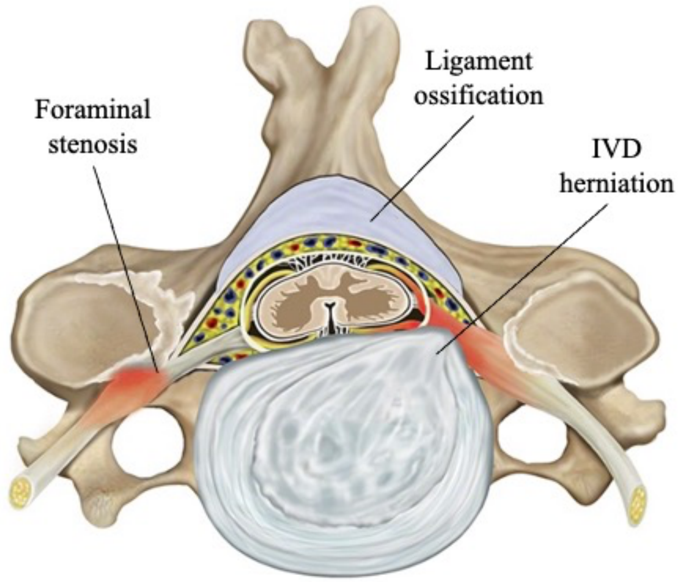

Figure 22: Possible Sources of Nerve Root Compression.
The three sources discussed that are displayed above are the vertebrae (foraminal stenosis), ossified ligaments with increased stiffness, and bulging or herniation of the IVD. *Source: [Adapted from (Culley, n.d.)].*

2.3.2 Nerve Pain Mechanisms

There has been an abundance of research done to examine how compression of the nerves generates pain. One of the main factors that has been considered is the cutoff of blood flow within the nerves. Without blood flow, the nerves cannot be supplied with nutrients, resulting in nerve deterioration, increasing the risk of pain(Sens et al., 2020). Additionally, compression and blood flow restriction to the DRG can have a detrimental effect on the function of nerves and nerve roots. The DRG require twice the amount of blood flow compared to the rest of the nerve root because they house the cell bodies of sensory axons (Kitab et al., 2009).

Another factor that could contribute to pain generation during compression of the nerve roots is the formation of an edema, which is a buildup of fluid within a tissue. Compression of the nerve root can cause the endoneurial capillaries to leak (B. Rydevik et al., 2012), causing swelling within the tissue due to trapped fluid. This swelling leads to an increase in the intraneural pressure and in turn decreases the permeability of the nerve root, impairing nutritional transport and causing further damage to the nerve (B. L. Rydevik, 1992; B. L. Rydevik et al., 1989). Locations where the nerve roots are tightly enclosed by connective tissue, such as at the DRG, are more susceptible to entrapment and edema formation (B. Rydevik et al., 2012). Because edemas do not disappear when compression is relieved, it is likely that this decreased permeability persists longer than the applied compression. If severe enough, this can also lead to intraneural fibrosis, which hardens the nerve, prolonging recovery even longer as the nerve would lose its ability to fold and unfold under tension (B. L. Rydevik, 1992). Thus, compression of the nerve roots does not only directly cause pain, but it can also cause long term structural impairments, even when compression is not present.

Lastly, ectopic firing within a compressed nerve root has also been speculated to be a cause of pain in cervical radiculopathy. Ectopic firing is when injured neurons produce spontaneous activity that is generated away from normal impulse generation sites, and has been demonstrated to play a large role in neuropathic and radicular pain (Sugawara et al., 1996). Ectopic firing begins likely due to blood vessel constriction once a certain threshold of critical pressure has been surpassed (Sugawara et al., 1996).

Other studies have investigated the incidence of chronic compression over months. Yoshizawa et al. (Yoshizawa et al., 1995) conducted a study examining the effects of compressing a canine lumbar nerve root with a siliconized rubber tube for up to 12 months. After one month, changes in the blood-nerve barrier produced a thickening of the dura mater and arachnoid membrane, making it more difficult for nutrients to enter the nerve. At three months, visible scar tissue began to form around the nerve root, with drastic changes in histological composition, as there was a decrease in large, myelinated fibers, leading to decreased compound action potentials. Additionally, an increase in smaller fibers in the periphery of the fascicle and a slight increase in collagen fibers was observed. After 6 months, the scar tissue was even more prominent, and degradation of axons distal from the site of injury and hardening of the endoneurium from excess collagen deposition was apparent. Finally, at 12 months the scar tissue was the most prominent, and all of the large, myelinated fibers had disappeared, significantly decreasing sensory nerve conduction. Ultimately, the researchers determined that these results stemmed from alterations in the blood-nerve barrier that were caused by an intra-radicular edema (Yoshizawa et al., 1995). A summary of the factors that contribute to pain and dysfunction in the nerve due to compression is presented below in Figure 23.

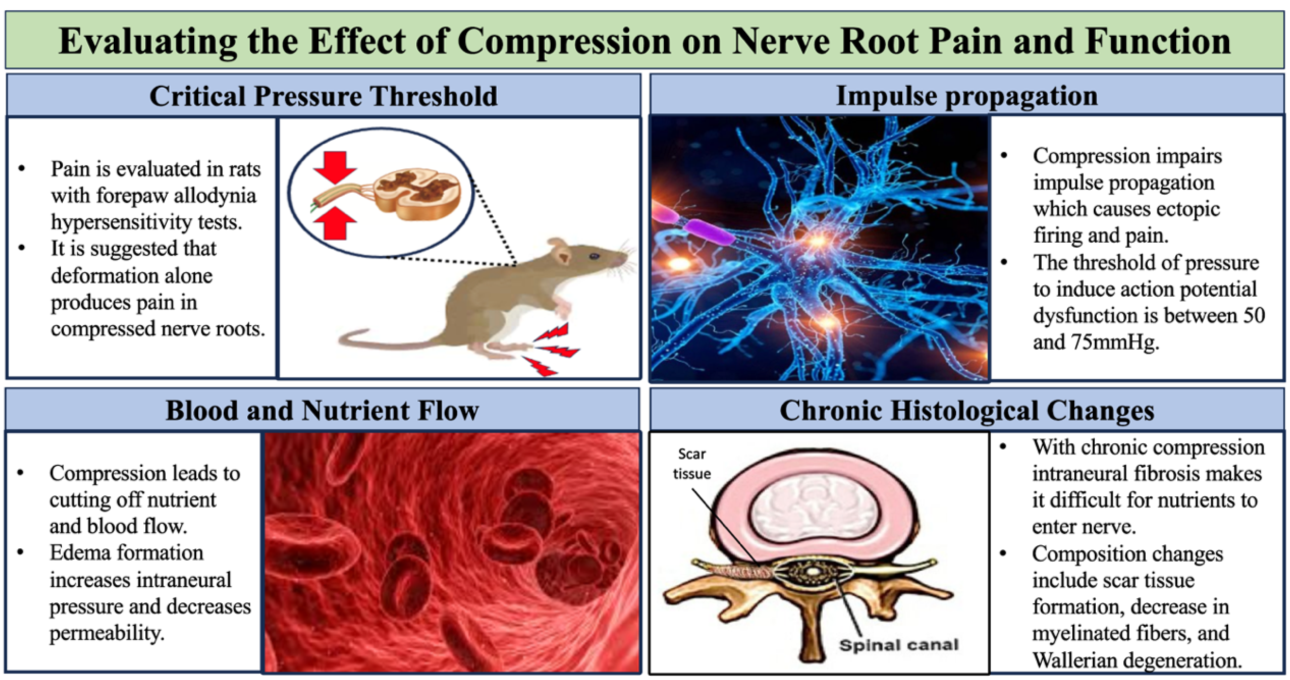

Figure 23: A Summary of the hypothesized mechanisms of pain in NR radiculopathy.
Top left: research has shown that deformation of the nerve roots demonstrates an allodynia pain response in rats. Bottom left: summary of consequences due to restricted blood flow within the nerves. Top right: effects of restricted impulse propagation

within the nerves. Bottom right: Summary of histological changes seen in the nerve root due to chronic compression. *Source: [Adapted from (Dalton, 2017; DBCLS, 2014; Membranpotensial og nerveimpuls - Biologi 1 - NDLA, n.d.; Neuromuscular Junctions and Muscle Contractions, n.d.; Free Images, n.d.; Royalty-Free Photo: Blood Cells Illustration, n.d.; Spinal Cord Segments and Spinal Roots, n.d.)].*

2.4 FE Nerve Models of the Spine

There have been several studies that have laid fundamental groundwork in FE modeling of nerve-tissue mechanics. The following will summarize models that were found from a comprehensive review that was done in two databases, Scopus and PubMed, using keywords searching for any implementation of nerve finite element modeling. There are two existing patterns that have emerged from the literature, the first being biomechanical modeling of spinal nerves under various loading applications to investigate the resulting stresses and strains within the neural tissues. The second is investigating the effect of electrical stimulation within the spinal column on electrical interactions with surrounding tissues or implants for insight into spinal cord stimulation used for relief of pain in radiculopathies. The focus of this research is modeling biomechanical interactions between nerve roots and tissues under loading; thus, a summary will be given to the studies which incorporate mechanical properties of spinal nerves, and the electrical studies will be left out due to the scope of this review.

Starting with examples of lower complexity, Shin et al. (Ah Shin et al., 2016) used 2D nonlinear FE analysis to examine the effects of epidural adhesions on spinal nerve roots. An epidural adhesion was modeled at the L4/5 level, with geometry creation achieved with a CT scan of a 24-year-old male with a disk protrusion, including the nucleus pulposus, annulus fibrosus, dura mater, cauda equina, spinal nerve, and lamina (Figure 24). Because IVDs are the most crucial element when dealing with epidural adhesions, the annulus fibrosis and nucleus pulpous were modeled with Mooney-Rivlin constitutive models. The remaining geometry was modelled with linear elastic material properties. However, the references reported were papers focused on defining material models for the gray and white matter of the spinal cord, which is not modelled in this study. Thus, it is unclear where the values used for the dura mater, spinal nerve, and lamina originated. Ultimately, they discovered a large stress concentration on the spinal nerves under the epidural adhesion condition, specifically in the DRG location. These are informative results, but they are limited in their contribution to modeling nerve root-tissue interaction within the spine because the model is two dimensional and has yet to be validated alongside any experimental data.

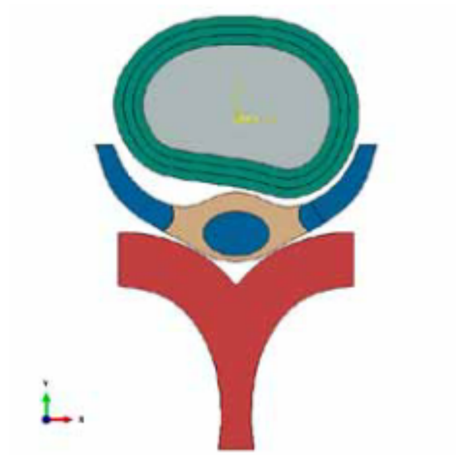

Figure 24: 2D FEM of the Lamina (red), Dura Mater (white), Spinal Nerve and Cauda Equina (blue), Nucleus Pulposus (gray), and the Annulus Fibrosis (green).
Source:(Lee et al., 2016).

Two simplified three-dimensional models of the cervical vertebrae and nervous structures have also been established. Kim et al. (H. J. Kim et al., 2009) developed a model of the lumbar vertebrae incorporating nerve roots to investigate the pathomechanics of nerve root symptoms in degenerative lumbar scoliosis, where spinal column misalignment often results in compression of the nerve roots. The model was validated by applying the same loading conditions from a cadaveric study examining the movement of the lumbar spine (Yamamoto et al., 1989) and found results within one standard deviation of the in vitro study. The model included four lumbar vertebrae, intervertebral discs with three distinct components, and seven vertebral ligaments (Figure 25). Additionally, the model contained a simplified structure representing the spinal cord and the nerve roots; however, it was modelled as the same part and did not distinguish between them. Another example by (Mihara, 2018) developed a model of the brachial plexus, which is a grouping of spinal nerves that extend from the cervical nerve roots, to investigate prevention of brachial plexus injuries. The model included vertebrae and IVDs from C2 to T2, the first and second rib and corresponding cartilage, and the right clavicle, scapulae, and humerus (Figure 26). Nerve structures included the brachial plexus, which was modelled with a simplified structure that extended the right C5-T1 spinal nerves from a column representing the layer of dura mater that travels through the spinal canal and surrounds the spinal cord (Figure 26). Both neural components in these studies were modelled using linear elastic properties reported from (Beel et al., 1986; Nishida et al., 2015; Singh et al., 2006).

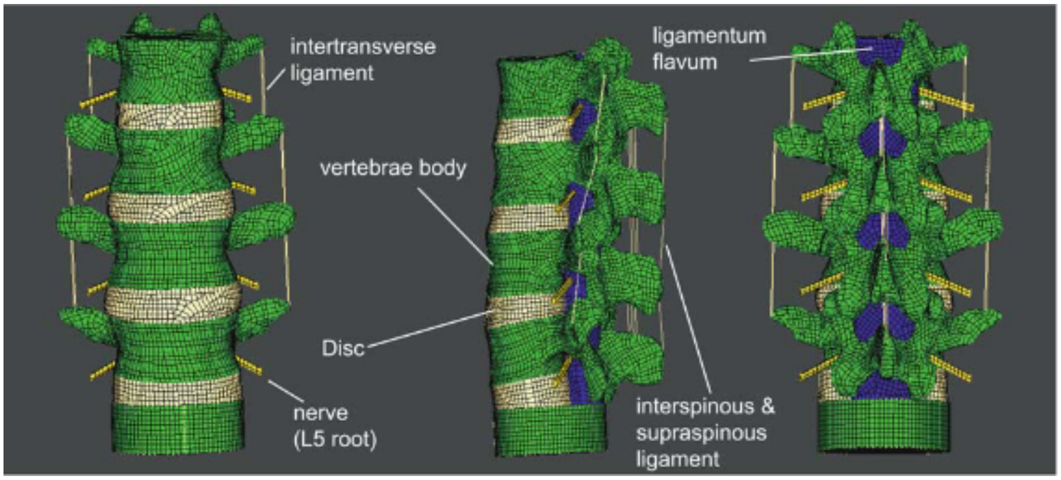

Figure 25: FEM of the Lumbar Spine Including Vertebrae, Ligaments, IVDs, and Nerve Roots.
Source:(H. J. Kim et al., 2009).

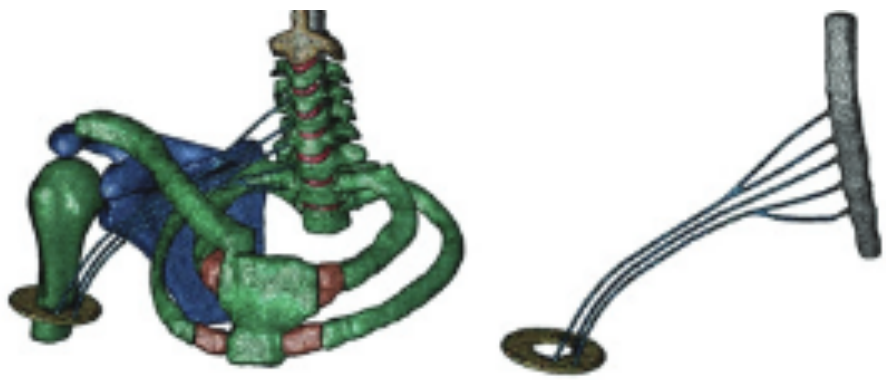

Figure 26: FEM of (left) the Cervical Spine, the First and Second Rib and Corresponding Cartilage, the Right Clavicle, Scapulae, Humerus and (right) Brachial Plexus.
Source: (Mihara, 2018).

Several limitations arise from these studies, the first being the simplification of the neural geometry, leaving out many important tissues within the spinal column that contribute to interactions that could dampen or increase the stress of the nerve roots under loading conditions. Examples of the tissues that were left out include the meninges, CSF, anatomically correct dura mater, root sheath, dorsal root ganglion, nerve rootlets, denticulate ligaments, epidural ligaments, and foraminal ligaments. Additionally, in the study by (H. J. Kim et al., 2009), the free ends of the nerve roots were constrained in all directions, which is not representative of real-world conditions as the nerve roots have been shown to move within the IVF (Akdemir & Neurosurg, 2010). Additional improvements would be to define the distinction in material properties between the spinal cord and nerve roots, and to utilize the well-defined hyperelastic material models that exist for the spinal cord. Further development of models like these would benefit greatly from attempting to distinguish the differences in structure and detail between the nerves and the spinal cord, as well as including the other tissues mentioned within the spinal column that are vital to the biomechanical ecosystem, in addition to validating stress and strain values under prescribed loading conditions alongside experimental data in these tissues.

Two models to date stand out as the greatest contributors to modeling mechanical interactions of nervous structures within the spinal canal and IVF. The first is a group of cervical spine models developed between 2013-2018 by Batbayar Khuyagbaatar, a biomechanist based out of Mongolian University of Science and Technology. He and his team have developed one of the most detailed models of the spinal canal to date that has been used for a variety of applications investigating maximum stress, strain, and displacement of both the spinal cord and the nerve roots under certain loading conditions. Over the course of the past decade, they developed and built upon an original FE model of the spinal cord, gradually adding components throughout the years. The first iteration of the isolated spinal cord (Y. H. Kim et al., 2013) was validated by comparing the force-deformation and stress strain curves of the spinal cord under compression to experimental studies (Hung et al., 1982; Ichihara et al., 2001). The later addition of the dura mater and CSF to the model was validated by comparing the maximum deformations of the spinal cord within the dural sheath to two experimental studies (Khuyagbaatar et al., 2014). However, the addition of the nerve roots, nerve rootlets, and denticulate ligaments has not yet been validated alongside any experimental studies.

Khuyagbaatar et al.'s most recent model (Khuyagbaatar et al., 2018) investigated tissue mechanics of the nerve roots and spinal cord following laminectomy and laminoplasty, which are surgical treatments used to relieve stress on the spinal cord caused by ossification of the posterior longitudinal ligament (OPLL). The von Mises stress, posterior shift of the spinal cord, and displacement caused by tension of the right and left extradural nerve roots in pre- and post-operative models were investigated. The model contained vertebrae C2-T1, intervertebral discs, vertebral ligaments, white and gray matter of the spinal cord, CSF, dura mater, denticulate ligaments, nerve rootlets, and nerve roots (Figure 27). The dura mater surrounded the CSF and the nerve roots as one continuous part. The nerve roots and nerve rootlets were separated into two distinct parts, with the nerve roots defined as originating lateral to the CSF and exiting the foraminal space while the nerve rootlets connected the spinal cord to the nerve roots and laid within the CSF. The denticulate ligaments connected the spinal cord to the medial surface of the dura mater. This representation of the geometry within the spinal canal is a substantial improvement to the simplified models discussed earlier in this section, as it includes distinct white and gray matter of the spinal cord, denticulate ligaments, dura mater, nerve roots, and nerve rootlets.

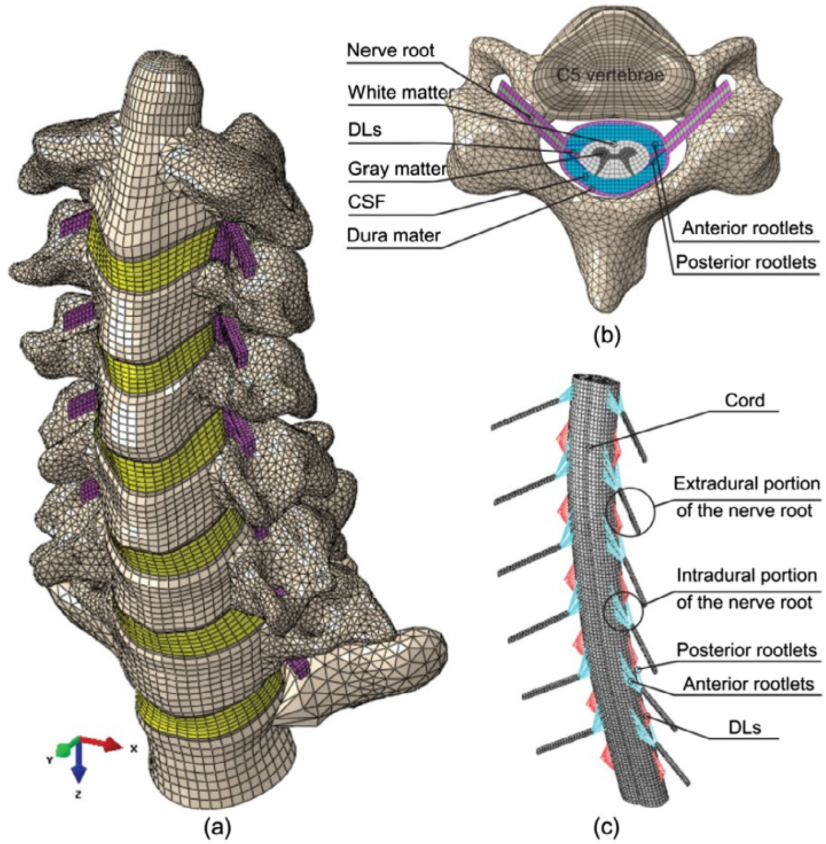

Figure 27: 3D FEM of the Cervical Spine with Detailed Neural Structures Within the Spinal Column.
(a) Full assembly of the cervical spine and soft tissues, (b) cross-sectional axial view of the spinal cord at the C5 vertebrae, (c) spinal cord with nerve rootlet and DL attachments securing the nerve root.
Source:(Khuyagbaatar et al., 2017).

The second important contribution to detailed nerve models of the cervical spine are the models published by Xue et al. (Xue et al., 2021, 2023). They replicated the work done by Khuyagbataar et al. (Khuyagbaatar et al., 2016, 2017, 2018) to study the biomechanism of spinal cord injury due to OPLL during Cervical Spinal Manipulation, a treatment used to treat nonspecific mechanical neck pain. The tissues and their geometrical configurations were the same as (Khuyagbaatar et al., 2018), with the only exception being the addition of the pia mater surrounding the lateral surface of the white and gray matter, and a slightly different configuration of the denticulate ligaments (Figure 28). This model was validated by applying a rotation of ±20º around the x-axis to simulate both flexion and extension, where the anterior/posterior (A/P), superior/inferior (S/I), and right/left (R/L) relative displacements of the C3-C7 spinal cord were compared alongside the in-vivo MRI data published by (Stoner et al., 2019). Xue et al. (Xue et al., 2021, 2023) also performed the same validation method used by Khuyagbataar (Khuyagbaatar et al., 2016, 2017, 2018) comparing the force-deformation curve of the spinal cord under a concentrated load of 0.8 N to the in vitro study by Hung et al. (Hung et al., 1982). In both simulations, their model's results fell within the mean value ± standard deviation (SD) reported, matching the experimental values well.

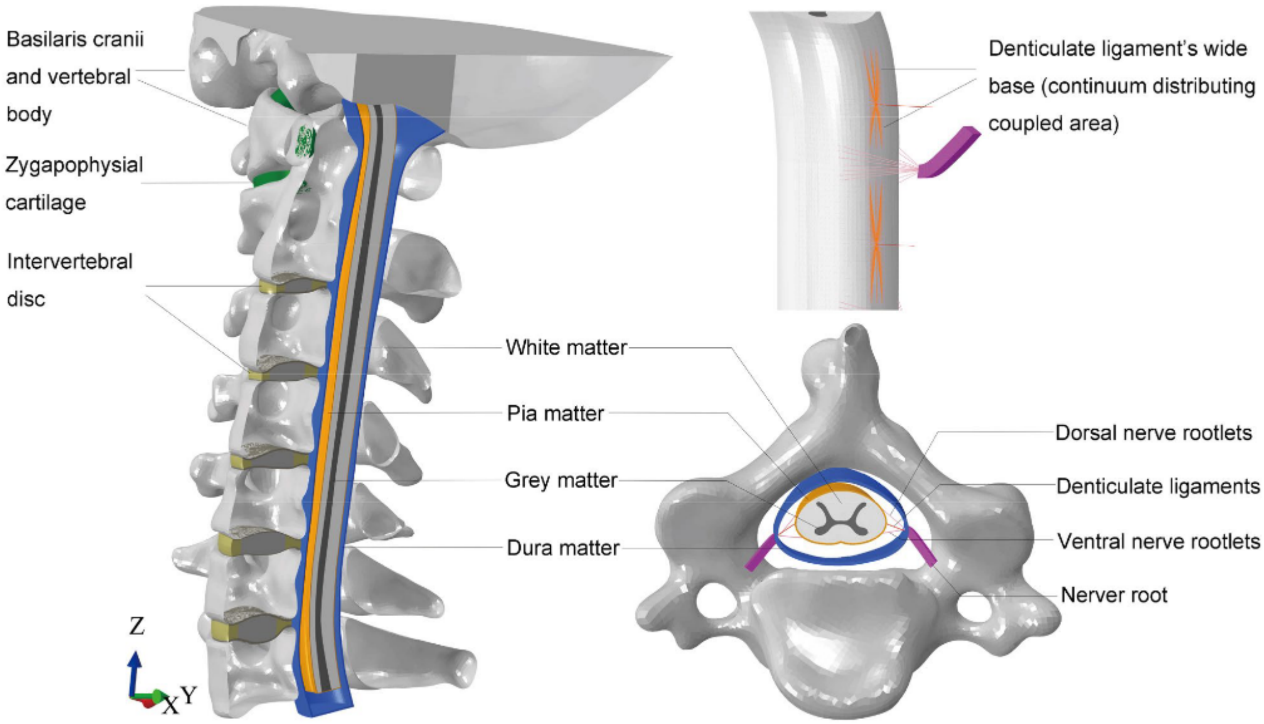

Figure 28: FEM of the Cervical Spine and Neural Soft Tissues.

Source:(Xue et al., 2021).

Both models by Khuyagbataar et al. (Khuyagbaatar et al., 2017, 2018) and Xue et al. (Xue et al., 2021, 2023) utilized the same linear elastic material properties for the dura mater and nerve root from (Persson et al., 2010) and (Singh et al., 2006), and used the same Ogden hyperelastic material models defined by (Ichihara et al., 2001) for the white and gray matter. Differences between the two studies arose in the element definitions of the CSF, where Khuyagbataar et al. (Khuyagbaatar et al., 2017, 2018) utilized fluid Eulerian elements, defined as an arbitrary collection of cubic elements that fill the entire region of the fluid. The fluid-solid material interaction was coupled using Eulerian-Lagrangian analysis using Explicit (ABAQUS™, ABAQUS Inc., Providence, RI, USA). In contrast, Xue et al. (Xue et al., 2021, 2023) defined the CSF as solid hexahedral elements that were converted to mass particles at the beginning of the analysis, where the interaction between the CSF and solid bodies was investigated through the smoothed-particle-hydrodynamics (SPH) analysis method using ABAQUS 2020 (ABAQUS™, ABAQUS Inc., Providence, RI, USA). Both models utilized Newtonian fluid characteristics. Other differences were the use of nonlinear tension-only springs vs 3D truss elements for the nerve rootlets and denticulate ligaments. Boundary conditions for both models included fixing the superior and inferior surfaces of the spinal cord, CSF and dura mater at their respective ends at C2 and T1. Khuyagbataar et al. (Khuyagbaatar et al., 2017, 2018) defined the distal nodes of the nerve roots as free to move only in the longitudinal direction, while Xue et al. (Xue et al., 2021, 2023) instead coupled the distal surface to the adjacent vertebral body, ensuring consistent movement between the two, which can be argued is more biofidelic, as the nerve root has been shown to move within the IVF (Akdemir & Neurosurg, 2010).

Table 3 below summarizes the mechanical properties utilized for the CSF, gray and white matter, nerve root, dura mater, nerve rootlets and denticulate ligaments across the five studies that were reviewed. The material properties utilized by (Ah Shin et al., 2016) can be difficult to replicate, as the references cited were not relevant to the tissues modeled, making it unclear where the values originated from. Additionally, the stiffness values used (1MPa for dura, 40.96 MPa for nerve root) were not within ranges reported in the literature. All five of the studies reviewed included nerve aspects within their FE models and chose to use linear elastic material models. Improvements in complexity and anatomical accuracy were exhibited by Khuyagbataar et al. (Khuyagbaatar et al., 2017, 2018) and Xue et al. (Xue et al., 2021, 2023). However, there is still a lack of validation studies that specifically aim to verify the accuracy of the stress-strain values and behavior of nerve roots interactions, likely due to the lack of availability of comparable experimental studies. Further improvements to consider would be the incorporation of the vast network of connective ligaments and tissues that constrain and dissipate forces of the nerve roots and spinal cord, such as the foraminal and epidural ligaments. Additionally, the inclusion of the DRG could help further understanding of how the vertebrae and other surrounding tissues interact with the nerve root during compression. Furthermore, incorporating the tissues within the spinal canal into a fully comprehensive model of the head-neck complex could open a wider variety of applications for investigation of injury and pain in the cervical spine.

Table 3: Summary of Material Properties Utilized Across Five Nervous Cervical Spine FEMs.

Material	Category	(H. J. Kim et al., 2009)	(Lee et al. 2016)	(Mihara, 2018)	Khuyagbaatar et al. (2013-2018)	Xue et al. (2021-23)
CSF	*Model*	-	-	-	ALE Elements, Newtonian	SPH Elements, Newtonian
	Parameters	-	-	-	η = 0.001 Pa*s	η = 0.0008 Pa*s co = 1381700 mm/s s = 1.979 Γ0 = 0.11
	Reference	-	-	-	(Bloomfield et al., 1998)	(Jannesar et al., 2021; Panzer et al., 2012)
White Matter	*Model*	-	-	-	Hyperelastic (Ogden)	Hyperelastic (Ogden)
	Parameters	-	-	-	μ = 4.0 kPa, α = 12.5	μ = 4.0 kPa, α = 12.5
	Reference	-	-	-	(Ichihara et al., 2001)	(Ichihara et al., 2001)
Gray Matter	*Model*	-	-	-	Hyperelastic (Ogden)	Hyperelastic (Ogden)
	Parameters	-	-	-	μ = 4.1 kPa, αf = 14.7	μ = 4.1 kPa, αf = 14.7
	Reference	-	-	-	(Ichihara et al., 2001)	(Ichihara et al., 2001)
Dura Mater	*Model*	-	Linear Elastic	Linear Elastic	Linear Elastic	Linear Elastic
	Parameters	-	E = 1 MPa ν = 0.49	E = 129 MPa ν = 0.40	E = 80 MPa ν = 0.49	E = 80 MPa ν = 0.49
	Reference	-	Unclear	(Tencer et al., 1985)	(Runza et al., 1999)	(Runza et al., 1999)
Nerve Root	*Model*	Linear Elastic	Linear Elastic	Linear Elastic	Linear Elastic	Linear Elastic

	Parameters	E = 1.19 MPa ν = 0.44	E = 40.96 ν = 0.37	E = 2 MPa ν = 0.40	E = 1.3 MPa ν = 0.3	E = 1.3 MPa ν = 0.3
	Reference	(Singh et al., 2006)	Unclear	(Nishida et al., 2015)	(Singh et al., 2006)	(Singh et al., 2006)
Nerve Rootlet	*Model*	-	-	-	Nonlinear tension-only spring	Elastic plastic 3D truss
	Parameters	-	-	-	Nonlinear force-displacement	Stress-strain curve
	Reference	-	-	-	(Singh et al., 2006)	(Singh et al., 2006)
Denticulate Ligaments	*Model*	-	-	-	Nonlinear tension-only spring	Elastic plastic 3D truss
	Parameters	-	-	-	Nonlinear force-displacement	Stress-strain curve
	Reference	-	-	-	(Polak et al., 2014)	(Polak et al., 2014)

CHAPTER 3: METHODS

3.1 Project Approaches and Aims

This thesis proposal encompasses one part of a larger project to investigate mechanisms for chronic neck pain in navy pilots through FE modeling. To the author's knowledge, there has not yet been any FE models that investigate the location and occurrence of nerve root compression in the spine under helmet loading conditions. Thus, the aim of this thesis is to contribute to the development of models that are subject-specific to pilots by creating a FEM of the neural structures and soft tissues found within the spinal column and intervertebral foramen and integrating it into an existing model of the head-neck complex.

The existing model of the head-neck complex that will be built upon is the VIVA OpenHBM 50^{th} percentile female head-neck model, which has been validated under multiple different dynamic loading scenarios (Östh et al., 2016, 2017). The VIVA OpenHBM is a head-neck complex made up of a skull, jaw, hyoid bone, vertebrae, intervertebral disks, vertebral joint tissues, ligaments, 1D muscle elements, and the soft tissues lateral to the vertebrae within the back and neck, encompassing over 423 individual parts with distinct material models and contact definitions (Figure 29). However, the spinal canal and intervertebral foramen do not contain any tissues. Thus, the goal of this thesis is to add the neural structures discussed in the anatomy section to the empty spaces in the VIVA OpenHBM. The newly adapted model developed in this thesis will be referred to as the Nerve CSM, where CSM stands for cervical spine model. All simulations were developed and processed in LS-Prepost (LS-PrePost 4.10, © 2024 DYNAmore GmbH, an Ansys Company, Hauptniederlassung Stuttgart) and run in LS-Run (LS-Run 2024 R1, © 2024 DYNAmore GmbH, an Ansys Company, Hauptniederlassung Stuttgart).

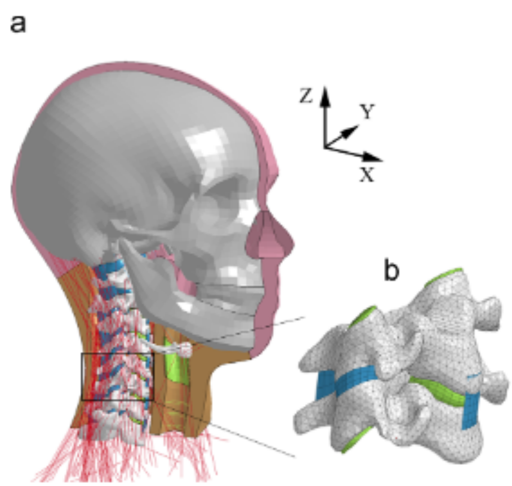

Figure 29: Head-Neck FEM of the Skull, Cervical Spine, and Surrounding Components.
(a) Right lateral view of the VIVA OpenHBM, (b) right lateral view of the isolated vertebral structures**.**
Source:(Östh et al., 2017).

Obtaining solutions with FE modelling that accurately represent real-world mechanics requires rigorous attention, as the results are arbitrary unless validated through comparison to physically conducted experimental results. Thus, validating the current model by recreating a simulation that replicates an experimental procedure is critical to the trustworthiness of the results. Validation methods commonly utilized are observing if the simulated data falls within data corridors that are based upon the standard mean and deviation of an experimental dataset. Validation of results is typically accepted if the simulated data falls within the data corridors of the experimental data.

Additionally, ensuring a model's accuracy requires an investigation into if the results adhere to physical laws, most importantly, the conservation of energy. To ensure that no imaginary energy is being added to the model, the global energy must be checked to confirm that there is balance by making sure that the artificially introduced energies, such as hourglass or damping energies are low compared to the total energy (Burkhart et al., 2013).

Most importantly, it is required that validation considerations state the intended use of the model, where some comparison takes place that considers the full application of the model. For example, an FE model to analyze the location and intensity of bone fractures should be compared to experimental data that reports the location and intensity of bone fractures in the real-world. This is one big limitation of the Nerve CSM, as there is an incredibly sparse amount of experimental data available which could validate the behavior of the nerve roots and the foraminal and epidural ligaments. However, it was important to establish that the soft tissues in this model that are replicated from other studies (e.g. the spinal cord) behaved in an accurate way. Thus, this thesis sought to establish that the behavior of the newly added soft tissues did not significantly alter the global biomechanics of the VIVA OpenHBM whiplash simulation that has already been validated, and to establish biofidelic movement of the spinal cord within the spinal canal during flexion/extension movements. Thus, this thesis has three main aims as follows:

Aim 1. To develop the Nerve CSM by incorporating the soft tissues of the spinal canal and intervertebral foramen into the existing VIVA OpenHBM Model. The tissues added will consist of the gray and white matter, CSF, dura mater, root sheath, nerve root, dorsal root ganglion, nerve rootlets, spinal nerve, and denticulate, foraminal and epidural ligaments. This also includes the definition of appropriate material models, boundary conditions and contacts between the new and existing parts. This aim will also include a mesh quality assessment.

Aim 2. To validate the global kinematics of the new Nerve CSM compared to the original VIVA OpenHBM. This will be done by running the new Nerve CSM alongside the original VIVA OpenHBM in the Mid 2.3 m/s whiplash simulation prescribed by (Östh et al., 2017) and comparing the head x-displacement of the skull relative to T1.

Aim 3. To validate the motion of the spinal cord relative to the vertebrae in the Nerve CSM alongside experimental data. This will be done by applying flexion/extension to the model and comparing the anterior/posterior (A/P), superior/inferior (S/I) and right/left (R/L) displacement of the spinal cord to experimental MRI data published by (Stoner et al., 2019), as done by (Xue et al., 2021).

3.2 Aim 1: Development of the Nerve CSM

3.2.1 Creation of Anatomical Geometry

SolidWorks (SOLIDWORKS® 2023, Dassault Systèmes-SolidWorks Corporation, Waltham, MA, USA) was used to construct the geometry of the white matter, gray matter, CSF, dura mater, root sheath, nerve root, and spinal nerve according to anatomical descriptions given in the literature. The ligaments were created in LS-Prepost (LS-PrePost 4.10, © 2024 DYNAmore GmbH, an Ansys Company, Hauptniederlassung Stuttgart). To construct the soft tissue geometry housed within the spinal canal, it was necessary to import the vertebral geometry of the VIVA OpenHBM into SolidWorks (SOLIDWORKS® 2023, Dassault Systèmes-SolidWorks Corporation, Waltham, MA, USA) to ensure a seamless incorporation of the new geometry. This was accomplished by turning the vertebrae into into interactive part files compatible with SolidWorks (SOLIDWORKS® 2023, Dassault Systèmes-SolidWorks Corporation, Waltham, MA, USA).

3.2.1.A. Spinal Cord

The spinal cord was created in SolidWorks (SOLIDWORKS® 2023, Dassault Systèmes-SolidWorks Corporation, Waltham, MA, USA) by utilizing anatomical dimensions and measurements from the literature (Holsheimer et al., 1994; Kameyama et al., 1996; Ko et al., 2004; Sherman et al., 1990). Planes that intersected the center of each vertebra were created to ensure that the cross section at each level of the spinal cord was synonymous with the curvature of the vertebrae. Additional planes were created as start and end points for each vertebral segment (Figure 30). Spinal cord segment length dimensions were based on values from the literature (Ko et al., 2004) with slight adjustments so that the superior and inferior defining plane for each segment lay in-between the corresponding IVF to ensure a smooth face for the intersection of the nerve roots.

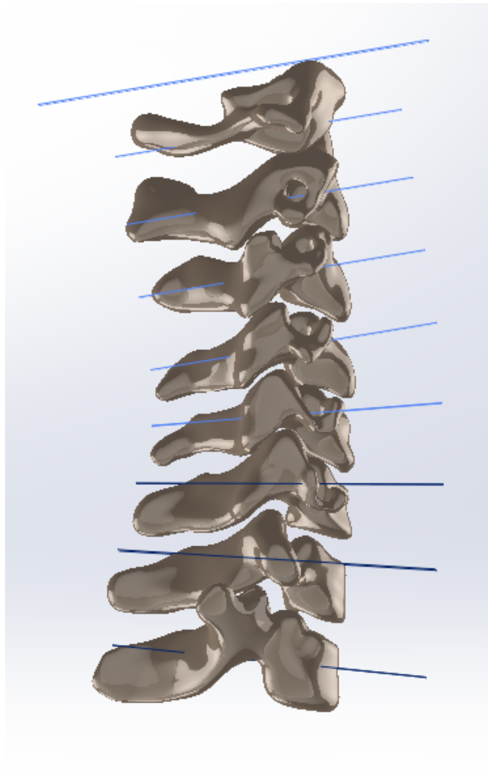

Figure 30: Intersecting Vertebral Planes for the Establishment of the Distinctive Spinal Cord Segments.

The outline of the white and gray matter was based off histological projections (Kameyama et al., 1996) showing the appearance of the spinal cord at each spinal level (Figure 31). A picture of the cross sections at each level was imported into SolidWorks (SOLIDWORKS® 2023, Dassault Systèmes-SolidWorks Corporation, Waltham, MA, USA) using the sketch picture tool, and the spline tool was used to trace the curvature of the white and the gray matter. The cross-section sketch was then transferred to the starting plane for the corresponding spinal level in the spinal canal (Figure 32-A). However, the spinal cord does not sit directly in the geometric center of the spinal canal, but instead sits offset, typically farther towards the anterior wall of the spinal canal, referred to as eccentricity. Eccentricity values were taken from the literature (Fradet et al., 2014) and used to place the spinal cord sketch at the appropriate anterior-posterior location at each level of the spinal cord. Zero left-right eccentricity was assumed due to the low values in the literature, meaning the spinal cord was placed directly in the center of the sagittal plane. The spinal cord cross section sketches were then connected using the boundary surface connect tool and solid surfaces were created using the knit surface tool, resulting in a continuous spinal cord that was split into sixteen distinct parts, consisting of the gray and white matter at each spinal level (Figure 32-B,C).

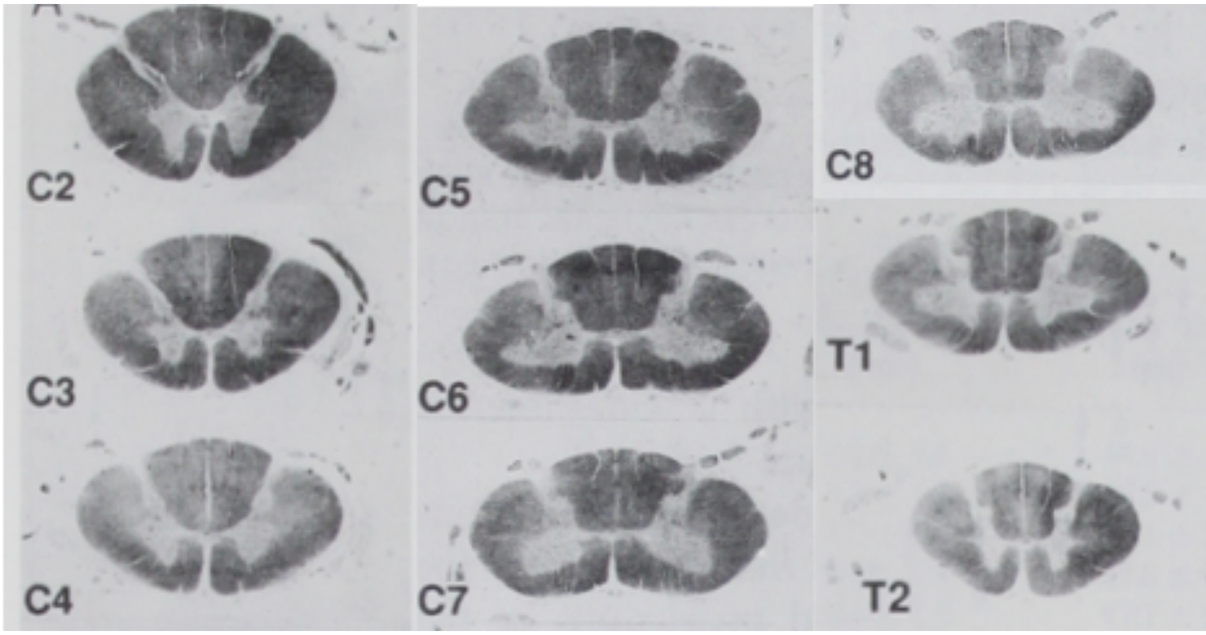

Figure 31: Cross-sectional Morphological Characteristics of the Gray and White Matter at Different Levels of the Cervical Spine.

Source: (Kameyama et al., 1996).

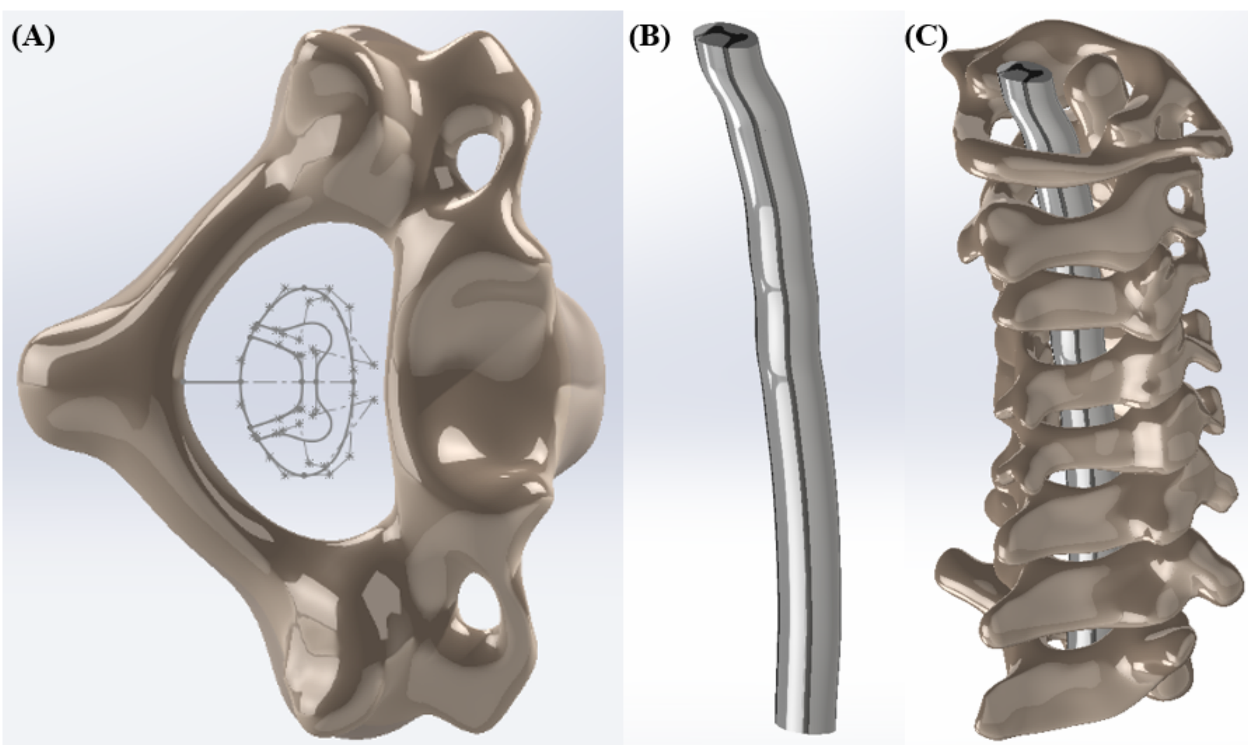

Figure 32: Construction and Finished Geometry of the Spinal Cord.

(A) an example of one of the spinal cord sketch traces used in its construction, (B) the fully constructed white and gray matter, (C) the finished spinal cord within the vertebrae.

Once the spinal cord was complete, the CSF was created by sketching half of the general shape of the arachnoid space enclosed by the dura mater and placing it 1.5-4.0mm from the spinal cord (Holsheimer et al., 1994) at each level, ensuring that it did not encounter the vertebral walls (Figure 33-A). The sketches at each level were again connected in the same manner as with the spinal cord and then mirrored to create a solid layer of CSF at each level (Figure 33-B,C).

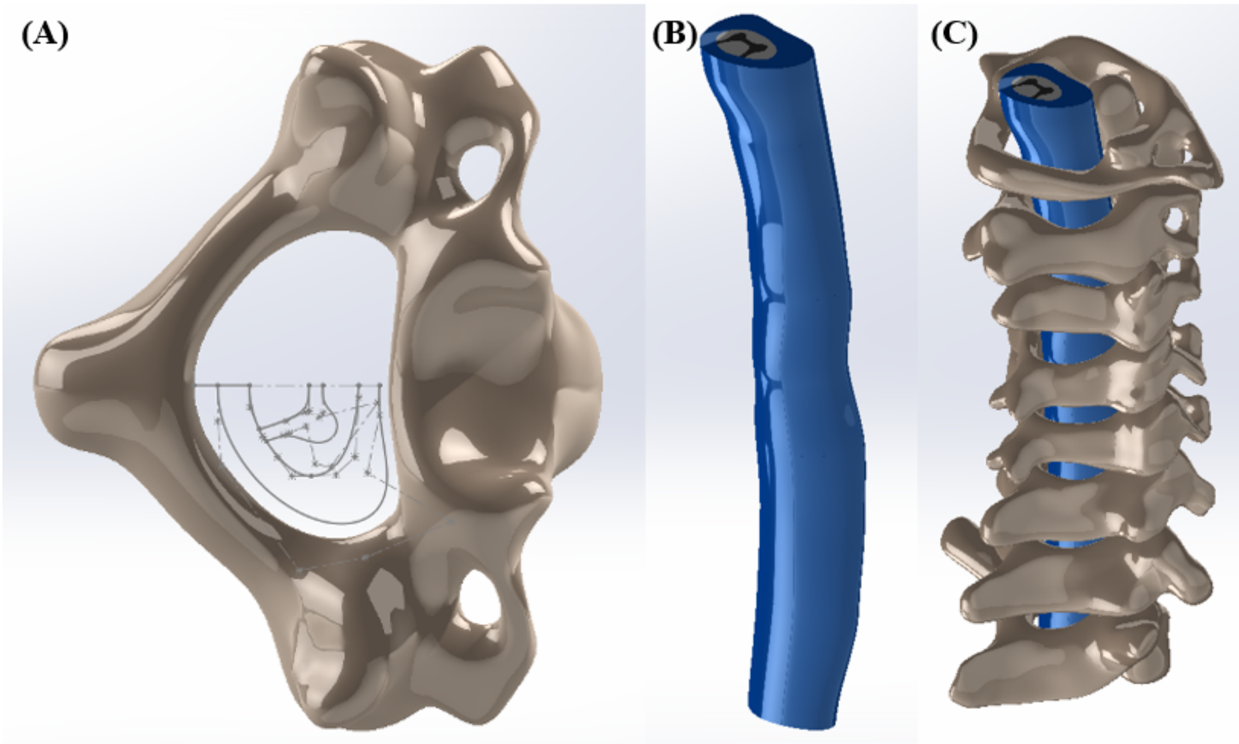

Figure 33: Construction and Finished Geometry of the CSF.
(A) an example of one of the CSF sketch traces used in its construction, (B) the fully constructed CSF enclosing the white and gray matter, (C) the finished CSF enclosing the spinal cord within the vertebrae.

3.2.1.B. Nerve Roots and Spinal Nerves

The nerve root geometry was modelled as the shape that the root sheath encloses around the dorsal and ventral root. This was because attempts to create a separate dorsal and ventral root proved extremely difficult when converting the geometry into a FE mesh. The area of narrowness that existed in the root sheath between the dorsal and ventral root required extremely small elements to capture the curvature, on the order of 0.1 and 0.2 mm, exponentially increasing the total element count to an unreasonable amount. Thus, a simplified nerve root component was created that included the area of swelling that encompasses the DRG. To accomplish this, three separate circular cross sections with varying dimensions based on values in the literature (Alleyne et al., 1998) were mounted on a common trajectory through the IVF at a precise angle and location in the 3D space to ensure that there would be no contact between the DRG and the vertebral wall (Figure 34-A). Next, the cross sections were connected using the boundary boss-base tool with tangency enforced between each segment. The proximal end of the nerve root extended into the solid CSF portion initially; however, the subtract function was utilized to delete the portion of the proximal nerve root within the CSF, leaving just the lateral nerve root and a seamless interface between the two (Figure 34-B). The DRG was positioned and sized with the middle circular cross section and placed directly superior to the centers of the medial zone of the pedicle, classifying them as proximally situated DRGs according to the classification laid out by (Yabuki & Kikuchi, 1996). The spinal nerve was created by extending the proximal end of the nerve root/DRG complex along the same trajectory by 15 mm as its own separate part. This process was repeated and mirrored to the left side for each level of the spinal cord C2-8.

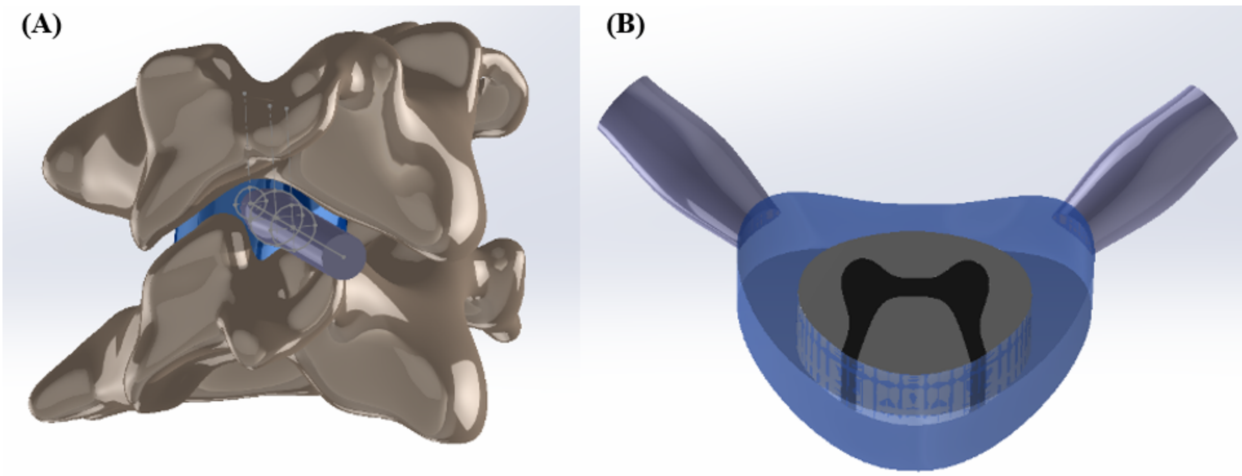

Figure 34: Construction and Final Geometry of the Nerve Root/DRG Complex.
(A) an example of the construction lines used to form the nerve root/DRG complex within the C3/4 IVF, (B) C4 cross section of the interface between the nerve root, CSF, and spinal cord.

At the C1 level, the nerve root was created by using only one smaller circular cross section and extruding it along an appropriate trajectory exiting the spine. This is because studies report the absence of both the ventral root and the DRG at the C1 level, with one study by (Tubbs et al., 2007) only observing the existence of the DRG in 28.5% of specimens and a smaller C1 root compared to the rest of the nerve roots. Thus, it felt appropriate to exclude the DRG at the C1 level (Figure 35-B,C). The finalized SolidWorks (SOLIDWORKS® 2023, Dassault Systèmes-SolidWorks Corporation, Waltham, MA, USA) geometry of the gray and white matter, CSF, nerve root complex and spinal nerve is shown below in Figure 35-A.

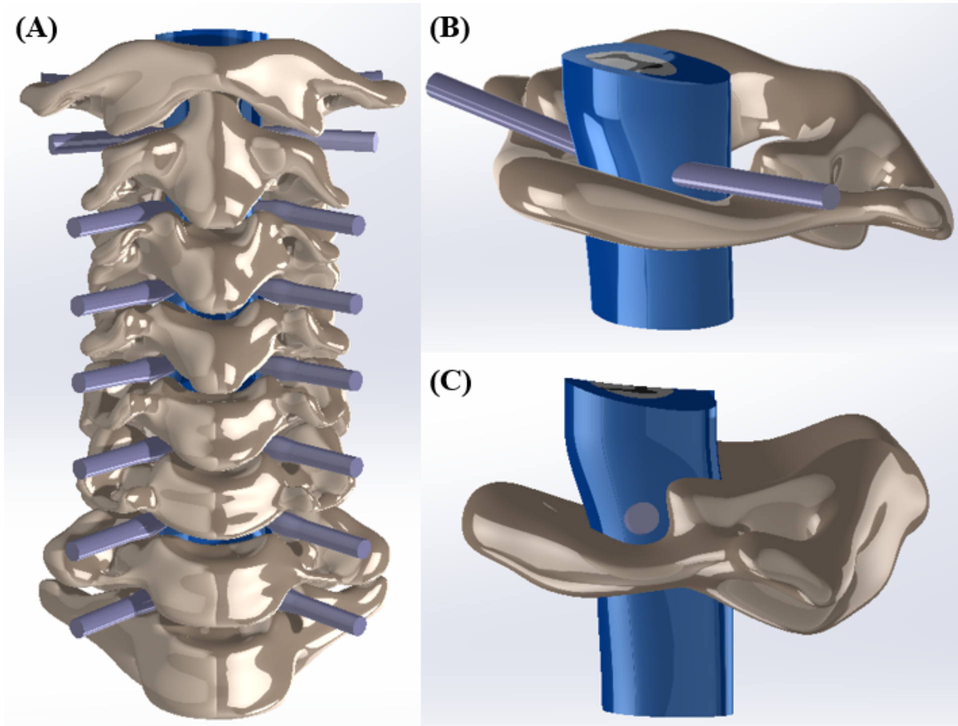

Figure 35: Finalized Geometry of the Cervical Gray and White Matter, CSF, Nerve Root/DRG Complexes, and Spinal Nerves.

(A) anterior view of new soft tissues within the vertebrae, (B) isometric view of the C1 nerve root, (C) right lateral view of the C1 nerve root.

3.2.1.C. Meninges

Once the SolidWorks (SOLIDWORKS® 2023, Dassault Systèmes-SolidWorks Corporation, Waltham, MA, USA) parts were created, their meshes were generated and the files were imported into the existing VIVA Open HBM model. The dura mater and the root sheath were created as shells on the outside surface of the CSF and the nerve root complex at each spinal level, adding 16 more parts into the model (Figure 36). The shells were defined with a thickness of 0.5 mm as reported in the literature (Holsheimer et al., 1994).

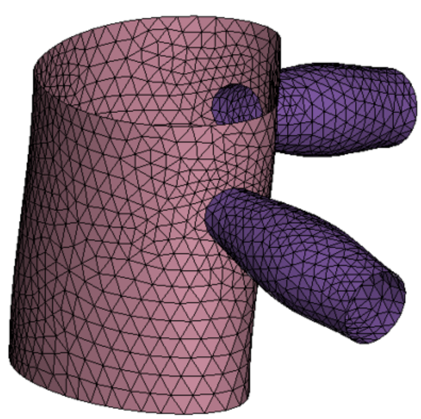

Figure 36: An Example of the Dura Mater and Root Sheath Surfaces within LS-PrePost at the C3 Level.

The pink sheath is the dura mater that is defined by the CSF surface nodes, while the purple sheath is the root sheath defined by the nerve root/DRG complex surface nodes.

3.2.1.D. Nerve Rootlets and Denticulate Ligaments

To implement the nerve rootlets and denticulate ligaments into the VIVA OpenHBM model, the methods utilized by (Khuyagbaatar et al., 2018) were replicated. According to the microanatomical study done by (Alleyne et al., 1998), the average number of dorsal rootlets ranged from 6-8 between C3-T1, thus, seven dorsal and ventral nerve root discrete elements were implemented into the model in LS-PrePost (LS-PrePost 4.10, © 2024 DYNAmore GmbH, an Ansys Company, Hauptniederlassung Stuttgart) originating on the white matter and inserting on the proximal face of the nerve root/DRG complex. In the study done by (Alleyne et al., 1998), the superior and inferior angle that the nerve rootlets made with the spinal cord was recorded (Figure 37). Thus, care was taken to choose origin and insertion sites for the most superior and inferior nerve rootlets to closely match the values for the superior and inferior angle cited in the literature. This process was repeated at levels C2-C8 (Figure 38-A,C); however, the nerve rootlets at the C1 level differed in number. In the study done by (Tubbs et al., 2007), in 46.6% of specimens the C1 nerve root received contributions from a mean of two dorsal rootlets, with the rest of the specimens not receiving any dorsal rootlets at the C1 level. Thus, two dorsal and ventral rootlets were created and attached to the C1 nerve root (Figure 38-B).

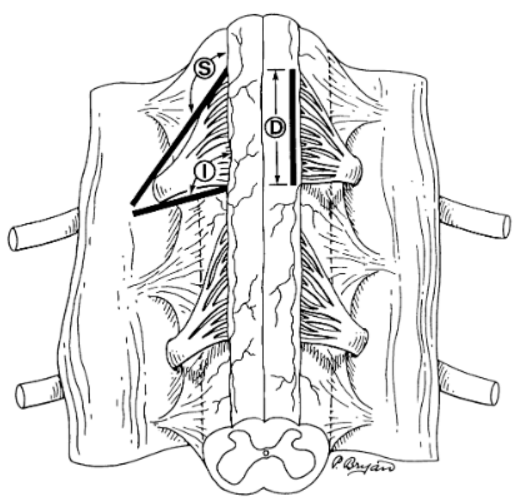

Figure 37: Cranial Superior and Inferior Angles of the Nerve Rootlet and White Matter Interface.
S is the superior angle, I is the inferior angle, and D is the length of the nerve rootlet origin. *Source:(Alleyne et al., 1998).*

To implement the DLs into the VIVA OpenHBM model, the same methods used by (Khuyagbaatar et al., 2018) were utilized. Because the DLs are described as triangular, with the wide base anchored to the white matter and the apex connected to the interior surface of the dura mater, six discrete elements were implemented that originated superior-inferiorly across the white matter and inserted at the same node on the dura mater. The orientation of the discrete elements was medial to lateral within the CSF, and they were located superior to and in between the dorsal and ventral nerve roots (Figure 38-A-C). Care was taken to ensure that the discrete elements were as evenly spread as possible and that their orientation and position matched those of KB and descriptions in the literature across the entirety of the spinal levels.

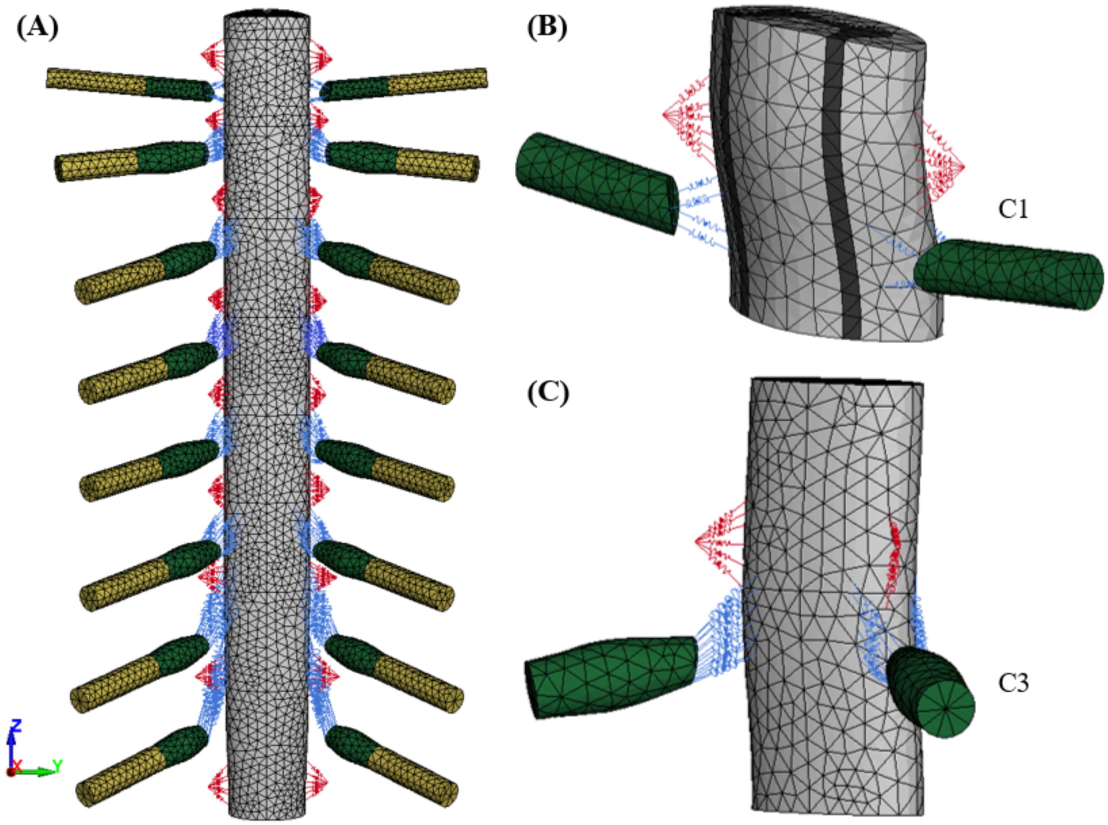

Figure 38:Implementation of the Nerve Rootlets and Denticulate Ligaments into the Nerve CSM.
(A) comprehensive gray and white matter connected to the nerve root/DRG complex (green) and spinal nerve (yellow) via the nerve rootlets (blue). The DLs (red) were connected to the white matter and the dura mater. (B) nerve rootlets and DLs at C1, (C) an example of the nerve rootlets and DLs at C3.

3.2.1.E. Foraminal Ligaments

To the author's knowledge, the incorporation of foraminal ligaments into a FE model has not been done previously. Thus, care was taken to accurately represent both the IFLs and EFLs within the IVF according to anatomical descriptions by (Yang et al., 2019) and (Shi et al., 2015). Four medial zone IFLs were incorporated within each IVF C3-T1, with origins at the posterior facet joint capsule, the upper edge of the inferior pedicle, the lower edge of the superior pedicle and the posterior part of the vertebrae directly adjacent to the IVD (Figure 39-A) (Yang et al., 2019). Orientations of the medial zone intraforaminal ligaments were radial, and care was taken to choose nodes that would ensure they met the nerve root/DRG complex as close to a right angle as possible. Due to their complex interwoven nature, the middle zone intraforaminal ligaments were not included in this study, as it was unclear how they could be accurately represented with FE elements without a more detailed description in the literature (Yang et al., 2019).

EFLs were also incorporated into each IVF. However, only radiating EFLs were included in this study; no TFLs were incorporated. This was due to the wide variety of incidences between individuals, as some specimens in the study by (Shi et al., 2015) had them in every IVF, while others had none at all. The inclusion of the TFLs would have significantly contributed to the complexity of this study, as the TFL has attachments not only to the vertebrae, but also to the nerve root/DRG complex and would have required the creation of geometrically complex shell elements. Five radiating EFLs with medial to lateral orientations were attached with the same origins and insertions across C3-T1, with one superior, two inferior, one anterior and one posterior origin sites (Figure 39-B). The superior radiating EFL originated on the lateral margin of the cranial transverse process, while the inferior radiating EFLs originated on the anterior and posterior tubercles of the caudal transverse process (Shi et al., 2015). The anterior radiating EFL originated on the capsule of the lateral part of the uncovertebral joint, while the posterior radiating EFL originated on the capsule of the facet joint (Shi et al., 2015). The IFLs and EFLs together are shown in Figure 40 for the C4 nerve root and spinal nerve.

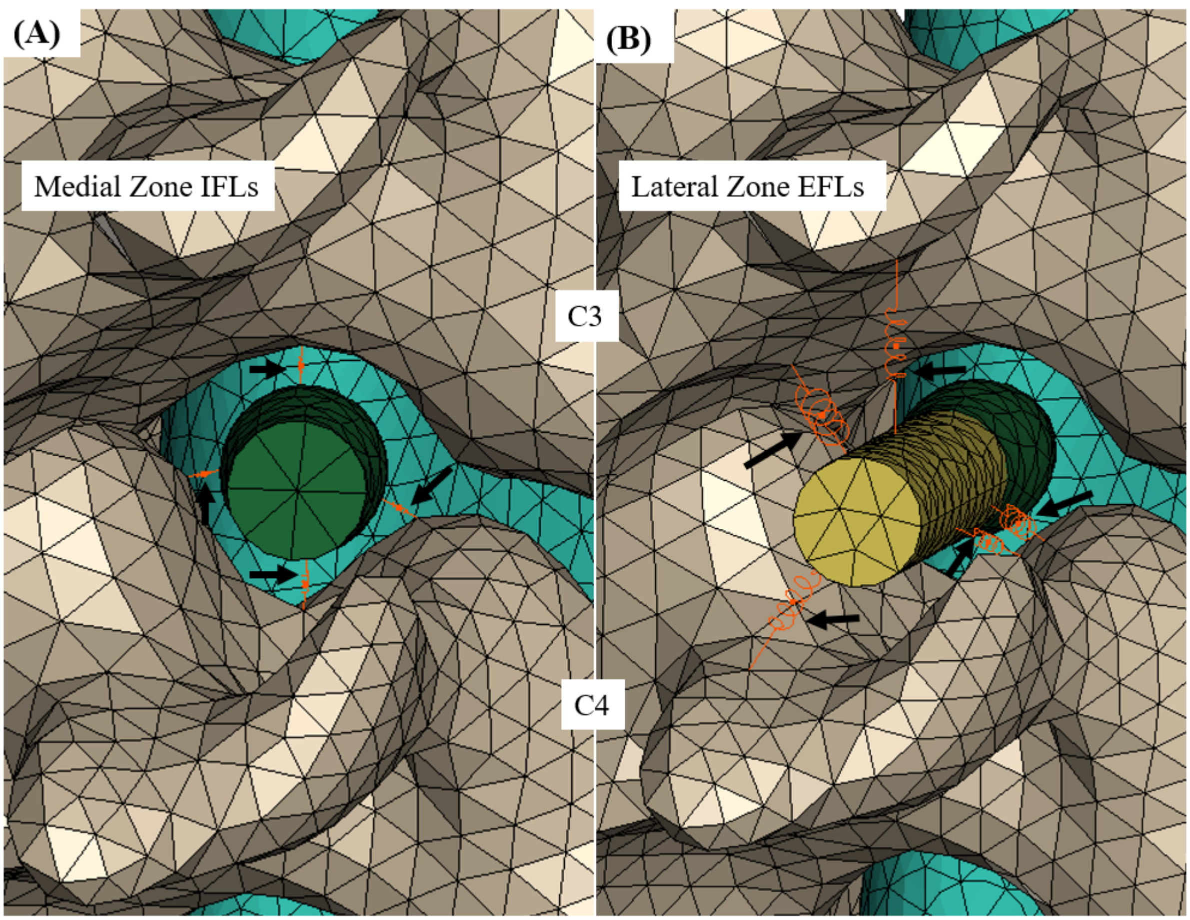

Figure 39: Medial and Lateral Zone IFL and EFL Attachment Sites.
(A) the four attachment sites of the IFLs, (B) the five attachment sites of the EFLs. IFLs/EFLs represented by orange springs and pointed out by the black arrows.

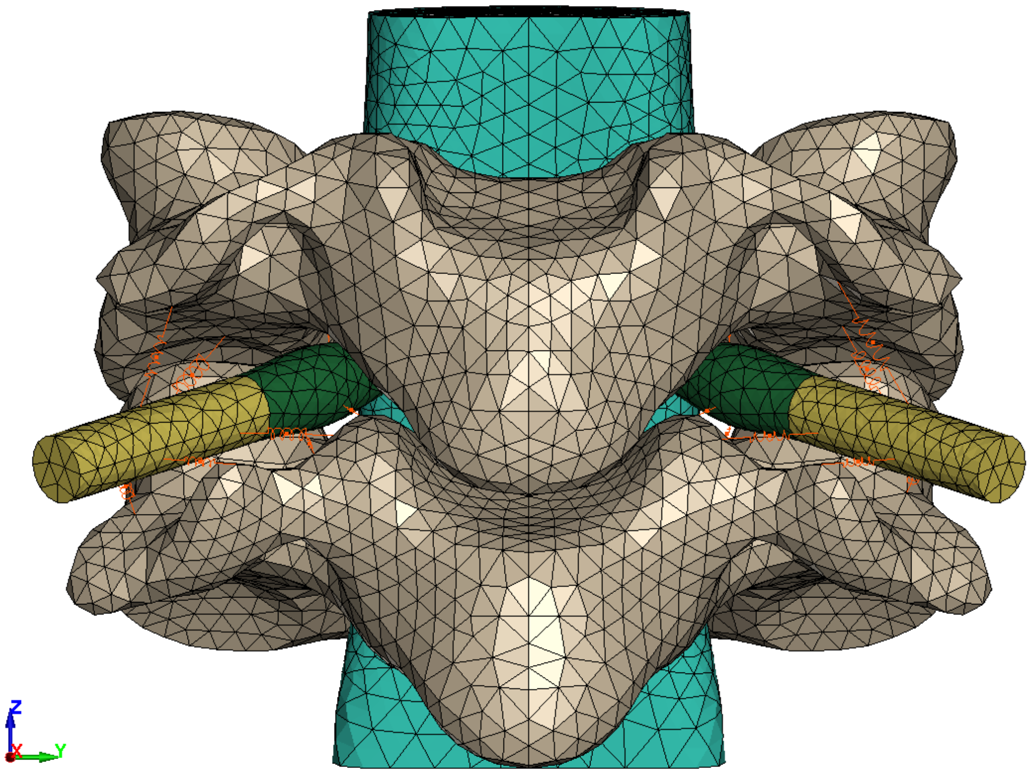

Figure 40: Overview of the IFL and EFL Attachments.
IFLs and EFLs are represented by orange springs. This example is at the C3/C4 IVF.

The IFLs and EFLs at the C1 and C2 level differed from levels C3-T1. The IFLs at the C1/2 level were described by (Yang et al., 2019) as fewer, looser, and thinner than at the lower spinal levels, with an average of one to two at the C1/C2 IVF. Additionally, only one to two radiating EFLs were reported by (Shi et al., 2015) at the C1/C2 level as well. Specific origin sites were not clarified in the literature, so origins were chosen at the author's discretion. Two IFLs and ELFs each were incorporated above the atlas to secure the C1 nerve root, with origins at the posterior lateral and medial parts of the superior articular surface of the lateral mass and the medial and lateral edges of the posterior arch (Figure 41-A). Three IFLs and EFLs each were incorporated within the C1/C2 IVF securing the C2 nerve root, with origins on the inferior C1 pedicle, the inferior posterior edge of the C1 transverse foramen, the posterior medial and lateral parts of the C2 superior articular facet, and the superior medial edge and lateral exit zone of the C2 pedicle (Figure 41-B). Figure 41-C shows an overview of the foraminal ligaments at the C1 and C2 levels.

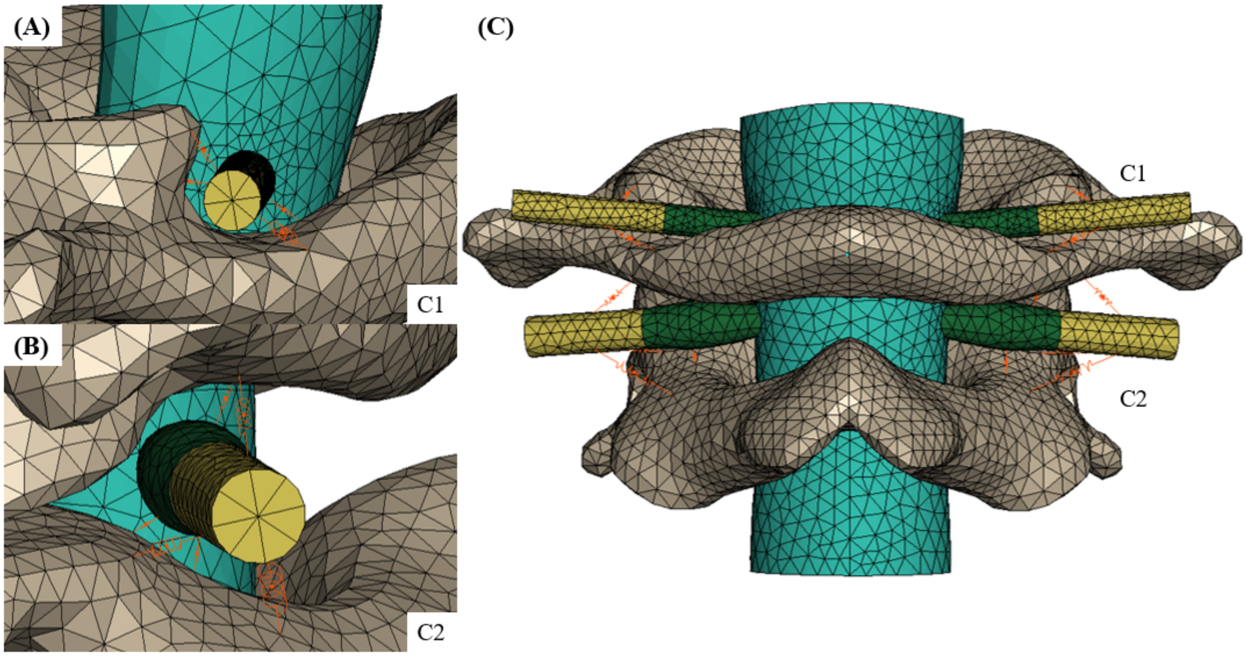

Figure 41: Overview of the Foraminal Ligaments at the C1 and C2 Level.
(A) Left lateral view of the C1 foraminal ligament attachments, (B) left lateral view of the C2 foraminal ligament attachments, (C) posterior view of the C1 and C2 foraminal ligament attachments.

3.2.1.F. Epidural Ligaments

The epidural ligaments that anchor the anterior dura mater to the PLL have been discovered in primarily lumbar and thoracic levels of the spine up to C7 but have not been observed at any of the higher cervical levels (Wadhwani et al., 2004). However, the anterior dural sac has been found to closely adhere to the PLL at higher cervical levels (Tardieu et al., 2016). To represent the constraint between the anterior dural sac and the PLL, four evenly distributed anterior epidural ligaments were attached to each PLL segment at the C2-C8 spinal level. Care was taken to ensure that the orientation of these ligament elements was as close to anteroposterior as possible with no orientation in any other direction (Figure 42).

The epidural ligaments that anchor the posterior dura to the LF and anterior laminar wall were created to replicate a photo (Figure 1) from the publication by (Shi et al., 2014) showing their orientation and distribution. From the posterior dural sac to the LF/laminae, the epidural ligament at C3 was oriented caudocranially and anchored to the C2/C3 LF. The next ligament was anchored to the C4 dural sac and inserted on the C3 anterior laminal wall, oriented caudocranially. The last two epidural ligaments were attached to the C4 and C5 dural sac and inserted on the C4/C5 and C5/C6 LF, respectively, and were oriented craniocaudally. One more epidural ligament was implemented at the C1 level, as one study by (Scali et al., 2015) demonstrated the existence of a ligamentous attachment between the atlas and the posterior dural sac. A summary of the epidural ligaments is shown below in Figure 42.

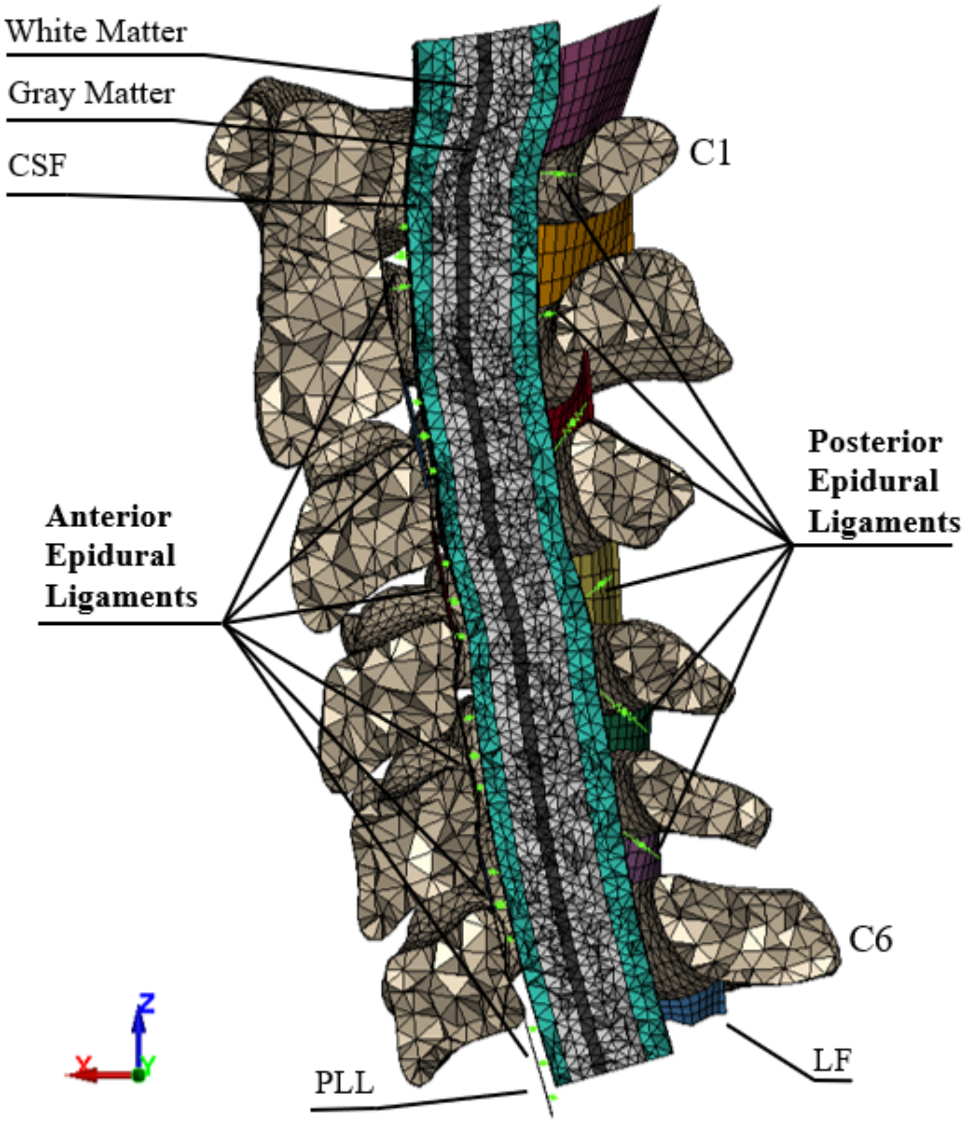

Figure 42: Overview of the Anterior and Posterior Epidural Ligament Attachments.
Shown in the center of the spinal canal is the white matter, gray matter, and surrounding CSF. The dura mater lies on the surface nodes of the CSF as a shell, where the anterior epidural ligaments (left) and posterior epidural ligaments (right) originate (green springs). These ligaments insert on the already defined PLL (posterior longitudinal ligament), LF (ligamentum flavum) and laminae of the vertebrae that was defined in the VIVA OpenHBM.

3.2.1.G. Summary of Newly Added Geometry to the Nerve VIVA CSM

To the author's knowledge, this thesis is the first research study to incorporate the DRG, intraforaminal ligaments, extraforaminal ligaments, anterior and posterior epidural ligaments, and the distinction between the nerve root and spinal nerve, thus furthering the modelling of soft tissues within the spinal canal and IVF. In total, eighty-nine new parts were added to the VIVA OpenHBM to make up the new Nerve CSM. Figure 43 shows a cross section at C4 of the newly incorporated soft tissues within the spinal canal, while Figure 44 shows the full spine with the inclusion of the vertebral ligaments and joints defined by (Östh et al., 2017).

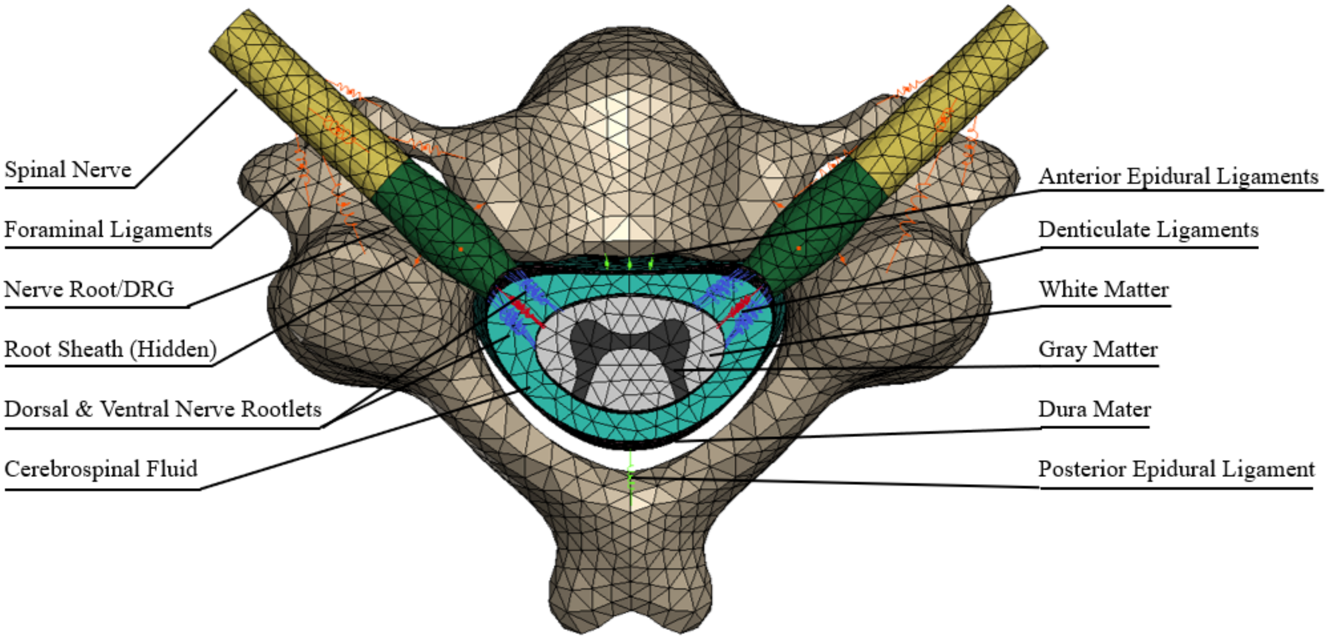

Figure 43: Cross-Sectional View of the Nerve CSM Spinal Column at C4.
Underlined parts are the new soft tissues that were defined in the Nerve CSM.

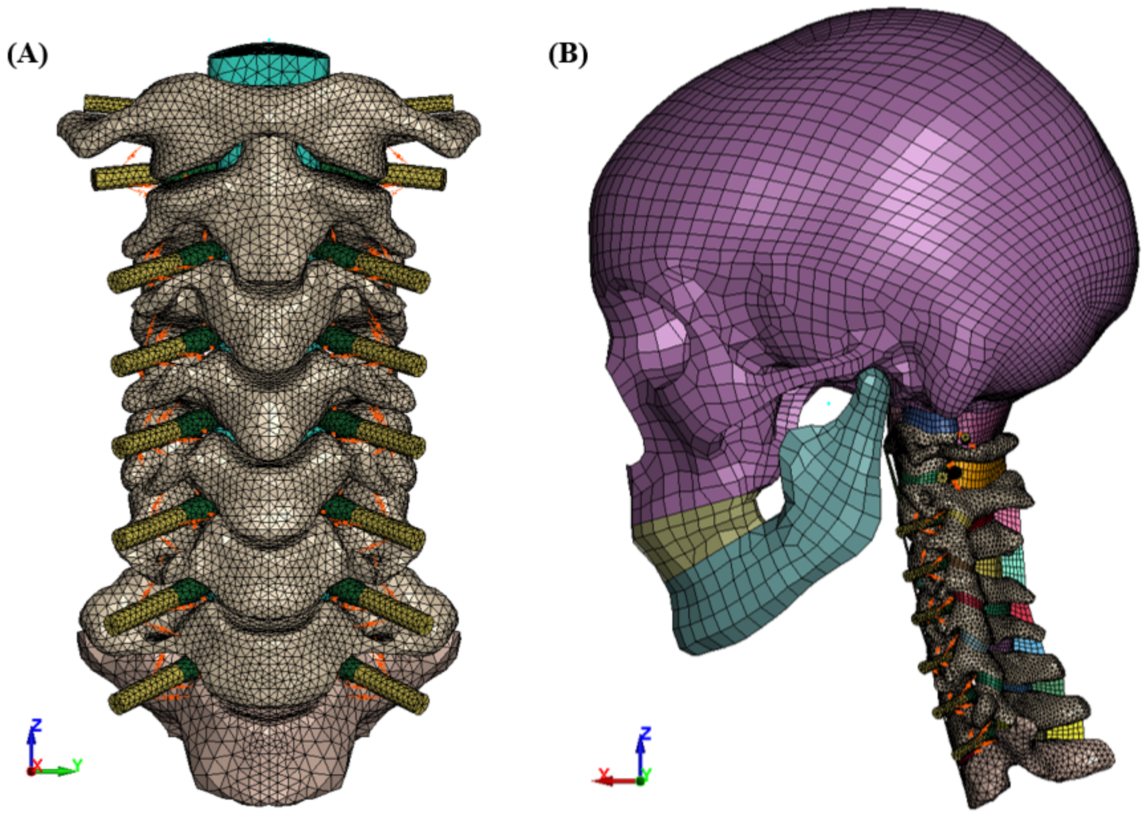

Figure 44: Full Nerve CSM Integrated FEM.
(A) anterior view of the Nerve CSM geometry within the vertebrae, (B) left lateral view of the fully integrated Nerve CSM, with some parts visible from the original VIVA OpenHBM.

3.2.2 Modeling Parameters

3.2.2.A. FE Mesh

The accuracy and reliability of finite element models is highly dependent on both the size and quality of the elements. The coarser the elements, the less computationally expensive they are, which can decrease the simulation time. However, this could be at the expense of the accuracy of the solution. Decreasing the element size, especially in areas of interest, will improve the accuracy of the solution, but will increase the computation time. As the fineness of the mesh is increased, a point is reached where the accuracy of the solution will converge and not change even when the mesh is refined further. A mesh quality assessment involves finding the largest possible elements that fall within the range of parameters that define mesh quality (Table 4). According to (Burkhart et al., 2013), a mesh quality assessment is critical in establishing elements that will be optimized for accuracy and computational efficiency. Typically, when meshing biological components with a high degree of curvature, hexahedral or tetrahedral elements are utilized. While hexahedral elements are generally considered more accurate than tetrahedral elements, the specific geometry used in this study made it impossible to implement a hexahedral mesh that met all the necessary quality criteria. This was due to the non-sweepable nature of many of the components, the high amounts of curvature, and areas of thinness. Thus, this study utilized tetrahedral elements for the soft tissues created in SolidWorks (SOLIDWORKS® 2023, Dassault Systèmes-SolidWorks Corporation, Waltham, MA, USA).

Burkhart et al. (Burkhart et al., 2013) outlines three parameters based on the shape of the mesh to check when ensuring the quality of the elements in a mesh, which are aspect ratio, angle idealization, and the Jacobian ratio. For tetrahedral elements, the most ideal shape is an equilateral 3D triangle with 60º corner angles. The aspect ratio is calculated by dividing the longest edge length divided by the smallest height of the smallest side (Figure 45). Thus, the more skewed an element, the more the sides deviate from equilateral. The optimum aspect ratio to achieve accurate solutions is close to unity (~1); however, with highly curved geometry and thin areas it is often impossible to avoid skewed elements (Burkhart et al., 2013). Aspect ratios between one and three are acceptable, between three and ten should be treated cautiously, and greater than ten should be viewed with alarm. Not only should the magnitude of the aspect ratio be considered, but additionally the location and frequency of elements that occur above three should be reported. The recommendation that this thesis will follow is to keep the percentage of element aspect ratios that exceed three to be less than 5% of the total elements (Burkhart et al., 2013) (Table 4).

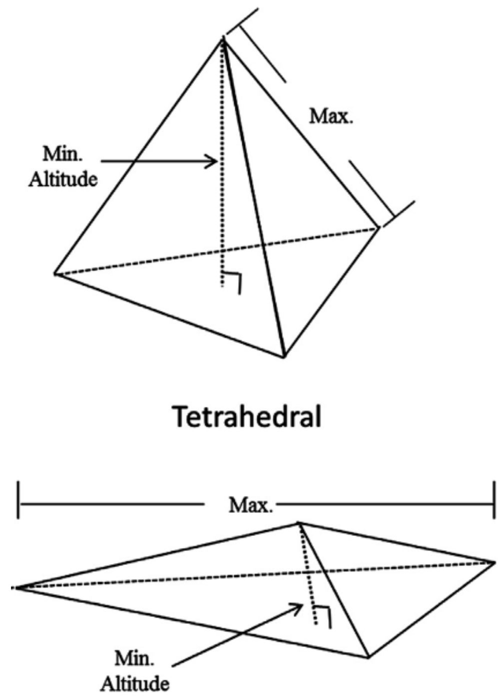

Figure 45: Calculation of a Tetrahedral Aspect Ratio.
An element with an aspect ratio of approximately one (top) is compared to an element with an aspect ratio of 14 (bottom).
Source:(Burkhart et al., 2013).

Secondly, angle idealization should be considered when a realistic deformation of the mesh is desired. Elements with extremely large or small corner angles are highly skewed and should be treated with caution. An example of element corner angles is shown below (Figure 46). (Burkhart et al., 2013) recommends that less than 5% of the total number of elements should fall outside the range of 30-150º, as tetrahedral elements within this range have been shown to be relatively accurate (Klingner & Shewchuk, 2007).

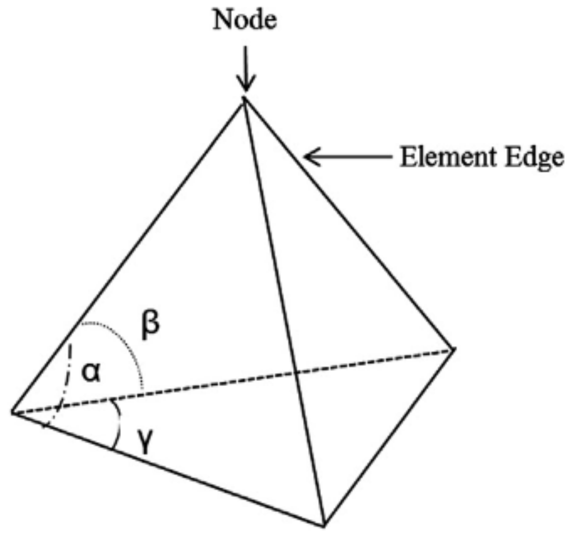

Figure 46: Example of Three Element Angles Calculated at the Corners of the Element.
α, β, and γ refer to the angles formed by the 2D planes that intersect that corner of the triangle. *Source:(Burkhart et al., 2013).*

Lastly, the element Jacobian describes a measure of volume distortion from the idealized shape, and is the determinant of the Jacobian matrix, which contains descriptions of the shape, orientation, and volume of the element. Further, it maps the vertices of an element from the ideal shape to the actual shape and will result in a negative value for an inverted, extremely distorted element. Any negative Jacobian value for an element will stop a finite element calculation from continuing. Thus, all element Jacobian values must be positive (Knupp, 2000), preferable greater than 0.2 (Quenneville & Dunning, 2011; Untaroiu et al., 2005), and less than 5% should fall below a value of 0.7 (Ray et al., 2008). A mesh quality assessment of the Nerve CSM was performed to ensure that all the elements within its mesh fell within these guidelines.

Table 4: Summary of Mesh Quality Recommendations for Tetrahedral Elements

Criteria	Acceptable range	No. of elements allowed outside range	Unacceptable value or range
Aspect Ratio	1-3	Less than 5%	~
Corner Angles	30º-150º	Less than 5%	~
Element Jacobians	0.7-10	Less than 5%	None below 0.2

3.2.2.B Definition of Section Properties and Constitutive Models for the Nerve CSM

The material and element parameters utilized in the Nerve CSM iterations are summarized below in Table 6. The CSF surrounds the spinal cord and plays an important role in absorbing dynamic energy during an impact (Baeck et al., 2011), protecting the spinal cord from injury. Additionally, the hydrostatic pressure that the CSF provides to the surrounding tissues plays a vital role in providing stability to the spinal cord and dura mater, preventing them from folding in on each other. Representing the CSF biomechanically in an FE model is one of the greatest challenges to developing a model of the spinal canal. For the purposes and scope of this thesis, we were not focused on modelling the fluid flow or sloshing within the subarachnoid space, but instead capturing the hydrostatic pressure that the CSF contributes to the biomechanics of the spinal column. One approach to modeling the behavior of the CSF is to define it as a linear elastic material with a high bulk modulus and a low shear modulus (Baeck et al., 2011), which was implemented in this model. The CSF was modelled as the solid volume between the gray and white matter and the dura mater with quadratic tetrahedral elements. The linear elastic material model defined by (Baeck et al., 2011) was implemented for the CSF.

The gray and white matter were modelled as solid, using quadratic tetrahedral elements. A hyperelastic Ogden constitutive model that was defined by (Ichihara et al., 2001) using bovine gray and white matter was utilized for the spinal cord in this study. This material model has been validated on multiple occasions in various cervical spine models (Khuyagbaatar et al., 2014, 2015; Y. H. Kim et al., 2013; Xue et al., 2021), making it a reliable choice to incorporate for the gray and white matter.

The spinal nerves were represented with solid, quadratic tetrahedral elements. A linear elastic constitutive model that was defined by (Kerns et al., 2019) using human peroneal nerves was utilized for the spinal nerve. The study done by (Luttges et al., 1986) stated that the density of nerve material was 1.5 times higher than the nerve root density, corroborated by the study done by (Beel et al., 1986) which stated that spinal nerves had a density 1.4 times higher than the nerve roots. Nerve root density was reported as 1040 kg/m3 in the publication by (Beel et al., 1986), thus the value the Nerve CSM utilized for the spinal nerve density was 1.45 times higher, rounded to 1500 kg/m3. To the author's knowledge, this model is the first to define a distinct material for the spinal nerve from the nerve root.

The extradural nerve root/DRG complexes were modelled as solid, quadratic tetrahedral elements. Beel et al. (Beel et al., 1986) reported the average density of the lumbar nerve roots to be 1040 kg/m^3, thus that is the value which was used in this model. The models by (Khuyagbaatar et al., 2017, 2018; Xue et al., 2021, 2023) used linear elastic material properties defined by (Singh et al., 2006) for the nerve roots, thus, the Nerve CSM utilized the same.

Dural tissue within the vertebral foramen was distinguished into two parts: the dura mater which interfaced with and surrounded the CSF, and the root sheath, which encased the extradural nerve root/DRG complex. The dura mater is extremely thin [~0.5mm, (Holsheimer et al., 1994)] thus, it makes sense to model it as a shell. A triangular element formulation was used to represent the dura mater and root sheath shell elements. Because the focus of the model is the nerve roots, the nodal integration points on the root sheath were increased from two to five. Because the main fiber orientation of the dura mater is longitudinal and the main direction of loading in the dura is in the longitudinal direction during flexion/extension, isotropy was assumed for the purposes of this study and properties from longitudinal testing were utilized. Additionally, because isotropy and near incompressibility was assumed, the Poisson's ratio chosen was 0.49 as done by (Khuyagbaatar et al., 2017, 2018; Xue et al., 2021, 2023). Future models that include anisotropic properties should carefully consider utilizing higher Poisson's ratios as reported in (Persson et al., 2010). Density values could not be found in the literature, thus, the same value utilized by (Khuyagbaatar et al., 2017, 2018; Xue et al., 2021, 2023) was chosen. Mechanical behavior of the dura mater and root sheath was modelled using the linear elastic properties defined by (Runza et al., 1999).

The nerve rootlets and denticulate ligaments were modelled using discrete, nonlinear tension-only springs, as done by (Khuyagbaatar et al., 2017, 2018; Xue et al., 2021, 2023). MAT_SPRING_INELASTIC (S08) was used to achieve this, and the mechanical behavior was defined by a force vs. displacement load curve from the literature (Polak et al., 2014; Singh et al., 2006). The CTF parameter within the material keycard was set to -1.0 to allow only tension within these elements.

The IFLs, EFLs and epidural ligaments were also modelled with MAT_SPRING_INELASTIC (#S08), due to their thin, tensile-only nature. However, defining a force vs displacement curve of the foraminal and epidural ligaments was elusive, as to the author's knowledge, no known studies have provided biomechanical behavior for either of these groups of connective ligaments. Thus, due to the lack of data available, the same load curve for the DLs was used for the foraminal and epidural ligament material model.

Table 5: Summary of Element and Constitutive Material Models used in the Nerve CSM.

Part	Element Type (ELFORM)	Constitutive Model (*MAT_no)	Material Parameters	Density (kg/m^3)	References

CSF	Quadratic tetrahedral (16)	Linear Elastic (003)	E = 15 MPa ν = 0.49	1000	(Baeck et al., 2011)
Gray Matter	Quadratic tetrahedral (16)	Hyperelastic Ogden (077)	μ = 4.1 kPa, α = 14.7 ν = 0.49	1050	(Ichihara et al., 2001; Khuyagbaatar et al., 2018; Xue et al., 2023)
White Matter	Quadratic tetrahedral (16)	Hyperelastic Ogden (077)	μ = 4.0 kPa, α = 12.5 ν = 0.49	1050	(Ichihara et al., 2001; Khuyagbaatar et al., 2018; Xue et al., 2023)
Spinal Nerve	Quadratic tetrahedral (16)	Linear Elastic (003)	E = 10 MPa ν = 0.3	1500	(Kerns et al., 2019)
Nerve Root/DRG	Quadratic tetrahedral (16)	Linear Elastic (003)	E = 1.3 MPa ν = 0.49	1040	(Beel et al., 1986; Singh et al., 2006)
Dura Mater	C0 triangular shell (4), NIP* = 2	Linear Elastic (003)	E = 80 MPa ν = 0.49	1000	(Runza et al., 1999)
Root Sheath	C0 triangular shell (4), NIP* = 5	Linear Elastic (003)	E = 80 Mpa ν = 0.49	1000	(Runza et al., 1999)
Nerve Rootlets	Discrete Spring	Nonlinear tension only spring (S08)	Force vs. Displacement curve CTF = -1.0	~	(Singh et al., 2006)
Denticulate Ligaments	Discrete Spring	Nonlinear tension only spring (S08)	Force vs. Displacement curve CTF = -1.0	~	(Polak et al., 2014)
Foraminal Ligaments	Discrete Spring	Nonlinear tension only spring (S08)	Force vs. Displacement curve CTF = -1.0	~	(Polak et al., 2014)
Epidural Ligaments	Discrete Spring	Nonlinear tension only spring (S08)	Force vs. Displacement curve CTF = -1.0	~	(Polak et al., 2014)

Note: NIP is the number of nodal integration points.*

3.2.2.C. Definitions of Contacts and Boundary Conditions within the Nerve CSM

The VIVA OpenHBM (Östh et al., 2017) defined frictionless automatic contact utilizing CONTACT_AUTOMATIC_GENERAL with SOFT = 1 for most of the solid parts within the model. Thus, all the new solid and shell elements in the Nerve CSM were included in the automatic general contact defined by the VIVA OpenHBM model. The new Nerve CSM solid and shell parts were continuously connected with each other through the continuity of the mesh, meaning that the white matter, gray matter, CSF, dura mater, root sheath, nerve root, and spinal nerve were coupled together. The DLs connected the outside white matter to the dura mater, while the nerve rootlets connected the outside white matter to the proximal end of the nerve root. The anterior epidural ligaments constrained the anterior surface of the dura mater to the posterior face of the vertebral body, while the posterior epidural ligaments constrained the posterior surface of the dura to the anterior face of the lamina. The foraminal ligaments constrained the outer root sheath and the spinal nerve to the intervertebral foramen.

In previous studies done by (Khuyagbaatar et al., 2017, 2018; Xue et al., 2021, 2023), the spinal cord was fixed at the superior and inferior ends in all directions. However, the simulations that were performed in this study required movement of the head and vertebrae. Thus, the nodes on the superior end of the spinal cord, CSF, and dura mater were constrained to move with the skull, and the nodes on the inferior end of the spinal cord, CSF, and dura mater were constrained to move with T1. The free end of the spinal nerve was difficult to characterize, as in the body the nerve extends throughout the rest of the body and innervates various tissues. It has been observed that the cervical spinal nerves can move in the ventral/dorsal direction (Kraan et al., 2010) and stretch longitudinally. Thus, for the purposes of this study the free end of the spinal nerve was constrained to the corresponding inferior vertebrae, as done by (Xue et al., 2021, 2023).

3.3 Aim 2: Global Kinematic Validation of the Nerve CSM

To ensure that the newly added nervous tissue in the Nerve CSM did not significantly alter the global kinematics of the head-neck model, the 2.3 m/s whiplash loading conditions stipulated by (Östh et al., 2017) were applied to the Nerve CSM mesh iterations. Additionally, the original VIVA OpenHBM 2.3 m/s whiplash simulation was run to ensure that the results matched those reported by (Östh et al., 2017). Global head kinematics were defined by tracking the head's center of gravity x-displacement relative to T1 and were compared to the original experimental results published by (Östh et al., 2017). The global head kinematics of the Nerve CSM were plotted alongside those of the VIVA OpenHBM and the experimental data to observe where the simulated data fell in the established data corridor published by (Östh et al., 2017). Additionally, the correlation between the datasets was calculated by using the weighted integration factor method (Hovenga et al., 2005) as done by (Östh et al., 2017).

Because the elements surrounding the junction of the nerve root and the dura mater were exceedingly small, the mass scaling originally defined in the VIVA OpenHBM was removed. Mass scaling increases the mass of tiny elements that have a small timestep, thereby increasing the timestep and drastically reducing the computational time. However, in the Nerve CSM, the high number of small elements were causing the additional mass increase to go beyond the recommended limit and terminate the computation. Because a lower computational time was not a significant priority for the Nerve CSM, the removal of the mass scaling was not detrimental.

3.4 Aim 3: Kinematic Validation of the Nerve CSM

To validate the movement of the spinal cord within the spinal canal, replication of the experimental study done by (Stoner et al., 2019) was performed, as done by (Xue et al., 2021). In the *in vivo* experiment by (Stoner et al., 2019), healthy participants with no history of spinal pathology underwent maximum flexion and extension movements. Their total flexion and extension ROM angle was measured, with the mean being 19.8 (SD 11.1) and 19.9 (SD 12.0) degrees, respectively. This angle was determined by the methods utilized by (Bartlett et al., 2012), where two lines parallel to the posterior cortex of the C2 and C7 vertebral body were drawn and the acute angle formed by their intersection was determined (Figure 47). This thesis utilized a sign convention where positive angle values correlated to the direction of flexion and negative angle values correlated to the direction of extension. MRI images of the midsagittal cervical spine were analyzed to determine the magnitude and direction of spinal cord displacement relative to the vertebrae at the various spinal levels during maximum flexion and extension of the spine. Results for anterior/posterior (A/P), superior/inferior (S/I), and right/left (R/L) relative displacement were reported.

Figure 47: Determination of the C2/C7 Vertebral Angle.
The Angle of Extension is 39.3º. *Source:(Bartlett et al., 2012).*

The recently published cervical spine model done by (Xue et al., 2021) replicated the experiment by (Stoner et al., 2019) by simulating a rotation of ±20º around the x-axis, which was the mean C2/C7 angle across the experimental participants, to simulate flexion and extension. Further details about the boundary conditions of this simulation were not reported, including the constraints of T1 and the superior face of the spinal cord, the segmental contributions of rotation for each individual vertebrae, and the origin of rotation. The A/P, S/I, and R/L relative displacement of the C3-C7 spinal cord segments in the spinal canal were compared to the in-vivo results published by (Stoner et al., 2019). Thus, to ensure that the spinal cord model in this thesis behaves in a biofidelic way during movement of the head, a similar procedure was carried out to replicate the in-vivo experiment.

To achieve ±20º of movement in the current spine model, data from the literature (S.-K. Wu et al., 2010) was considered that reported the rotation of each vertebral segmental contribution during maximum flexion/extension in-vivo. Using LS-Prepost (LS-PrePost 4.10, © 2024 DYNAmore GmbH, an Ansys Company, Hauptniederlassung Stuttgart), local coordinate systems were defined for each vertebra according to the system defined in (S.-K. Wu et al., 2007), with the x-z plane running perpendicularly through the middle of the vertebral body. Angle changes between two adjacent vertebrae were defined in (S.-K. Wu et al., 2007, 2010) as the relative angle change between two adjacent vertebral planes once full flexion or extension was reached. The transform operation was used to rotate each vertebral body according to the full ROM values defined in (S.-K. Wu et al., 2010). The origin of the corresponding vertebral local coordinate system was defined as the center of rotation for that vertebra and the vertebrae above it, as well as the skull. The rotation was applied around the z-axis of the vertebra below it. Each total C2-C7 flexion/extension angle was then measured by defining the angle between two vectors parallel to the C2 and C7 vertebral body with the methods used by (Bartlett et al., 2012)

Because Wu et al. (S.-K. Wu et al., 2010) had different participants performing maximum flexion and extension from the study done by (Stoner et al., 2019), the C2/C7 angle reached using the mean segmental angulations did not result in ±20º, as was reported for the average C2/C7 angle in maximum flexion/extension by (Stoner et al., 2019). The C2/C7 angle achieved in the Nerve CSM utilizing the mean segmental angulations from (S.-K. Wu et al., 2010) was 41.4º in flexion and -47.3º in extension. Thus, to get the C2/C7 angle as close to ±20º as possible, the lower bounds of the segmental rotations reported by (S.-K. Wu et al., 2010) were utilized, which resulted in 23.4º in flexion and -26.3º in extension (Figure 48), which is much closer to the 20º average C2/C7 and well within the standard deviations reported by (Stoner et al., 2019). Thus, it is reasonable to assert that this method to reach a maximum flexion and extension position is within the range of average human physiology and can be used to carry out a max flexion/extension movement of the cervical spine model. The lower bound segmental angulations were thus used in the flexion/extension spinal cord validation simulation to compare to the results published by (Stoner et al., 2019) and (Xue et al., 2021).

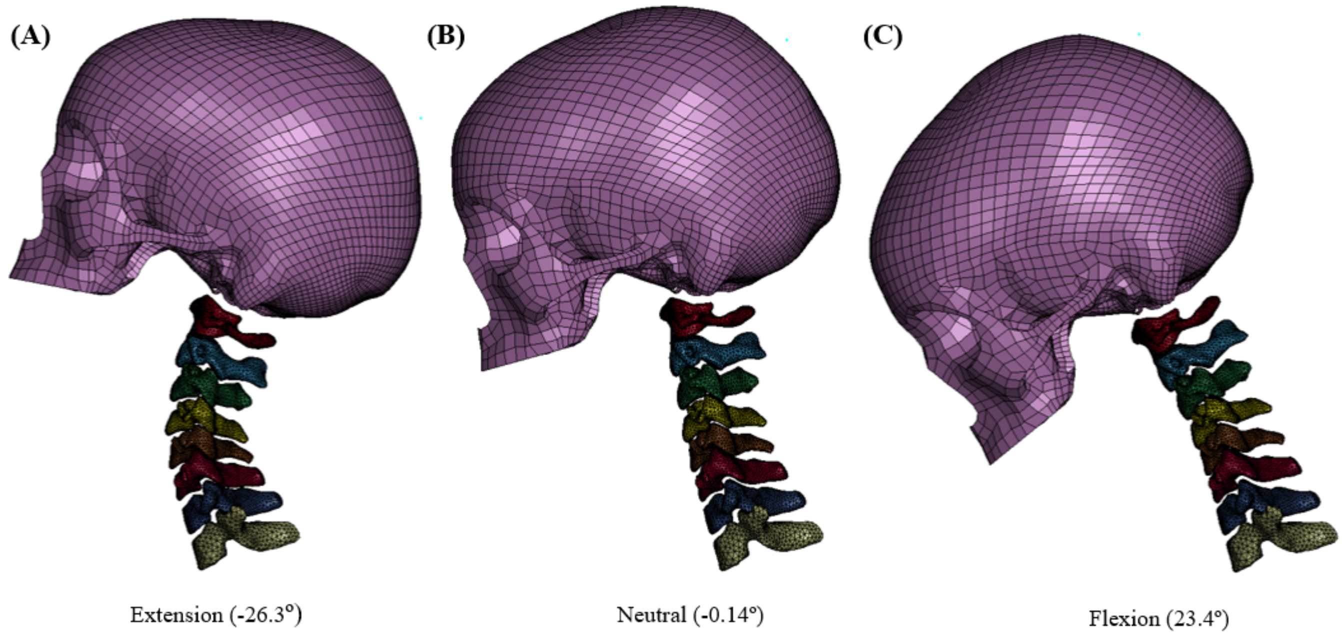

Figure 48: Final Simulated Extension and Flexion Head and Neck Positions.
(A) Final position of extension applied to the Nerve CSM, (B) neutral Nerve CSM initial position, (C) final position of flexion applied to the Nerve CSM. The values in parentheses represent the C2/C7 angle.

To apply the flexion/extension movement to the Nerve CSM, nodal coordinates from the rotated vertebrae and skull were copied into a keyword card in the neutral Nerve CSM model that prescribed final nodal positions (PRESCRIBED_FINAL_GEOMETRY). Points on the C3-C7 posterior surface of the white matter were defined at the superior-inferior midpoint of the segment to track the A/P, S/I, and R/L relative displacement. The A/P, S/I, and R/L relative displacement values were plotted alongside the values from Stoner et al. (Stoner et al., 2019) and Xue et al. (Xue et al., 2021) to see if they fell within the standard deviation defined by Stoner et al. (Stoner et al., 2019). During flexion/extension of the neck *in vivo*, there is relatively little movement of the lower lumbar and thoracic vertebral segments, thus the T1 vertebrae was constrained in all 6 DOF. While it is likely that T1 does experience some movement during flexion/extension *in-vivo*, the magnitude and direction is not defined. Additionally, T1 was the lowest vertebrae available to be constrained; thus, it was necessary to add some condition that replicated the relative immobility of the lower spine during flexion/extension.

CHAPTER 4: RESULTS

4.1 Aim 1: Results of Mesh Quality Assessment and Sensitivity Analysis

The results of the mesh quality assessment are displayed below in Table 7. The elements within the Nerve CSM fell within the standards outlined by (Burkhart et al., 2013), where less than 5% of the elements had an aspect ratio greater than three, a maximum corner angle greater than 150º, and a Jacobian ratio lower than 0.7. Additionally, none of the elements had a negative Jacobian value, with the lowest value seen at 0.19. The location of the elements that were the most skewed was the descending tracts of the gray matter, as that area encompassed the most curvature and thin walls. Because the elements within the global mesh fell within the quality standards outlined by (Burkhart et al., 2013), it was acceptable to utilize them in the Nerve CSM.

Table 6: Mesh Quality Assessment Results.

Mesh	No. of nodes	No. of elements	Max. Aspect Ratio	Aspect Ratio >3 (%)	Max. Corner Angle	Corner Angle >150 (%)	Min. Jacobian value	Jacobian < 0.7 (%)
Nerve CSM	182,271	123,486	11.20	1.72	158	0.02	0.19	2.30

The addition of the nerve components into the VIVA OpenHBM that established the formation of the new Nerve CSM did increase the computational cost, as reflected by the increased runtime, where the original VIVA OpenHBM took 2 hrs. and 25 min to run and the Nerve CSM took 24 hrs. and 23 min to run.

4.2 Aim 2: Results of Global Kinematic Validation of the Nerve CSM

In the rear impact whiplash simulation, the correlation score published by (Östh et al., 2017) of the global head kinematics for head x-displacement relative to T1 between the VIVA OpenHBM model and the Post Mortem Human Subject (PMHS) data was reported as 0.7. Due to the lack of reported significant digits, the authors of this thesis re-calculated the correlation score between the VIVA OpenHBM and PMHS datasets extracted from (Östh et al., 2017) using the weighted integration factor method (Hovenga et al., 2005), with the result coming out to 0.717. As reported by (Östh et al., 2017), the time-displacement response of the VIVA OpenHBM model fell within the scaled 50th percentile PMHS standard deviation corridors. Overall, the modified Nerve CSM developed in this thesis showed a similar response and correlation score to the VIVA OpenHBM. The correlation score determined for the Nerve CSM was 0.706, slightly lower than the result found for the VIVA OpenHBM. Additionally, the x-displacement of the head also fell within the scaled 50th percentile PMHS standard deviation corridors, with only a slight deviation past 0.09s (Figure 49).

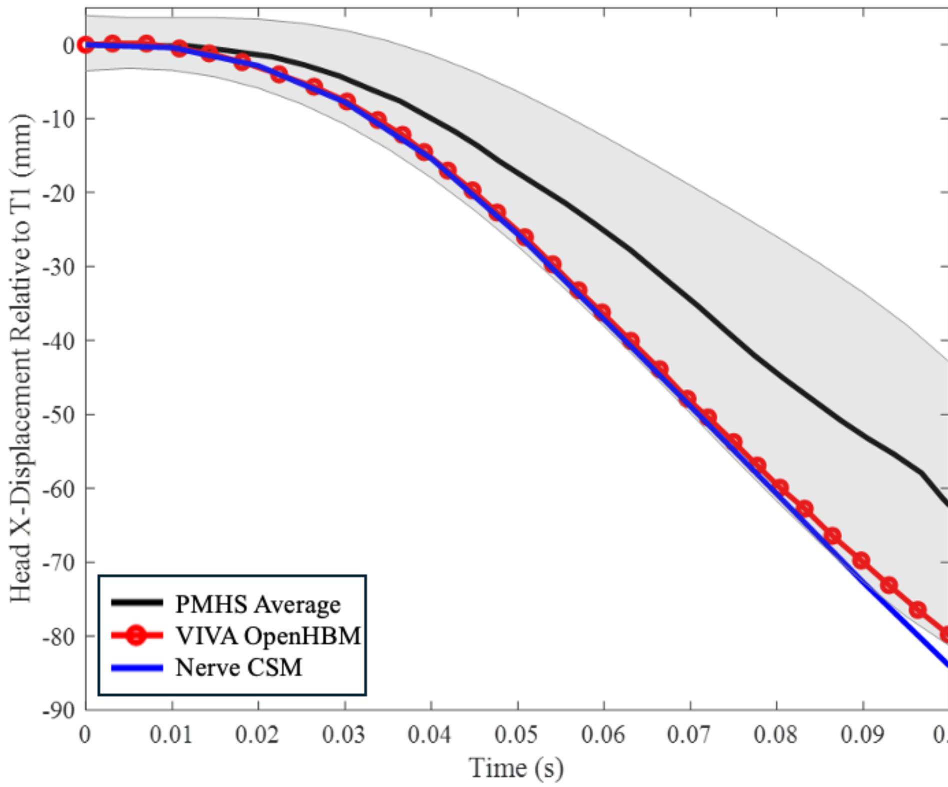

Figure 49: Head X-Displacement of the Nerve CSM Compared to PMHS and VIVA OpenHBM.
The solid black line refers to the experimental PHMS data *(Stemper et al., 2004)*, the red marked line refers to the VIVA OpenHBM response *(Östh et al., 2017)*, the blue line refers to the Nerve CSM response, and the light gray shaded areas represent the scaled female 50th percentile PMHS corridors *(Östh et al., 2017)*.

To ensure that the newly added nervous tissue in the Nerve CSM did not substantially alter the system energies of the head-neck model, the system energies of the VIVA OpenHBM and the Nerve CSM were compared. There were slight differences in the responses (Figure 50), which is to be expected, as models that are deforming slightly differently would contribute to a different sum of system energies. The Nerve CSM followed the general shape of the VIVA OpenHBM system energies, and most importantly, none of the artificial energies (hour glassing, damping) showed a noteworthy deviation, which was expected, as none of these parameters were altered from the VIVA OpenHBM.

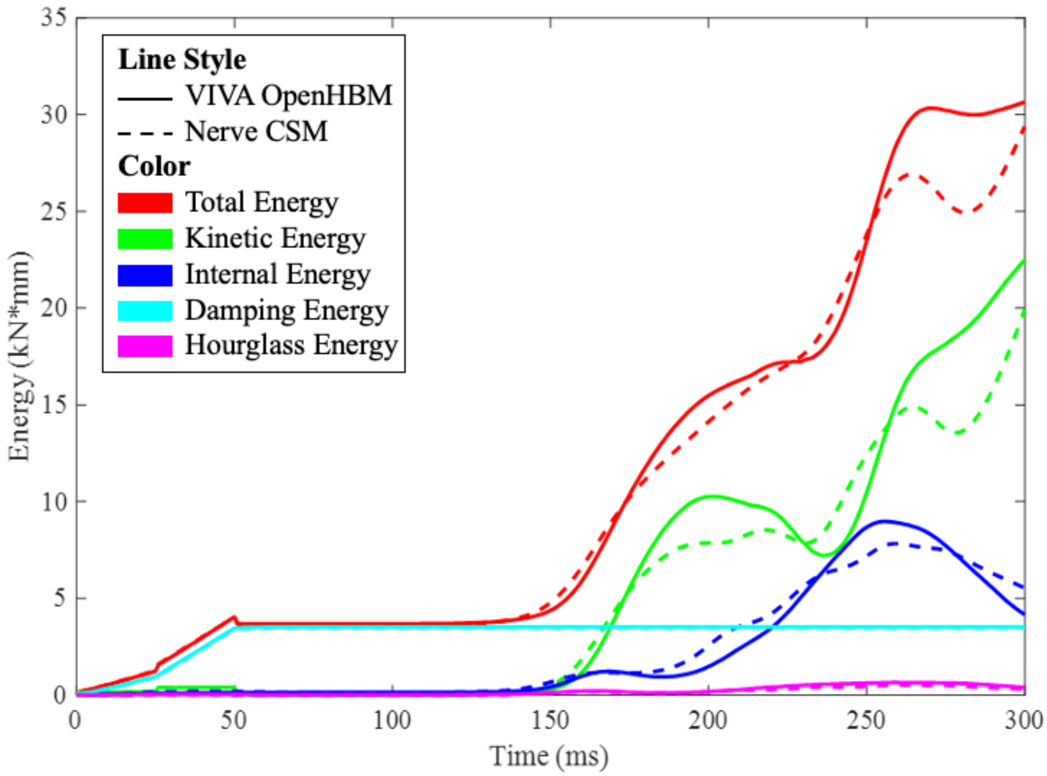

Figure 50: Whiplash System Energies of VIVA OpenHBM and Nerve CSM Mid-Q and Mid-L Models.
The solid line refers to the VIVA OpenHBM response and the dashed line refers to the Nerve CSM response.
The type of energy is distinguished by the color of the line defined in the legend.

4.3 Aim 3: Results of Spinal Cord Kinematic Validation of the Nerve CSM

The Nerve CSM spinal cord kinematics were validated alongside experimental data from (Stoner et al., 2019) and also compared to simulation data from the model by (Xue et al., 2021). The A/P, S/I and R/L relative displacements resulting from a flexion and extension simulation of the neck and head of the spinal cord at levels C3-C7 were determined and are summarized below in Figure 51.

For flexion in the A/P direction, the Nerve CSM moved posteriorly at C3 and anteriorly at the C4-7 level, sharing the same inflection point as the mean values from (Stoner et al., 2019). In the S/I direction, the Nerve CSM moved inferiorly at C3-C6 and superiorly at C7. Compared to the data from (Stoner et al., 2019), the Nerve CSM showed the most discrepancy in both direction and magnitude at the C7 level for both the A/P and S/I direction. In the L/R direction during flexion, the Nerve CSM showed much smaller displacement than the values reported by (Stoner et al., 2019) and (Xue et al., 2021). All the spinal cord displacement values of the Nerve CSM except for L/R displacement at C4 lay well within the mean value±SD reported by (Stoner et al., 2019).

For extension in the A/P direction, the Nerve CSM spinal cord showed relative anterior displacement at all levels, matching the direction seen in the data from both (Stoner et al., 2019) and (Xue et al., 2021). In the S/I direction during extension, the Nerve CSM shared an inflection point with (Stoner et al., 2019) and (Xue et al., 2021), moving inferiorly at C3 and superiorly at C4-7. L/R displacement during extension for the Nerve CSM was much smaller than the values reported by (Stoner et al., 2019). All displacement values of the Nerve CSM except for S/I displacement at C7 and L/R displacement at C3 lay within the mean value ±SD reported by (Stoner et al., 2019).

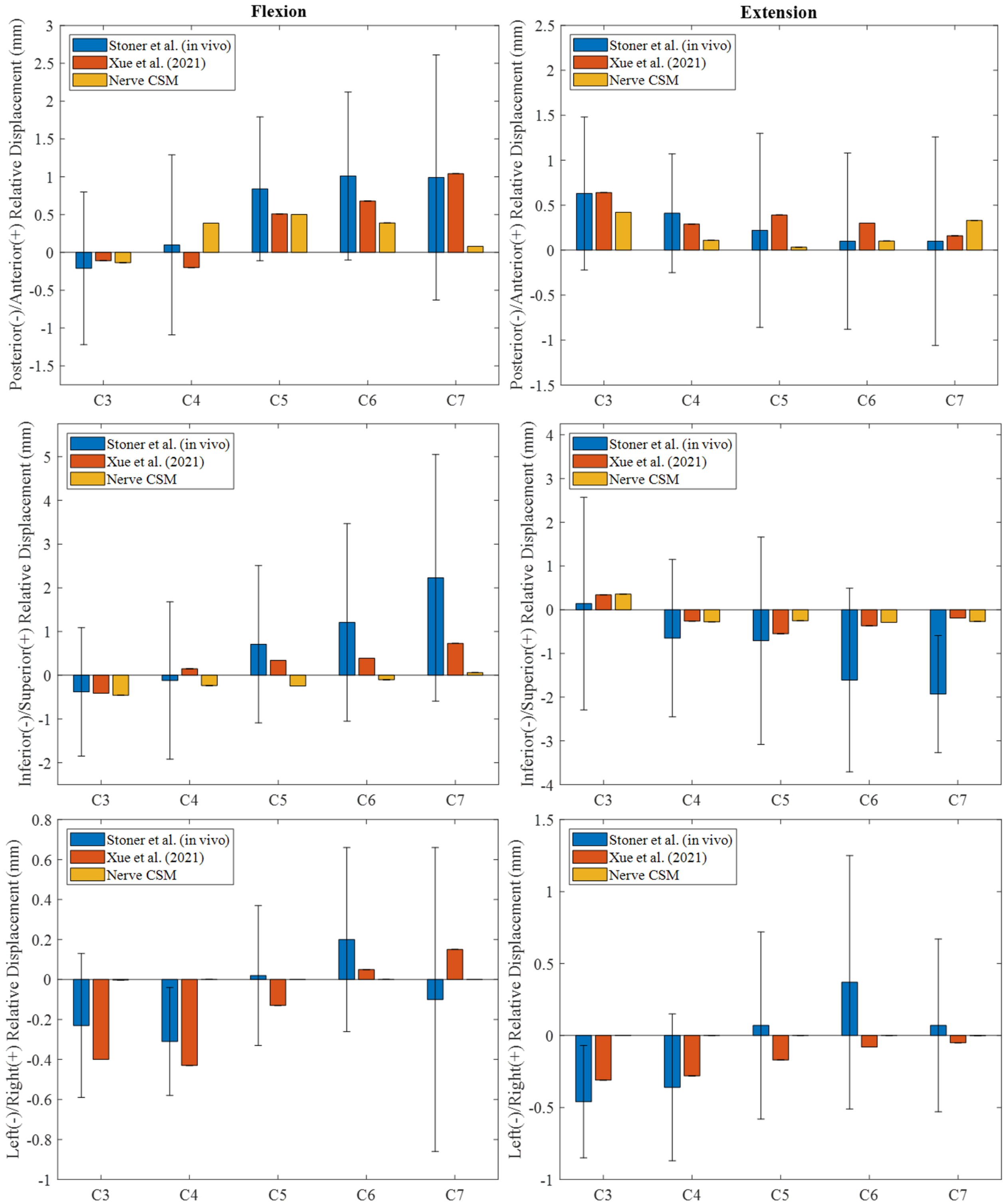

Figure 51: Relative Spinal Cord Displacement in the A/P, S/I, and L/R Directions of the Nerve CSM Model Compared to (Stoner et al., 2019) and (Xue et al., 2021).

Top left: A/P spinal cord relative displacement in flexion. Middle left: S/I spinal cord relative displacement in flexion. Bottom left: L/R spinal cord relative displacement in flexion. Top right: A/P spinal cord relative displacement in extension. Middle right: S/I spinal cord relative displacement in extension. Bottom right: L/R spinal cord relative displacement in extension. The anterior, superior, and right direction refers to the positive direction.

4.4 Nerve Root Global Movement Within the IVF Across Validation Simulations

Across the three validation simulations, which were the 2.3 m/s whiplash loading conditions (Östh et al., 2017) and the flexion/extension loading conditions (Stoner et al., 2019), the nerve root showed a proportional increase in displacement and strain as the C2/C7 angle increased (Figure 52). The vertebrae moved into an extremely extended position in the 2.3 m/s whiplash simulation, with a C2/C7 angle of -93.8º, representing a pathological ROM of the head and spine due to the sudden acceleration applied to T1, resulting in a decrease in IVF diameter. This decrease in IVF height and width caused serious impingement of the C3-C5 nerve roots (Figure 52). In the flexion/extension simulations, the vertebrae moved into much less extreme positions, with an C2/C7 extension angle of -26.3º and flexion angle of 23.4º, which represented a normal ROM movement of the head and spine. In extension, the nerve roots shifted slightly in the superior and dorsal direction and in flexion, the nerve roots shifted slightly in the inferior and ventral direction, mimicking the movement of the spinal cord (Figure 52). No impingement of the nerve roots was seen in the flexion/extension simulation, as they stayed relatively centered within the IVF.

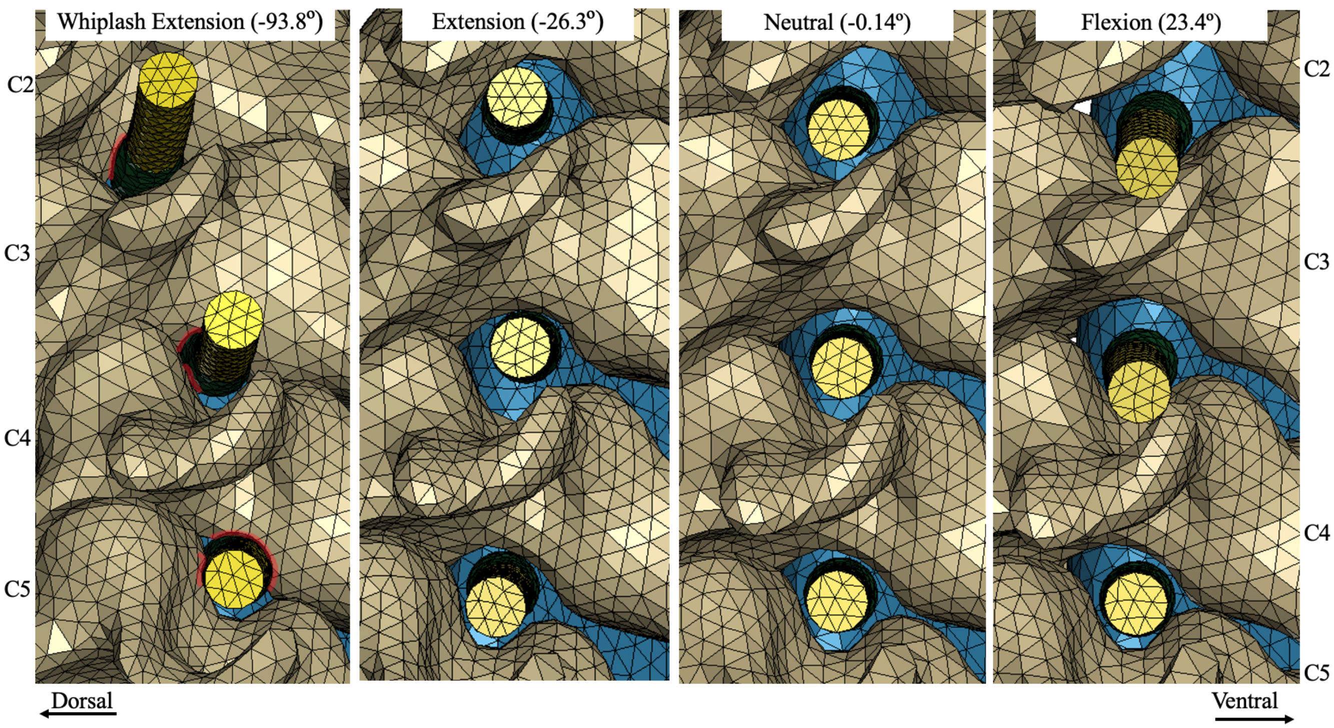

Figure 52: Right Lateral View of Nerve Root Position Within the IVF After Flexion and Extension. Far left: position of the C3-5 nerve roots within the IVF after the 2.3 m/s whiplash simulation, where the final C2/7 angle was -93.8º. The shaded areas of red represent the areas where the vertebrae have impinged on the nerve root. Middle left: position of the C3-5 nerve roots within the IVF after the normal extension simulation, where the final C2/7 angle was -26.3º, and no compression of the nerve root occurred. Middle right: position of the C3-5 nerve roots within the IVF in a neutral position before any movement of the spine was applied. Far right: position of the C3-5 nerve roots within the IVF after the normal flexion simulation, where the final C2/7 angle was 23.4º, and no compression of the nerve root occurred.

The impingement to the nerves caused by the severe and sudden extension of the vertebrae within the whiplash simulation caused the nerve root strain to be much higher than in the normal flexion/extension ROM. Figure 53 below shows the pattern of deformation and strain in the C3-5 nerve roots across the three simulations, where the magnitudes of strain in the whiplash extension so far exceeded that of the normal extension and flexion that their proportional scales were incompatible. The highest areas of strain in the nerve roots in the whiplash extension were where the nerve roots were deformed by the impinging vertebrae. The quantitative values of strain displayed below are not necessarily an accurate representation of what the nerve roots would experience *in-vivo* as they have not been validated compared to experimental data. Thus, they should not be used for any quantitative conclusions or comparisons, but instead for a general understanding of the locations and magnitudes of strain and displacement in the nerve root during differing magnitudes of flexion and extension.

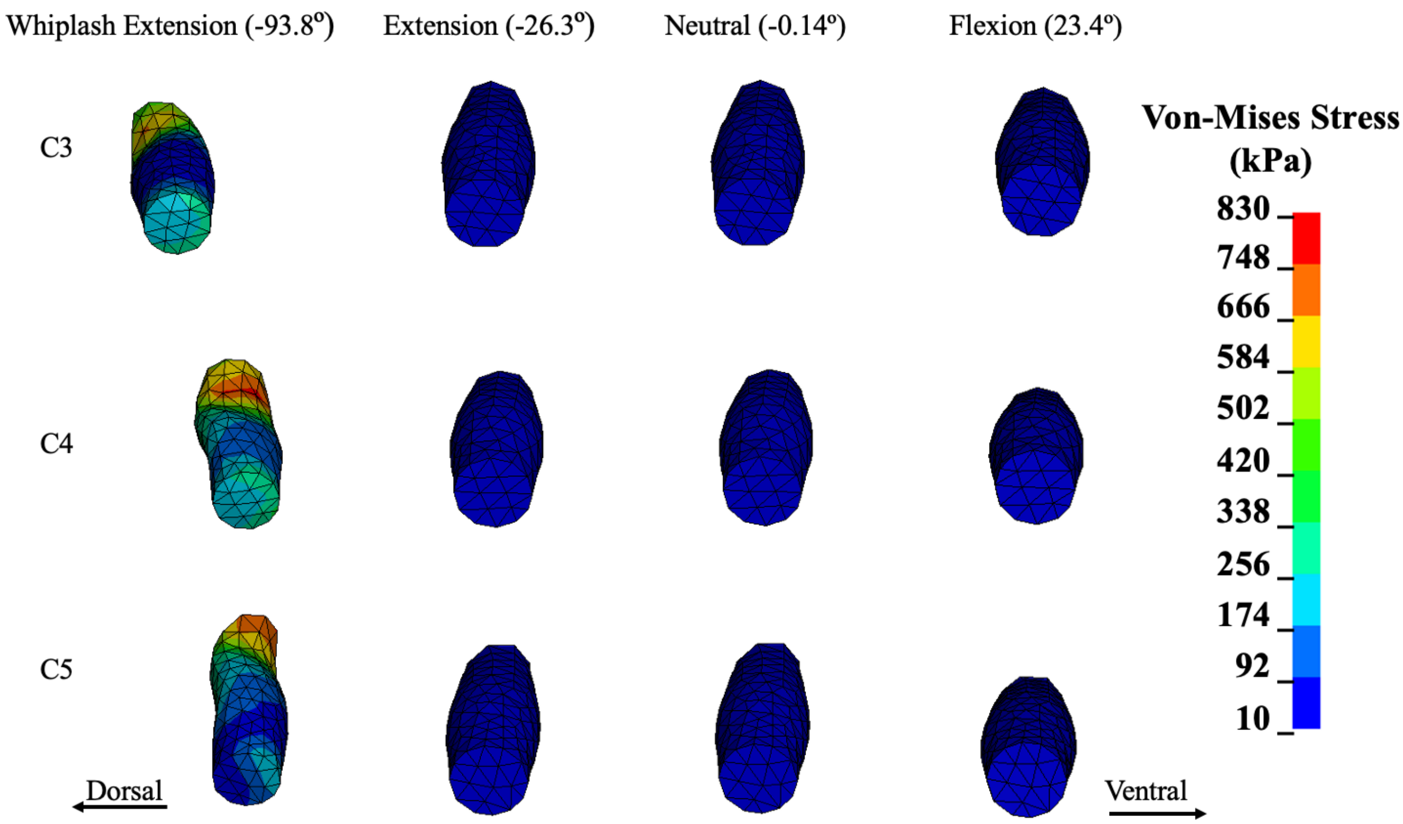

Figure 53: General Deformation and Strain in the Nerve Roots After Flexion and Extension.
Far left: strain gradient in the C3-5 nerve roots following the 2.3 m/s whiplash simulation, where extreme extension and compression of the nerve roots was observed. The highest areas of strain were those where the nerve root was deformed due to the impingement of the vertebrae. Middle left, middle right, far right: strain gradient in the C3-5 nerve roots following normal extension (middle left), the neutral position (middle right) and the normal flexion (far right) simulations, where no compression of the nerve roots were observed, resulting in a much lower magnitude of strain than seen in the nerve roots following the whiplash extension.

CHAPTER 5: DISCUSSION

5.1 Implications from the Nerve CSM Results

The global head kinematics of the Nerve CSM did not change substantially as compared to the VIVA OpenHBM. Their correlation scores were similar, and the Nerve CSM response fell within the scaled 50th percentile PMHS standard deviation corridors. Thus, it is reasonable to conclude that the addition of the nerve geometry did not considerably alter the global kinematics of the VIVA OpenHBM. Additionally, the system energies of the Nerve CSM showed similar trends to the VIVA OpenHBM in the 2.3 m/s whiplash simulation. It is thus a reasonable conclusion that the Nerve CSM can be considered validated in the 2.3 m/s whiplash simulation if global head kinematics are desired result.

The results of the spinal cord kinematic validation of the Nerve CSM demonstrated that the spinal cord moved relatively similarly in flexion and extension compared to the experimental data by (Stoner et al., 2019). While the magnitudes and directions of the A/P, S/I, and L/R displacements did not always fall near the mean value reported by (Stoner et al., 2019), almost all the simulated values fell well within the mean value±SD of the experiment. Discrepancy in the values could potentially be attributed to the constraint of T1 in the Nerve CSM model, when *in-vivo* it is possible that T1 displaces slightly during flexion and extension of the neck. The most discrepancy in the magnitude of values between the Nerve CSM and the experimental data was seen in the L/R direction for both flexion and extension. This could be due to the higher likelihood for participants to turn their heads marginally to the right or the left during the maximum flexion/extension movement, which would not occur in the Nerve CSM. The relatively small displacements of the spinal cord relative to the vertebrae in the Nerve CSM in the A/P, S/I and L/R directions during flexion and extension that are well within the variability of the reported experimental values (Stoner et al., 2019) point to a conclusion that the Nerve CSM demonstrates suitable spinal cord kinematics for a healthy participant.

Movement of the nerve root within the IVF across the three validation simulations showed that for a normal flexion/extension movement, the nerve root stayed relatively centered within the IVF, hypothesized to be due to the constraint that the foraminal ligaments offer to the nerve roots. (Shi et al., 2015; Yang et al., 2019). However, during the pathological extension of the spine from the 2.3 m/s whiplash simulation (Östh et al., 2017), the IVF diameter severely decreased, which caused compression and deformation of the nerve roots in the Nerve CSM by the vertebral walls. These insights show the value of including nerve roots to a full model of the head and vertebrae, as the magnitudes and locations of compression or increased strain can be investigated during movement and loading of the full head-neck complex.

5.2 Limitations

There were many limitations of this research study and the current Nerve CSM model. One of the biggest challenges in developing the Nerve CSM model was the correct definition of the distal boundary connections. It has been demonstrated that the spinal nerve can move in multiple directions to accommodate the motion of the spine and prevent damage to the nerve tissue (Akdemir & Neurosurg, 2010; Kraan et al., 2010). However, at more distal points in the body, the network of spinal nerves is constrained at their insertion sites. Thus, at the IVF, the spinal nerve can move, but it is unclear by how much and in what direction. Thus, the best solution this author could determine was constraining the free end of the spinal nerve to its corresponding caudal vertebrae as done by (Xue et al., 2021, 2023) since it is attached to the vertebrae through the foraminal ligaments. The most accurate solution would be to have a full model of the nervous system constrained to its corresponding tissues; but this possibility likely remains outside the limits of current FE software due to the sheer amount of computational power it would require to include such small detail at the scale of the full human body. The same problem presents itself for T1 during movements such as flexion and extension, where there is likely some motion, but it is limited due to the constraints of the lower thoracic and lumbar spine.

Additionally, due to the time consuming nature of developing a FE model of this complexity and scale, the scope of this thesis did not include further parametric studies of the material properties or validation of the stress-strain behavior of the developed tissues. To this author's knowledge, no biomechanical studies have been performed to elucidate the stress-strain behavior of both the foraminal and epidural ligaments. This is likely due to their newness in being described in the literature. Additionally, a comprehensive parameter analysis of the CSF should also be considered for a complete model of the spinal canal. In this study, it was modelled utilizing a linear elastic model according to (Baeck et al., 2011). However, there is a multitude of other publications (Duckworth et al., 2021; Jin et al., 2015; Panzer et al., 2012; J. Z. Wu et al., 2017) that investigate the utilization of more advanced material models to capture the complex biomechanical contribution that the CSF provides to the spinal system. Additionally, biomechanical studies to validate the *in-vivo* parameters related to radiculopathy of the nerve roots, such as pressure, stress, and strain are scarce and often not well-defined enough to be repeatable in an FE simulation. To advance FE models of nerve roots, more experimental data needs to be collected that could be replicated in a simulation and increase the trustworthiness of the models.

Additionally, the differences in scale between the nerve root and the overall head-neck model made it difficult to implement a sufficiently refined nerve root mesh. Originally, a mesh sensitivity analysis was performed as a part of this thesis, where six additional Nerve CSM assemblies were created with six different mesh sizes and were run under the 2.3 m/s whiplash loading scenario (Östh et al., 2017). However, because the isolated nerve root's geometrical dimensions were on a much smaller scale than the global model, a relatively fine mesh relative to the nerve root resulted in an incredibly small timestep when implemented in the global head-neck assembly, drastically increasing the simulation run-time to an unreasonable degree. Thus, across the six Nerve CSM mesh iterations, nerve root mesh sizes were chosen so that the elements would fall within the mesh quality assessment criteria (Table 4) and allow the models to run in a reasonable amount of time. However, the results showed that the stress and strain in the nerve root across the six mesh sizes did not converge. Thus, there were not enough iterations of mesh size to accomplish convergence of the results, meaning that a further refinement of the mesh should be pursued. The creation of just six iterations of the Nerve CSM assembly was extremely time consuming, mainly due to the manual re-attachment of the ligament attachments on the surface nodes of the nerve root, the recreation of the root sheath on the surface of the nerve root, and the re-assembly of the entire model for each change of the nerve root mesh. Thus, refinement of the nerve root mesh within the full scale of the head-neck model proved to be a disadvantageous approach due to these limitations. A sub-modeling approach would likely be a better fit, where the global head-neck model simulation could be run once with a coarse nerve root mesh, calculating loads and boundary conditions to apply to an isolated model of the nerve root. With this approach, the nerve root mesh could be more efficiently changed as a detached part and refined according to its own scale.

5.3 Future Research Direction

Future research directions of the Nerve CSM could include an investigation into the validity of the IFL and EFL biomechanical contribution to the nerve root. Several biomechanical studies have been performed that track the displacement of the intraforaminal nerve root under longitudinal tension with and without the EFLs (Kraan et al., 2010; Zhao et al., 2020). While these studies are not geared towards FE replication, a qualitative reproduction could provide insight into if the EFLs are dissipating traction and preventing nerve root displacement during longitudinal tension within the Nerve CSM. These results could provide insight into other research areas, such as surgical procedures of the spine and brachial plexus injury diagnosis and treatment.

Other researchers could use the methods utilized in this thesis to implement nerve tissue into spinal models at all different levels to investigate alternative topics, such as potential injury to the soft tissues from ossification of the PLL or other ligaments, IVD degeneration, operative procedures, high impact injury scenarios, or the causes of neck pain from sitting in non-ergonomical positions. To improve these models, biomechanical studies examining the mechanical properties of the foraminal and epidural ligaments should be performed, as well as other experimental studies geared toward FE validation for radiculopathy metrics within the nerve roots. Parametric analysis of the CSF material definition should also be considered.

Future researchers investigating chronic neck pain mechanisms in military pilots should determine if the gradients of strain and deformation change within the nerve root under helmet loading conditions during normal movements of the spine (flexion, extension, turning left/right). These insights are vital in understanding if the increased loading and altered head center of mass due to long helmet use contribute to an increased strain gradient or compression of the nerve roots, which could be indicators of pain. Further development of the Nerve CSM should be pursued to provide trustworthiness of these results, such as validation of the metrics of radiculopathy (strain, deformation, stress) within the nerve root compared to experimental data. If specific values of strain, deformation, or stress within the nerve root tissue are the desired result, further refinement of the mesh should be explored with a submodeling approach to overcome the scale differences between the full head-neck complex and the miniscule nerve root.

CONCLUSION

This thesis project encompassed the creation and implementation of 89 soft tissue parts within the spinal canal and IVF into the VIVA OpenHBM model, of which 40 of these soft tissue parts were completely novel in their definition, resulting in the new Nerve CSM. To the author's knowledge, this is the first comprehensive head-neck model that contains the combination of gray and white matter, CSF, the dura mater, root sheaths, nerve roots, dorsal root ganglions, nerve rootlets, spinal nerves, and denticulate, foraminal and epidural ligaments. Additionally, the Nerve CSM global head and spinal cord kinematics were validated in the 2.3 m/s whiplash and maximum flexion-extension simulations, falling within established corridors from experimental data (Stemper et al., 2005; Stoner et al., 2019). Establishment of a stable, working model of the soft tissues relevant to cervical radiculopathy will enable future researchers to build upon the Nerve CSM for investigation into chronic neck pain in military fighter and helicopter pilots. It also contributes to the advancement of cervical spine FE modelling and can give insight into many other applications involving these soft tissues, such as pain generation and injuries to the nerves from ossification of the PLL, IVD degeneration and herniation, surgical procedures, dynamic loading, and other chronic neck pain scenarios seen in the everyday world. The completion of this thesis project specifically served to contribute to the investigation into how each component within the cervical spine contributes to chronic neck pain under prolonged helmet loads within the pilot population to prevent and treat pain for decreased costs and a better quality of life.

REFERENCES

Ä, B. O., Monnier, A., & Harms-Ringdahl, K. (2009). Neck/shoulder exercise for neck pain in air force helicopter pilots: A randomized controlled trial. *Spine*, *34*(16). https://doi.org/10.1097/BRS.0B013E3181AA6870

Ah Shin, D., Lee, N., Yeul Ji, G., Yi, S., Heum Yoon, D., Nyun Kim, K., Ha, Y., & Hyun Oh, C. (2016). Basic Science Finite Element Analysis of the Effect of Epidural Adhesions. *Pain Physician*, *19*, 787–793.

Akdemir, G., & Neurosurg, J. (2010). Thoracic and lumbar intraforaminal ligaments: Laboratory investigation. *Journal of Neurosurgery: Spine*, *13*(3), 351–355. https://doi.org/10.3171/2010.3.SPINE09799

Alleyne, C. H., Cawley, C. M., Barrow, D. L., & Bonner, G. D. (1998). Microsurgical anatomy of the dorsal cervical nerve roots and the cervical dorsal root ganglion/ventral root complexes. *Surgical Neurology*, *50*(3), 213–218. https://doi.org/10.1016/S0090-3019(97)00315-7

Ang, B., & Harms-Ringdahl, K. (2006). Neck pain and related disability in helicopter pilots: A survey of prevalence and risk factors. *Aviation, Space, and Environmental Medicine*, *77*(7), 713–719.

Äng, B. O. (2008). Impaired neck motor function and pronounced pain-related fear in helicopter pilots with neck pain—A clinical approach. *Journal of Electromyography and Kinesiology : Official Journal of the International Society of Electrophysiological Kinesiology*, *18*(4), 538–549. https://doi.org/10.1016/J.JELEKIN.2007.01.002

Baeck, K., Goffin, J., & Sloten, J. (2011, May 1). *The use of different CSF representations in a numerical head model and their effect on the results of FE head impact analyses*. 8th European LS-DYNA Users Conference, Strasbourg. https://www.semanticscholar.org/paper/The-use-of-different-CSF-representations-in-a-head-Baeck-Goffin/6307fcefa371eb28ff6bd00c5418f09247209ec3

Bartlett, R. J. V., Hill, C. A. R., Rigby, A. S., Chandrasekaran, S., & Narayanamurthy, H. (2012). MRI of the cervical spine with neck extension: Is it useful? *The British Journal of Radiology*, *85*(1016), 1044–1051. https://doi.org/10.1259/bjr/94315429

Beel, J. A., Groswald, D. E., & Luttges, M. W. (1984). Alterations in the mechanical properties of peripheral nerve following crush injury. *Journal of Biomechanics*, *17*(3), 185–193. https://doi.org/10.1016/0021-9290(84)90009-5

Beel, J. A., Stodieck, L. S., & Luttges, M. W. (1986). Structural Properties of Spinal Nerve Roots: Biomechanics. *Experimental Neurology*, *91*(1), 30–40. https://doi.org/10.1016/0014-4886(86)90023-3

Betts, J. G., Young, K. A., Wise, J. A., Johnson, E., Poe, B., Kruse, D. H., Korol, O., Johnson, J. E., Womble, M., & DeSaix, P. (2013). *Anatomy and Physiology*. OpenStax. https://openstax.org/books/anatomy-and-physiology-2e/pages/1-introduction

Bloomfield, I. G., Johnston, I. H., & Bilston, L. E. (1998). Effects of proteins, blood cells and glucose on the viscosity of cerebrospinal fluid. *Pediatric Neurosurgery*, *28*(5), 246–251. https://doi.org/10.1159/000028659

Brisby, H. (2003). Nerve root injuries in patients with chronic low back pain. *Orthopedic Clinics of North American*, 221–230. https://doi.org/10.1016/S0030-5898(03)00002-6

Burkhart, T. A., Andrews, D. M., & Dunning, C. E. (2013). Finite element modeling mesh quality, energy balance and validation methods: A review with recommendations associated with the modeling of bone tissue. *Journal of Biomechanics*, *46*(9). https://doi.org/10.1016/j.jbiomech.2013.03.022

Cai, X. Y., YuChi, C. X., Du, C. F., & Mo, Z. J. (2020). The effect of follower load on the range of motion, facet joint force, and intradiscal pressure of the cervical spine: A finite element study. *Medical and Biological Engineering and Computing*, *58*(8), 1695–1705. https://doi.org/10.1007/S11517-020-02189-7

Carette, S., & Fehlings, M. G. (2005). Clinical practice. Cervical radiculopathy. *The New England Journal of Medicine*, *353*(4), 392–399. https://doi.org/10.1056/NEJMCP043887

Caridi, J. M., Pumberger, M., & Hughes, A. P. (2011). Cervical Radiculopathy: A Review. *HSS Journal : The Musculoskeletal Journal of Hospital for Special Surgery*, *7*(3), 265–272. https://doi.org/10.1007/s11420-011-9218-z

Cassidy, J. J., Hiltner, A., & Baer, E. (1989). Hierarchical Structure of the Intervertebral Disc. *Connective Tissue Research*, *23*(1), 75–88. https://doi.org/10.3109/03008208909103905

Ceylan, D., Tatarli, N., Abdullaev, T., Seker, A., Yildiz, S. D., Keles, E., Konya, D., Bayri, Y., Kilį, T., & Çavdar, S. (2012). The denticulate ligament: Anatomical properties, functional and clinical significance. *Acta Neurochirurgica*, *154*(7), 1229–1234. https://doi.org/10.1007/S00701-012-1361-X

CFCF. (2014). *Anatomical Planes* [Graphic]. https://commons.wikimedia.org/wiki/File:Anatomical_Planes.svg

Chumbley, E. M., Stolfi, A., & McEachen, J. C. (2017). Risk Factors for Cervical Pain in F-15C Pilots. *Aerospace Medicine and Human Performance*, *88*(11), 1000–1007. https://doi.org/10.3357/AMHP.4848.2017

Culley, J. (n.d.). *Compressed Root Cervical Disc*. Medical Stock Images. Retrieved June 11, 2024, from https://www.medicalstockimages.net/products/compressed-root-cervical-disc?_pos=2&_sid=3992d24f2&_ss=r

Dalton, E. (2017, February 16). Scar Remodeling, Adhesions, and Nerve Pain. *Erik Dalton Blog*. https://blog.erikdalton.com/scar-remodeling-adhesions-nerve-pain/

DBCLS, W. C. (2014). *Rat* [Graphic]. https://commons.wikimedia.org/wiki/File:201412_rat.png

De Loose, V., Van den Oord, M., Burnotte, F., Van Tiggelen, D., Stevens, V., Cagnie, B., Witvrouw, E., & Danneels, L. (2008). Individual, work-, and flight-related issues in F-16 pilots reporting neck pain. *Aviation, Space, and Environmental Medicine*, *79*(8), 779–783. https://doi.org/10.3357/asem.2285.2008

De Peretti, F., Micalefz, J., Bourgeon, A., Argenson, C., & Rabischong, P. (1989). Biomechanics of the lumbar spinal nerve roots and the first sacral root within the intervertebral foramina. *Radiologlc Anatomy Journal of Clinical Anatomy*, *11*, 221–225.

DiPaola, C. P., & Eck, J. C. (2014). Anatomy of the Spine. In *Essentials of Spinal Disorders*. Jaypee Brothers Medical Ltd. https://www.jaypeedigital.com/eReader/chapter/9789350909836/ch1

Duckworth, H., Sharp, D. J., & Ghajari, M. (2021). Smoothed particle hydrodynamic modelling of the cerebrospinal fluid for brain biomechanics: Accuracy and stability. *International Journal for Numerical Methods in Biomedical Engineering*, *37*(4), e3440. https://doi.org/10.1002/cnm.3440

Ebraheim, N. A., An, H. S., Xu, R., Ahmad, M., & Yeasting, R. A. (1996). The quantitative anatomy of the cervical nerve root groove and the intervertebral foramen. *Spine*, *21*(14), 1619–1623. https://doi.org/10.1097/00007632-199607150-00001

Fradet, L., Arnoux, P. J., Ranjeva, J. P., Petit, Y., & Callot, V. (2014). Morphometrics of the entire human spinal cord and spinal canal measured from in vivo high-resolution anatomical magnetic resonance imaging. *Spine*, *39*(4). https://doi.org/10.1097/BRS.0000000000000125

Gray, H., & Lewis, W. H. (with Harold B. Lee Library). (1918). *Anatomy of the human body*. Philadelphia : Lea & Febiger. http://archive.org/details/anatomyofhumanbo1918gray

Hämäläinen, O., Visuri, T., Kuronen, P., & Vanharanta, H. (1994). Cervical disk bulges in fighter pilots. *Aviation, Space, and Environmental Medicine*, *65*(2), 144–146.

Harrison, M. F., Coffey, B., Albert, W. J., & Fischer, S. L. (2015). Night vision goggle-induced neck pain in military helicopter aircrew: A literature review. *Aerospace Medicine and Human Performance*, *86*(1), 46–55. https://doi.org/10.3357/AMHP.4027.2015

Hasue, M., Kikuchi, S., Sakuyama, Y., & Ito, T. (1983). Anatomic study of the interrelation between lumbosacral nerve roots and their surrounding tissues. *Spine*, *8*(1), 50–58.

Holsheimer, J., Den Boer, J. A., Struijk, J. J., & Rozeboom, A. R. (1994). MR assessment of the normal position of the spinal cord in the spinal canal. *AJNR. American Journal of Neuroradiology*, *15*(5), 951–959.

Hovenga, P. E., Spit, H. H., Uijldert, M., & Dalenoort, A. M. (2005). *Improved Prediction of Hybrid-III Injury Values Using Advanced Multibody Techniques and Objective Rating* (SAE Technical Paper 2005-01–1307). SAE International. https://doi.org/10.4271/2005-01-1307

Humphreys, S. C., Chase, J., Patwardhan, A., Shuster, J., Lomasney, L., & Hodges, S. D. (1998). Flexion and traction effect on C5-C6 foraminal space. *Archives of Physical Medicine and Rehabilitation*, *79*(9), 1105–1109. https://doi.org/10.1016/s0003-9993(98)90179-4

Hung, T. K., Lin, H. S., Bunegin, L., & Albin, M. S. (1982). Mechanical and neurological response of cat spinal cord under static loading. *Surgical Neurology*, *17*(3), 213–217. https://doi.org/10.1016/0090-3019(82)90284-1

Ichihara, K., Taguchi, T., Shimada, Y., Sakuramoto, I., Kawano, S., & Kawai, S. (2001). Gray matter of the bovine cervical spinal cord is mechanically more rigid and fragile than the white matter. *Journal of Neurotrauma*, *18*(3), 361–367. https://doi.org/10.1089/08977150151071053

Jannesar, S., Salegio, E. A., Beattie, M. S., Bresnahan, J. C., & Sparrey, C. J. (2021). Correlating Tissue Mechanics and Spinal Cord Injury: Patient-Specific Finite Element Models of Unilateral Cervical Contusion Spinal Cord Injury in Non-Human Primates. *Journal of Neurotrauma*, *38*(6), 698–717. https://doi.org/10.1089/neu.2019.6840

Jin, J.-X., Zhang, J.-Y., Song, X.-W., Hu, H., Sun, X.-Y., & Gao, Z.-H. (2015). Effect of cerebrospinal fluid modeled with different material properties on a human finite element head model. *Journal of Mechanics in Medicine and Biology*, *15*(3). https://doi.org/10.1142/S021951941550027X

Jones, J. A., Hart, S. F., Baskin, D. S., Effenhauser, R., Johnson, S. L., Novas, M. A., Jennings, R., & Davis, J. (2000). Human and behavioral factors contributing to spine-based neurological cockpit injuries in pilots of high-performance aircraft: Recommendations for management and prevention. *Military Medicine*, *165*(1), 6–12.

Jørgensen, M. B., Skotte, J. H., Holtermann, A., Sjøgaard, G., Petersen, N. C., & Søgaard, K. (2011). Neck pain and postural balance among workers with high postural demands—A cross-sectional study. *BMC Musculoskeletal Disorders*, *12*. https://doi.org/10.1186/1471-2474-12-176

Kameyama, T., Hashizume, Y., & Sobue, G. (1996). Morphologic features of the normal human cadaveric spinal cord. *Spine*, *21*(11), 1285–1290. https://doi.org/10.1097/00007632-199606010-00001

Kerns, J., Piponov, H., Helder, C., Amirouche, F., Solitro, G., & Gonzalez, M. (2019). Mechanical Properties of the Human Tibial and Peroneal Nerves Following Stretch With Histological Correlations. *Anatomical Record (Hoboken, N.J.: 2007)*, *302*(11), 2030–2039. https://doi.org/10.1002/ar.24250

Khuyagbaatar, B., Kim, K., & Hyuk Kim, Y. (2014). Effect of bone fragment impact velocity on biomechanical parameters related to spinal cord injury: A finite element study. *Journal of Biomechanics*, *47*(11), 2820–2825. https://doi.org/10.1016/J.JBIOMECH.2014.04.042

Khuyagbaatar, B., Kim, K., Park, W. M., & Kim, Y. H. (2015). Influence of sagittal and axial types of ossification of posterior longitudinal ligament on mechanical stress in cervical spinal cord: A finite element analysis. *Clinical Biomechanics*, *30*(10), 1133–1139. https://doi.org/10.1016/j.clinbiomech.2015.08.013

Khuyagbaatar, B., Kim, K., Park, W. M., & Kim, Y. H. (2016). Effect of posterior decompression extent on biomechanical parameters of the spinal cord in cervical ossification of the posterior longitudinal ligament.

Http://Dx.Doi.Org/10.1177/0954411916637383, *230*(6), 545–552. https://doi.org/10.1177/0954411916637383

Khuyagbaatar, B., Kim, K., Park, W. M., & Kim, Y. H. (2017). Biomechanical investigation of post-operative C5 palsy due to ossification of the posterior longitudinal ligament in different types of cervical spinal alignment. *Journal of Biomechanics*, *57*, 54–61. https://doi.org/10.1016/J.JBIOMECH.2017.03.019

Khuyagbaatar, B., Kim, K., Purevsuren, T., Lee, S. H., & Kim, Y. H. (2018). Biomechanical Effects on Cervical Spinal Cord and Nerve Root Following Laminoplasty for Ossification of the Posterior Longitudinal Ligament in the Cervical Spine: A Comparison Between Open-Door and Double-Door Laminoplasty Using Finite Element Analysis. *Journal of Biomechanical Engineering*, *140*(7). https://doi.org/10.1115/1.4039826

Kim, H. J., Chun, H. J., Kang, K. T., Lee, H. M., Kim, H. S., Moon, E. S., Park, J. O., Hwang, B. H., Son, J.-H., & Moon, S. H. (2009). A validated finite element analysis of nerve root stress in degenerative lumbar scoliosis. *Medical & Biological Engineering & Computing*, *47*(6), 599–605. https://doi.org/10.1007/s11517-009-0463-y

Kim, K. W., Chung, J. W., Park, J. B., Song, S. W., Ha, K. Y., & An, H. S. (2004). The Course of the Nerve Root in the Neural Foramen and Its Relationship with Foraminal Entrapment or Impingement in Adult Patients with Lumbar Isthmic Spondylolisthesis and Radicular Pain. *Spinal Disorder Technology*, *17*(3), 220–225. https://doi.org/10.1097/00024720-200406000-00009

Kim, Y. H., Khuyagbaatar, B., & Kim, K. (2013). Biomechanical effects of spinal cord compression due to ossification of posterior longitudinal ligament and ligamentum flavum: A finite element analysis. *Medical Engineering & Physics*, *35*(9), 1266–1271. https://doi.org/10.1016/J.MEDENGPHY.2013.01.006

Kitab, S. A., Miele, V. J., Lavelle, W. F., & Benzel, E. C. (2009). Pathoanatomic basis for stretch-induced lumbar nerve root injury with a review of the literature. *NEUROSURGERY*, *65*. https://doi.org/10.1227/01.NEU.0000347002.67982.8F

Klingner, B., & Shewchuk, J. (2007). *Aggressive Tetrahedral Mesh Improvement*. 3–23. https://doi.org/10.1007/978-3-540-75103-8_1

Knupp, P. (2000). Achieving finite element mesh quality via optimization of the Jacobian matrix norm and associated quantities. Part I—A framework for surface mesh optimization. *International Journal for Numerical Methods in Engineering*, *48*(3), 401–420. https://doi.org/10.1002/(SICI)1097-0207(20000530)48:3<401::AID-NME880>3.0.CO;2-D

Ko, H. Y., Park, J. H., Shin, Y. B., & Baek, S. Y. (2004). Gross quantitative measurements of spinal cord segments in human. *Spinal Cord*, *42*(1), 35–40. https://doi.org/10.1038/SJ.SC.3101538

Koppaka, S., Hess-Dunning, A., & Tyler, D. J. (2022). Biomechanical characterization of isolated epineurial and perineurial membranes of rabbit sciatic nerve. *Journal of Biomechanics*, *136*. https://doi.org/10.1016/J.JBIOMECH.2022.111058

Korhonen, R. K., & Saarakkala, S. (2011). Biomechanics and Modeling of Skeletal Soft Tissues. *Theoretical Biomechanics*. https://doi.org/10.5772/19975

Kraan, G. A., Smit, T. H., Hoogland, P. V. J. M., & Snijders, C. J. (2010). Lumbar extraforaminal ligaments act as a traction relief and prevent spinal nerve compression. *Clinical Biomechanics (Bristol, Avon)*, *25*(1), 10–15. https://doi.org/10.1016/j.clinbiomech.2009.09.001

Kwan, M., & Rydevik, B. (1988). Selected biomechanical assessment of lumbosacral spinal nerve roots. *Orthopaedic Transactions*, *12*(1).

Lange, B., Torp-Svendsen, J., & Toft, P. (2011). Neck pain among fighter pilots after the introduction of the JHMCS helmet and NVG in their environment. *Aviation, Space, and Environmental Medicine*, *82*(5), 559–563. https://doi.org/10.3357/ASEM.2935.2011

Lee, N., Yeul Ji, G., Yi, S., Yoon, D. H., Nyun Kim, K., Ah Shin, D., & Hyun Oh, C. (2016). Basic Science Finite Element Analysis of the Effect of Epidural Adhesions. *Pain Physician*, *19*, 787–793.

Li, H., Ma, X., Wu, X., Liu, F., Yu, T., Yue, B., Xiang, H., & Chen, B. (2014). Morphological observation of sympathetic nerve fibers in the human posterior longitudinal ligament. *Spine*, *39*(26), 2119–2126. https://doi.org/10.1097/BRS.0000000000000647

Loeser, R. F. (2010). Age-related changes in the musculoskeletal system and the development of osteoarthritis. *Clinics in Geriatric Medicine*, *26*(3), 371–386. https://doi.org/10.1016/j.cger.2010.03.002

Lohman, C. M. (2014). 2015 Young Investigator Award Winner: Cervical Nerve Root Displacement and Strain During Upper Limb Neural Tension Testing Part 2: Role of Foraminal Ligaments in the Cervical Spine. *Spine*. https://doi.org/10.1097/BRS.0000000000000687

Luttges, M., Stodieck, L., & Beel, J. (1986). Postinjury changes in the biomechanics of nerves and roots in mice. *Journal of Manipulative and Physiological Therapeutics*, *9*(2), 89–98.

Ma, Z., Hu, S., Tan, J. S., Myer, C., Njus, N. M., & Xia, Z. (2013). In vitro and in vivo mechanical properties of human ulnar and median nerves. *Journal of Biomedical Materials Research. Part A*, *101*(9), 2718–2725. https://doi.org/10.1002/jbm.a.34573

Mansfield, M., Smith, T., Spahr, N., & Thacker, M. (2020). Cervical spine radiculopathy epidemiology: A systematic review. *Musculoskeletal Care*, *18*(4), 555–567. https://doi.org/10.1002/MSC.1498

Mattock, M. G., Asch, B. J., Hosek, J., & Boito, M. (2019). *The Relative Cost-Effectiveness of Retaining Versus Accessing Air Force Pilots*. RAND Corporation. https://www.rand.org/pubs/research_reports/RR2415.html

Mazzasette, C. (2021). *Spinal Cord within Vertebra* [Photo]. https://www.flickr.com/photos/187096960@N06/51173930139/

Melly, S. K., Liu, L., Liu, Y., & Leng, J. (2021). A review on material models for isotropic hyperelasticity. *International Journal of Mechanical System Dynamics*, *1*(1), 71–88. https://doi.org/10.1002/MSD2.12013

Membranpotensial og nerveimpuls—Biologi 1—NDLA. (n.d.). ndla.no. Retrieved June 11, 2024, from https://ndla.no/nn/subject:1:83ce68bc-19c9-4f2b-8dba-caf401428f21/topic:b0d8201d-66cc-4b29-b74b-6f7bd88a4d99/topic:185257b1-9e6e-4d0a-af6c-b85f621a7566/resource:0d3492ad-f5cc-4167-8db6-78e2987b86eb

Mihara, A. (2018). Biomechanical analysis of brachial plexus injury: Availability of three-dimensional finite element model of the brachial plexus. *Experimental and Therapeutic Medicine*, *15*, 1989–1993. https://doi.org/10.3892/etm.2017.5607

Neuromuscular Junctions and Muscle Contractions. (n.d.). Nursing Hero. Retrieved June 11, 2024, from https://www.nursinghero.com/study-guides/cuny-csi-ap-1/neuromuscular-junctions-and-muscle-contractions

Neuron. (n.d.). Pxhere. Retrieved June 11, 2024, from https://pxhere.com/en/photo/1453897

Newman, D. G. (1996). Cervical intervertebral disc protrusion in an RAAF F-111C pilot: A case report—PubMed. *Aviation, Space, and Environmental Medicine*, *67*(4), 351–353.

Nishida, N., Kanchiku, T., Ohgi, J., Ichihara, K., Chen, X., & Taguchi, T. (2015). Mechanical properties of nerve roots and rami radiculares isolated from fresh pig spinal cords. *Neural Regeneration Research*, *10*(11), 1869–1873. https://doi.org/10.4103/1673-5374.170319

Nowicki, B. H., Haughton, V. M., Schmidt, T. A., Lim, T.-H., An, H. S., Iii, L. H. R., Yu, L., & Hong, J.-W. (1996). Occult Lumbar Lateral Spinal Stenosis in Neural Foramina Subjected to Physiologic Loading. *AJNR Am J Neuroradiol*, *17*, 1605–1614.

O'Conor, D. K., Dalal, S., Ramachandran, V., Shivers, B., Shender, B. S., & Jones, J. A. (2020). Crew-Friendly Countermeasures Against Musculoskeletal Injuries in Aviation and Spaceflight. *Frontiers in Physiology*, *11*, 837. https://doi.org/10.3389/fphys.2020.00837

Olmarker, K. (1991). Pathophysiology of sciatica. *The Orthopedic Clinics of North America*, *22*(2), 223–234.

Omholt, M. L., Tveito, T. H., & Ihlebæk, C. (2017). Subjective health complaints, work-related stress and self-efficacy in Norwegian aircrew. *Occupational Medicine (Oxford, England)*, *67*(2), 135–142. https://doi.org/10.1093/occmed/kqw127

Östh, J., Brolin, K., Svensson, M. Y., & Linder, A. (2016). A Female Ligamentous Cervical Spine Finite Element Model Validated for Physiological Loads. *Journal of Biomechanical Engineering*, *138*(6). https://doi.org/10.1115/1.4032966

Östh, J., Mendoza-Vazquez, M., Sato, F., Svensson, M. Y., Linder, A., & Brolin, K. (2017). A female head-neck model for rear impact simulations. *Journal of Biomechanics*, *51*, 49–56. https://doi.org/10.1016/J.JBIOMECH.2016.11.066

Paggi, V., Outman, A., Micera, S., & Lacour, S. P. (2021). Compliant peripheral nerve interfaces. *Journal of Neural Engineering*, *18*(3). https://doi.org/10.1088/1741-2552/abcdbe

Palmerska, M., Mackiewicz, A., Klekiel, T., Noszczyk-Nowak, A., & Będziński, R. (2022). Characteristics of Nerve Roots Mechanical Properties Exposed to Uniaxial Stretching Tests. *Lecture Notes in Networks and Systems*, *328 LNNS*, 123–131. https://doi.org/10.1007/978-3-030-86297-8_11/COVER

Panzer, M. B., Myers, B. S., Capehart, B. P., & Bass, C. R. (2012). Development of a finite element model for blast brain injury and the effects of CSF cavitation. *Annals of Biomedical Engineering*, *40*(7), 1530–1544. https://doi.org/10.1007/s10439-012-0519-2

Persson, C., Evans, S., Marsh, R., Summers, J. L., & Hall, R. M. (2010). Poisson's ratio and strain rate dependency of the constitutive behavior of spinal dura mater. *Annals of Biomedical Engineering*, *38*(3), 975–983. https://doi.org/10.1007/S10439-010-9924-6/FIGURES/12

Phillips, J. B., Smit, X., De Zoysa, N., Afoke, A., & Brown, R. A. (2004). Peripheral nerves in the rat exhibit localized heterogeneity of tensile properties during limb movement. *The Journal of Physiology*, *557*(Pt 3), 879–887. https://doi.org/10.1113/jphysiol.2004.061804

Polak, K., Czyz, M., Ścigała, K., Jarmundowicz, W., & Bedziński, R. (2014). Biomechanical characteristics of the porcine denticulate ligament in different vertebral levels of the cervical spine-preliminary results of an experimental study. *Journal of the Mechanical Behavior of Biomedical Materials*, *34*, 165–170. https://doi.org/10.1016/J.JMBBM.2014.02.010

Posch, M., Schranz, A., Lener, M., Senn, W., Äng, B. O., Burtscher, M., & Ruedl, G. (2019). Prevalence and potential risk factors of flight-related neck, shoulder and low back pain among helicopter pilots and crewmembers: A questionnaire-based study. *BMC Musculoskeletal Disorders*, *20*(1), 1–10. https://doi.org/10.1186/S12891-019-2421-7/TABLES/2

Pousette, M. W., Martire, R. L., Linder, J., Kristoffersson, M., & äng, B. O. (2016). Neck Muscle Strain in Air Force Pilots Wearing Night Vision Goggles. *Aerospace Medicine and Human Performance*, *87*(11), 928–932. https://doi.org/10.3357/AMHP.4579.2016

Quenneville, C. E., & Dunning, C. E. (2011). Development of a finite element model of the tibia for short-duration high-force axial impact loading. *Computer Methods in Biomechanics and Biomedical Engineering*, *14*(2), 205–212. https://doi.org/10.1080/10255842.2010.548324

Rahman, W. U., Jiang, W., Zhao, F., Li, Z., Wang, G., & Yang, G. (2022). Biomechanical effect of C5-C6 intervertebral disc degeneration on the human lower cervical spine (C3-C7): A finite element study. *Computer Methods in Biomechanics and Biomedical Engineering*. https://doi.org/10.1080/10255842.2022.2089026

Ray, M., Mongiardini, M., Atahan, A. O., Plaxico, C., & Anghileri, M. (2008). Recommended procedures for verification and validation of computer simulations used for roadside safety applications. *National Cooperative Highway Research Program*, 22–24.

Rosso, G., & Guck, J. (2019). Mechanical changes of peripheral nerve tissue microenvironment and their structural basis during development. *APL Bioengineering*, *3*(3). https://doi.org/10.1063/1.5108867

Royalty-Free photo: Blood cells illustration. (n.d.). PickPik. Retrieved June 11, 2024, from https://www.pickpik.com/blood-cells-red-medical-medicine-anatomy-1901

Runza, M., Pietrabissa, R., Mantero, S., Albani, A., Quaglini, V., & Contro, R. (1999). Lumbar Dura Mater Biomechanics. *Anesthesia & Analgesia*, *88*(6), 1317–1321. https://doi.org/10.1213/00000539-199906000-00022

Rydevik, B., Brown, M. D., & Lundborg, G. (1984). Pathoanatomy and pathophysiology of nerve root compression. *Spine*, *9*(1), 7–15. https://doi.org/10.1097/00007632-198401000-00004

Rydevik, B. L. (1992). The effects of compression on the physiology of nerve roots. *Journal of Manipulative and Physiological Therapeutics*, *15*(1), 62–66.

Rydevik, B. L., Kwan, M. K., Myers, R. R., Brown, R. A., Triggs, K. J., Woo, S. L., & Garfin, S. R. (1990). An in vitro mechanical and histological study of acute stretching on rabbit tibial nerve. *Journal of Orthopaedic Research: Official Publication of the Orthopaedic Research Society*, *8*(5), 694–701. https://doi.org/10.1002/jor.1100080511

Rydevik, B. L., Myers, R. R., & Powell, H. C. (1989). Pressure increase in the dorsal root ganglion following mechanical compression. Closed compartment syndrome in nerve roots. *Spine*, *14*(6), 574–576. https://doi.org/10.1097/00007632-198906000-00004

Rydevik, B., Lundborg, G., Olmarker, K., & Myers, R. (2012). Biomechanics of peripheral nerves and spinal nerve roots. In M. Nordin, V. H. Frankel, & D. Leger (Eds.), *Basic biomechanics of the musculoskeletal system* (pp. 128–149). Wolters Kluwer.

Salmon, D. M., Harrison, M. F., & Neary, J. P. (2011). Neck pain in military helicopter aircrew and the role of exercise therapy. *Aviation Space and Environmental Medicine*, *82*(10), 978–987. https://doi.org/10.3357/ASEM.2841.2011

Salmon, D. M., Harrison, M. F., Sharpe, D., Albert, W. J., Candow, D., & Neary, J. P. (2013). Exercise therapy for improved neck muscle function in helicopter aircrew. *Aviation Space and Environmental Medicine*, *84*(10), 1046–1054. https://doi.org/10.3357/ASEM.3593.2013

Scali, F., Pontell, M. E., Nash, L. G., & Enix, D. E. (2015). Investigation of meningomyovertebral structures within the upper cervical epidural space: A sheet plastination study with clinical implications. *The Spine Journal*, *15*(11), 2417–2424. https://doi.org/10.1016/j.spinee.2015.07.438

Schall, D. G. (1989). Non-ejection cervical spine injuries due to +Gz in high performance aircraft. *Aviation, Space, and Environmental Medicine*, *60*(5), 445–456.

Sens, P., Dubey, S., Bhembre, N., Bodas, S., Veer, S., Ghose, A., Callan-Jones, A., & Pullarkat, P. (2020). *The axonal actin-spectrin lattice acts as a tension buffering shock absorber*. https://doi.org/10.7554/eLife.51772

Shen, T.-W. D. (2020). *Investigation of Whiplash Associated Disorders using Finite Element Neck Models with Active Musculature in Frontal, Rear and Lateral Impact*. https://uwspace.uwaterloo.ca/handle/10012/15716

Sherman, J. L., Nassaux, P. Y., & Citrin, C. M. (1990). Measurements of the normal cervical spinal cord on MR imaging. *AJNR. American Journal of Neuroradiology*, *11*(2), 369–372.

Shi, B., Zheng, X., Min, S., Zhou, Z., Ding, Z., & Jin, A. (2014). The morphology and clinical significance of the dorsal meningovertebra ligaments in the cervical epidural space. *The Spine Journal*, *14*(11), 2733–2739. https://doi.org/10.1016/j.spinee.2014.04.014

Shi, B., Zheng, X., Zhang, H., Sun, C., Cao, Y., Jin, A., & Ding, Z. (2015). The morphology and clinical significance of the extraforaminal ligaments at the cervical level. *Spine*, *40*(1), E9–E17. https://doi.org/10.1097/BRS.0000000000000668

Singh, A., Lu, Y., Chen, C., & M Cavanaugh, J. (2006). Mechanical properties of spinal nerve roots subjected to tension at different strain rates. *Journal of Biomechanics*, *39*(9), 1669–1676. https://doi.org/10.1016/J.JBIOMECH.2005.04.023

Sjölander, P., Michaelson, P., Jaric, S., & Djupsjöbacka, M. (2008). Sensorimotor disturbances in chronic neck pain—Range of motion, peak velocity, smoothness of movement, and repositioning acuity. *Manual Therapy*, *13*(2), 122–131. https://doi.org/10.1016/J.MATH.2006.10.002

Spinal Cord Segments and Spinal Roots. (n.d.). Retrieved June 11, 2024, from https://vanat.ahc.umn.edu/neurLab2/pages/SpCdCranHalf.html

Standring, S. (2020). *Gray's Anatomy, The Anatomical Basis of Clinical Practice* (42nd ed.). https://shop.elsevier.com/books/grays-anatomy/standring/978-0-7020-7705-0

Stemper, B. D., Yoganandan, N., & Pintar, F. A. (2004). Response Corridors of the Human Head-Neck Complex in Rear Impact. *Annual Proceedings / Association for the Advancement of Automotive Medicine*, *48*, 149–163.

Stemper, B. D., Yoganandan, N., & Pintar, F. A. (2005). Effects of abnormal posture on capsular ligament elongations in a computational model subjected to whiplash loading. *Journal of Biomechanics*, *38*(6), 1313–1323. https://doi.org/10.1016/j.jbiomech.2004.06.013

Stijn, T. J., & van den Oord, M. H. A. H. (2015). Modern Air Combat Developments and Their Influence on Neck and Back Pain in F-16 Pilots. *Aerospace Medicine and Human Performance*, *86*(11), 936–941. https://doi.org/10.3357/AMHP.4303.2015

Stoner, K. E., Abode-Iyamah, K. O., Magnotta, V. A., Howard, M. A., & Grosland, N. M. (2019). Measurement of in vivo spinal cord displacement and strain fields of healthy and myelopathic cervical spinal cord. *Journal of Neurosurgery. Spine*, *31*(1), 53–59. https://doi.org/10.3171/2018.12.SPINE18989

Subramani, A. V., Whitley, P. E., Garimella, H. T., & Kraft, R. H. (2020). Fatigue damage prediction in the annulus of cervical spine intervertebral discs using finite element analysis. *Computer Methods in Biomechanics and Biomedical Engineering*, *23*(11), 773–784. https://doi.org/10.1080/10255842.2020.1764545

Sugawara, O., Atsuta, Y., Iwahara, T., Muramoto, T., Watakabe, M., & Takemitsu, Y. (1996). The effects of mechanical compression and hypoxia on nerve root and dorsal root ganglia. An analysis of ectopic firing using an in vitro model. *Spine*, *21*(18), 2089–2094. https://doi.org/10.1097/00007632-199609150-00006

Sunderland, S., & Bradley, K. C. (1961). Stress-strain phenomena in denervated peripheral nerve trunks. *Brain*, *84*(1), 125–127. https://doi.org/10.1093/BRAIN/84.1.125

Tamura, A., Murakami, J., Sone, Y., & Koide, T. (2015). Strain Rate Effects on the Tensile Behavior of Fiber Bundles Isolated from Nerve Root. *JOURNAL OF SUSTAINABLE RESEARCH IN ENGINEERING*, *2*(2), 63–69.

Tardieu, G. G., Fisahn, C., Loukas, M., Moisi, M., Chapman, J., Oskouian, R. J., & Tubbs, R. S. (2016). The Epidural Ligaments (of Hofmann): A Comprehensive Review of the Literature. *Cureus*, *8*(9), e779. https://doi.org/10.7759/cureus.779

Tencer, A. F., Allen, B. L., & Ferguson, R. L. (1985). A biomechanical study of thoracolumbar spine fractures with bone in the canal. Part III. Mechanical properties of the dura and its tethering ligaments. *Spine*, *10*(8), 741–747. https://doi.org/10.1097/00007632-198510000-00009

Thoolen, S. J. J., & van den Oord, M. H. A. H. (2015). Modern Air Combat Developments and Their Influence on Neck and Back Pain in F-16 Pilots. *Aerospace Medicine and Human Performance*, *86*(11), 936–941. https://doi.org/10.3357/AMHP.4303.2015

Tubbs, R. S., Loukas, M., Slappey, J. B., Shoja, M. M., Oakes, W. J., & Salter, E. G. (2007). Clinical anatomy of the C1 dorsal root, ganglion, and ramus: A review and anatomical study. *Clinical Anatomy*, *20*(6), 624–627. https://doi.org/10.1002/ca.20472

umimeto.org, T. K. &. (2020). *English: Human spinal cord with meninges* [Graphic]. https://commons.wikimedia.org/wiki/File:Human_spinal_cord_svg.svg

Untaroiu, C., Darvish, K., Crandall, J., Deng, B., & Wang, J.-T. (2005). A finite element model of the lower limb for simulating pedestrian impacts. *Stapp Car Crash Journal*, *49*, 157–181. https://doi.org/10.4271/2005-22-0008

Van den Oord, M. H. A. H., Frings-Dresen, M. H. W., & Sluiter, J. K. (2012). Optimal helmet use and adjustments with respect to neck load: The experience of military helicopter aircrew. *International Journal of Industrial Ergonomics*, *42*(1), 73–79. https://doi.org/10.1016/J.ERGON.2011.09.001

Wadhwani, S., Loughenbury, P., & Soames, R. (2004). The anterior dural (Hofmann) ligaments. *Spine*, *29*(6), 623–627. https://doi.org/10.1097/01.brs.0000115129.59484.24

Walbeehm, E. T., Afoke, A., De Wit, T., Holman, F., Hovius, S. E. R., & Brown, R. A. (2004). Mechanical functioning of peripheral nerves: Linkage with the "mushrooming" effect. *Cell and Tissue Research*, *316*(1), 115–121. https://doi.org/10.1007/S00441-004-0867-9

Wallace, J. B., Newman, P. M., McGarvey, A., Osmotherly, P. G., Spratford, W., & Gabbett, T. J. (2021). Factors associated with neck pain in fighter aircrew: A systematic review and meta-analysis. *Occupational and Environmental Medicine*, *78*(12), 900–912. https://doi.org/10.1136/oemed-2020-107103

Walters PL, Cox JM, Clayborne K, & Hathaway AJ. (2012). *Prevalence of Neck and Back Pain amongst Aircrew at the Extremes of Anthropometric Measurements*. Defense Technical Information Center. Alexandria: USAARL Reports No. 2012–12; https://apps.dtic.mil/sti/citations/ADA564323

Wikipedia, C. (2007, January 26). *"Intervertebral Foramen," Wikipedia Commons*. https://commons.wikimedia.org/wiki/File:Foraminaintervertebralia.png

Wong, Y.-R., Pang, X., Lim, Z. Y., Du, H., Tay, S.-C., & McGrouther, D. A. (2019). Biomechanical evaluation of peripheral nerves after crush injuries. *Heliyon*, *5*(4), e01557. https://doi.org/10.1016/j.heliyon.2019.e01557

Wu, J. Z., Pan, C. S., Wimer, B. M., & Rosen, C. L. (2017). An improved finite element modeling of the cerebrospinal fluid layer in the head impact analysis. *Bio-Medical Materials and Engineering*, *28*(2), 187–199. https://doi.org/10.3233/BME-171666

Wu, S.-K., Kuo, L.-C., Lan, H.-C. H., Tsai, S.-W., Chen, C.-L., & Su, F.-C. (2007). The quantitative measurements of the intervertebral angulation and translation during cervical flexion and extension. *European Spine Journal: Official Publication of the European Spine Society, the European Spinal Deformity Society, and the European Section of the Cervical Spine Research Society*, *16*(9), 1435–1444. https://doi.org/10.1007/s00586-007-0372-4

Wu, S.-K., Kuo, L.-C., Lan, H.-C. H., Tsai, S.-W., & Su, F.-C. (2010). Segmental percentage contributions of cervical spine during different motion ranges of flexion and extension. *Journal of Spinal Disorders & Techniques*, *23*(4), 278–284. https://doi.org/10.1097/BSD.0b013e3181a98d26

Xue, F., Chen, Z., Yang, H., Chen, T., & Li, Y. (2021). Effects of cervical rotatory manipulation on the cervical spinal cord: A finite element study. *Journal of Orthopaedic Surgery and Research*, *16*(1), 737. https://doi.org/10.1186/s13018-021-02885-6

Xue, F., Deng, H., Chen, Z., Yang, H., Li, Y., Yuan, S., Zheng, N., & Chen, M. (2023). Effects of cervical rotatory manipulation on the cervical spinal cord complex with ossification of the posterior longitudinal ligament in the vertebral canal: A finite element study. *Frontiers in Bioengineering and Biotechnology*, *11*. https://doi.org/10.3389/FBIOE.2023.1095587

Yabuki, S., & Kikuchi, S. (1996). Positions of dorsal root ganglia in the cervical spine. An anatomic and clinical study. *Spine*, *21*(13), 1513–1517. https://doi.org/10.1097/00007632-199607010-00004

Yamamoto, I., Panjabi, M. M., & Oxland, T. (1989). Three-dimensional movements of the whole lumbar spine and lumbosacral joint. *Spine*, *14*(11), 1256–1260. https://doi.org/10.1097/00007632-198911000-00020

Yang, Y., Shi, B., Duan, Y., Qiu, S., & Liu, Z. (2019). Anatomic morphology and clinical significance of intraforaminal ligaments of the cervical spine. *Clinical Anatomy (New York, N.Y.)*, *32*(5), 654–660. https://doi.org/10.1002/ca.23364

Yong-Hing, K., Reilly, J., & Kirkaldy-Willis, W. H. (1976). The Ligamentum Flavum. *Spine*, *1*(4), 226.

Yoshizawa, H., Kobayashi, S., & Morita, T. (1995). Chronic nerve root compression. Pathophysiologic mechanism of nerve root dysfunction. *Spine*, *20*(4), 397–407. https://doi.org/10.1097/00007632-199502001-00001

Zhao, Q., Yang, Y., Wu, P., Huang, C., Zhang, R., Li, Q., & Shi, B. (2020). Biomechanical study of the C5-C8 cervical extraforaminal ligaments. *Journal of Orthopaedic Surgery and Research*, *15*(1). https://doi.org/10.1186/s13018-020-02006-9